

REPORT DOCUMENTATION PAGE			Form Approved OMB No. 0704-0188	
<small>Public reporting burden for this collection of information is estimated to average 1 hour per response, including the time for reviewing instructions, searching existing data sources, gathering and maintaining the data needed, and completing and reviewing the collection of information. Send comments regarding this burden estimate or any other aspect of this collection of information, including suggestions for reducing this burden, to Washington Headquarters Services, Directorate for Information Operations and Reports, 1215 Jefferson Davis Highway, Suite 1204, Arlington, VA 22202-4302, and to the Office of Management and Budget, Paperwork Reduction Project (0704-0188), Washington, DC 20503.</small>				
1. AGENCY USE ONLY (Leave Blank)	2. REPORT DATE 26 July 96	3. REPORT TYPE AND DATES COVERED Final 23 Aug 95 - 30 June 96		
4. TITLE AND SUBTITLE Dynamic Simulation of High-Power Machinery Systems		5. FUNDING NUMBERS Contract N61533-95-C-0107		
6. AUTHOR(S) S. D. Sudhoff O. Wasynczuk P. C. Krause				
7. PERFORMING ORGANIZATION NAME(S) AND ADDRESS(ES) PC Krause and Associates, Inc. 3016 Ccvington St. West Lafayette, IN 47906		8. PERFORMING ORGANIZATION REPORT NUMBER NSBIR-0001		
9. SPONSORING/MONITORING AGENCY NAME(S) AND ADDRESS(ES) NSWC, Caderock Division Annapolis Detachment Code 808, Henry Robey Annapolis, MD 21402-5067		10. SPONSORING/MONITORING  <b>19960802 016</b>		
11. SUPPLEMENTARY NOTES Originally monitored by Jignas Cherry, Code 826				
12a. DISTRIBUTION/AVAILABILITY STATEMENT Approved for public release; distribution unlimited		12b. DISTRIBUTION CODE		
13. ABSTRACT (Maximum 200 words) The purpose of this research was to develop accurate computationally efficient detailed and reduced-order computer models for typical high-power machinery systems being used or considered by the Navy. The detailed and reduced-order models of the example integrated power system (IPS) were developed. Example computer studies are given to illustrate the system performance during various large-disturbances including the operation of the pulsed power load. For purposes of validating the reduced-order modeling techniques, duplicate studies were performed using the detailed and reduced-order system simulations. These studies are presented along with an analytical description of the simulation of each component. The digital code is also provided to the Program Manager for use by the Navy and/or their contractors. It was also demonstrated that a vector controlled induction motor could cause negative-impedance system instability. A control was developed to eliminate this instability. This instability was predicted and eliminated by the computer models developed and then verified in hardware.				
14. SUBJECT TERMS Efficient, Accurate Computer Models of IPS Negative-Impedance Instability Vector Controlled Induction Motor Stabilizer for Vector Controller		15. NUMBER OF PAGES 128		
		16. PRICE CODE		
17. SECURITY CLASSIFICATION OF REPORT	18. SECURITY CLASSIFICATION OF THIS PAGE	19. SECURITY CLASSIFICATION OF ABSTRACT	20. LIMITATION OF ABSTRACT	

**Table of Contents**

	Page
EXECUTIVE SUMMARY/INTRODUCTION	1
SYSTEM DESCRIPTION AND MODEL DEVELOPMENT	3
COMPUTER STUDIES	30
REFERENCES	102
APPENDICES	103
Appendix A: DC Link Stabilized Field Oriented Control of Electric Propulsion Systems	
Appendix B: Modeling Consideration in a 15-Phase Induction Motor Drive System	
Appendix C: Control of a 15-Phase Induction Motor Drive System	

## EXECUTIVE SUMMARY/INTRODUCTION

As a first step, PCKA and NSWC met and mutually agreed upon an example system to be simulated for the purpose of investigating high-power machinery systems. This system, which is shown later in Fig. 1, is similar to the proposed integrated power system (IPS) in that, the salient features of the IPS are included. Briefly, the sample IPS considered consists of a 3-phase synchronous machine, ac distribution, a ship service power supply, a 15-phase, 19 MW propulsion drive and a pulsed power load. This system was selected to illustrate the utility and facility of simulation in the analysis and design of high-power machinery systems.

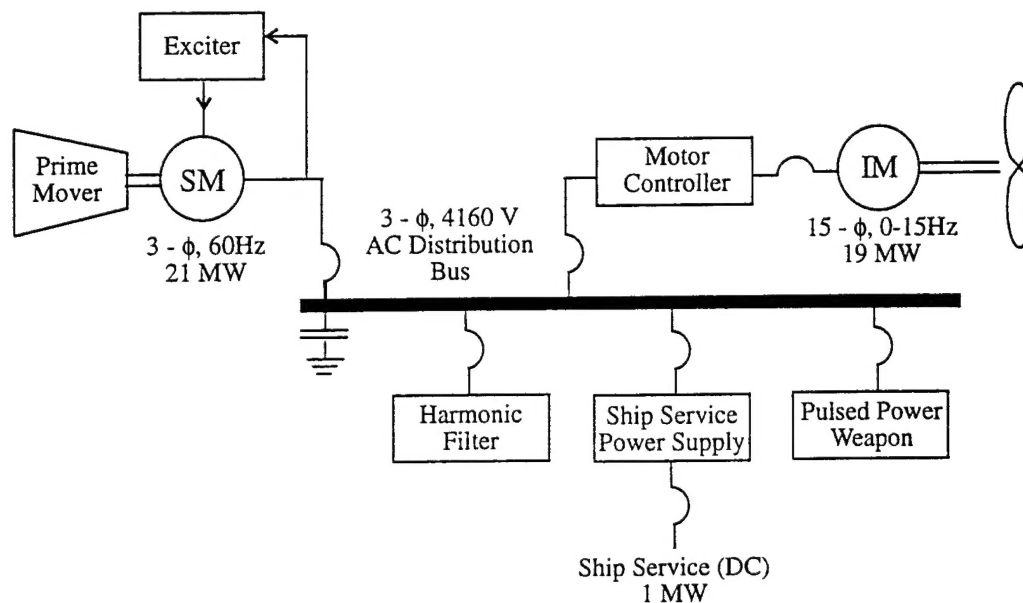


Figure 1. System studied.

In the original SBIR Phase I proposal, PCKA suggested that the selected system be simulated in both detailed and reduced-order models and that the concept of waveform reconstruction be used whenever appropriate. This technique (waveform reconstruction), which was introduced by PCKA in a previous SBIR Phase II, provides a means to accelerate the speed of computation by extracting information from the reduced-order model to reconstruct the instantaneous waveforms of the system variables. However, during the interim between submitting the proposal and the contract award, PCKA personnel were successful in developing a simulation technique which markedly increased the speed of computation of the detailed system

simulation [1]. As this technique developed, it became clear that waveform reconstruction of the system variables from the reduced-order simulation was less important. Therefore, this approach was not pursued even though this technique could be applied using the reduced-order models developed in this SBIR. Instead, attention was focused on demonstrating the facility of a detailed and reduced-order system simulation for analysis and design purposes of high-power systems.

In this SBIR Phase I, the detailed and reduced-order models of the example IPS were developed. Example computer studies are given to illustrate the system performance during various large-disturbances including the operation of the pulsed power weapon. For purposes of validating the reduced-order modeling techniques, duplicate studies were performed using the detailed and reduced-order system simulations. These studies are presented in this report along with an analytical description of the simulation of each system component. In some cases, however, references are cited rather than repeating previous derivations. The digital code is also given to the Program Manager, Mr. Henry Robey of NSWC Annapolis, so that these simulations (detailed and reduced-order) can be used by the Navy and/or their contractors.

There are additional aspects of this work which are considered innovative with applications well beyond the proposed IPS. In particular, the analysis of the 15-phase induction machine is new and the simulation developed should have application to other multiphase induction or synchronous machines [Appendix B]. Another aspect of this work deals with system stability. It was found that the field-oriented control (vector control) associated with the proposed 15-phase propulsion induction motor drive, exhibited negative-impedance instability [Appendix C]. This was verified by implementing in hardware a lower power, 3-phase induction motor with the same type of vector control [Appendix A]. It was shown that this system also inhibited negative-impedance instability. In other words, this verified that, when placed in a system, vector controlled machines could promote negative-impedance system instability in a manner similar to that of constant power loads. To our knowledge, this has not been demonstrated previously.



Perhaps more important than demonstrating that negative-impedance system instability could occur due to vector controlled machines, is the fact that PCKA personnel (S. D. Sudhoff) developed a control technique which prevents this instability [Appendix A]. In particular, by incorporating an additional control within the vector control, system stability can be maintained with insignificant degradation of the performance of the vector controlled machine. It is of utmost importance to emphasize that the negative-impedance feature of the vector control was discovered through the detailed simulation of the proposed IPS. Moreover, the technique to eliminate this instability was also developed through simulation before implementing the hardware prototype. These facts alone attest to the success of this SBIR Phase I research by demonstrating the value of computationally efficient detailed models and nonlinear reduced-order models derived from and validated against these detailed models. This work sets the stage for Phase II wherein an ACSL-based simulation library for shipboard electric power/drive systems, specifically the IPS, will be developed and demonstrated. In Phase III this library would be made available by the Navy in the advanced surface and machinery program (ASMP) and to Navy contractors for the IPS full scale engineered development (FSED) system integration efforts.

## **SYSTEM DESCRIPTION AND MODEL DEVELOPMENT**

The system considered in this study is illustrated in Fig. 1. The turbine is the prime mover for a 3-phase, 60 Hz, 21 MW, 4160 V (line-to-line) synchronous machine. The voltage is controlled by an IEEE Type 2 excitation system. The synchronous machine is connected to a 3-phase 4160 V ac distribution bus. The principal load on the bus is the 19 MW ship propulsion motor drive. In addition to the propulsion load, there is a 1 MW ship service power supply consisting of a 12-pulse controlled rectifier, as well as a pulsed power load. A harmonic filter is present which reduces the harmonics caused by the electronic switching in the motor controllers and ship service power supply. The bus capacitance shown represents the stray bus capacitances.

A detailed description of each of these components follows, along with a brief discussion of the average-value modeling strategy as appropriate.

### Prime Mover

Since the focus of this effort was the representation of the electrical dynamics, the prime mover was assumed to be ideal and therefore the synchronous machine speed was assumed to be constant and the frequency 60 Hz.

### Synchronous Machine

The synchronous machine is a 2-pole, 21 MW (26.25 MVA), 4160 V (line-to-line), salient pole machine. The parameters are given in Table 1. The modeling of a synchronous machine has been reported previously by PCKA and therefore it is not repeated here [2].

Table 1. Synchronous machine parameters		
$P = 2$		
$r_s = 1.27 \text{ m}\Omega$	$L_{ls} = 391 \text{ }\mu\text{H}$	$L_{mq} = 2.51 \text{ }\mu\text{H}$
$r'_{kq} = 5.26 \text{ m}\Omega$	$L'_{lkq} = 157 \text{ }\mu\text{H}$	$L_{md} = 2.79 \text{ }\mu\text{H}$
$r'_{kd} = 4.74 \text{ m}\Omega$	$L'_{lkd} = 69.8 \text{ }\mu\text{H}$	
$r'_{fd} = 401 \text{ m}\Omega$	$L'_{lfd} = 227 \text{ }\mu\text{H}$	
$M_a = 3.73.6 \text{ H}^{-1}$	$M_d = 360.5 \text{ H}^{-1}$	$\tau_r = 1.90 \text{ H}^{-1}$

### Excitation System

The synchronous machine excitation system / voltage regulator is an IEEE Type 2. The block diagram is given in Fig. 2 and the parameters are listed in Table 2. These are reasonable parameters based on the size of the machine. Unfortunately, the parameters provided by the manufacturer, appear to be incorrect.

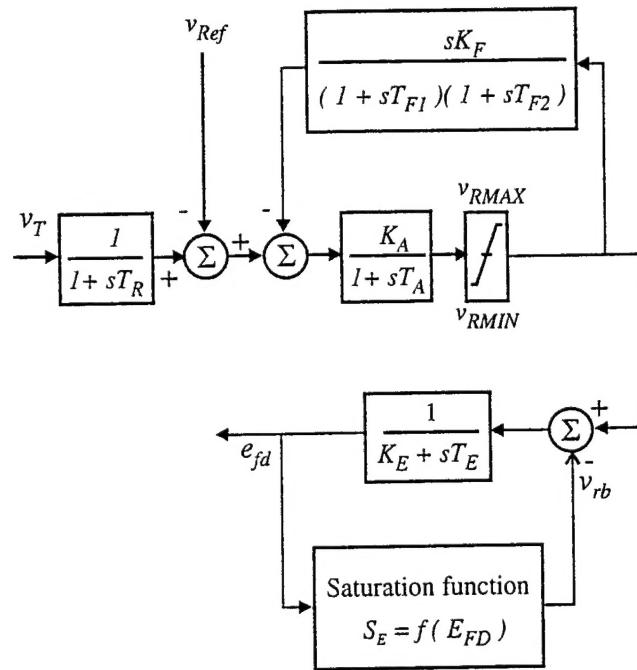


Figure 2. IEEE Type 2 exciter representation.

Table 2. Exciter parameter		
$v_{Ref} = 4160 \text{ V}$	$v_{RMAX} = 7.3 \text{ p.u.}$	$S_{E75} = 0.50$
$T_R = 0.8 \text{ s}$	$v_{RMIN} = 0 \text{ p.u.}$	$S_{E100} = 0.86$
$K_A = 400$	$K_F = 0.03$	$K_E = 1.0$
$T_A = 20 \text{ ms}$	$T_{F1} = 1 \text{ s}$	$T_E = 0.8 \text{ s}$
	$T_{F2} = 1 \text{ s}$	

### Induction Motor

The induction motor which is used for ship propulsion is a 150 rpm, 19 MW unit. The steady-state equivalent circuit is shown in Fig. 3 and the parameters for the five 3-phase set model are given in Table 3. Modeling of the 15-phase induction motor was a major technical challenge. Since this work may be of interest to a relatively large audience, a description of the modeling is documented in Appendix B.

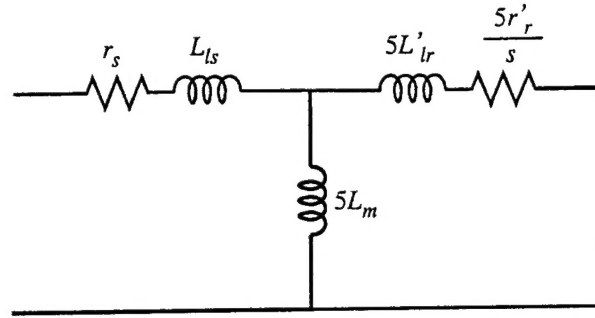


Figure 3. Per-phase equivalent circuit of 15-phase induction machine.

Table 3. Induction motor parameters.			
$L_{ls} = 6.79 \text{ mH}$	$L'_{lr} = 4.57 \text{ mH}$	$r_s = 122 \text{ m}\Omega$	$r'_r = 21.4 \text{ m}\Omega$
$L_{ms} = 58.1 \text{ mH}$	$n_{sr} = 0.373$	$P = 12$	

### Motor Controller

The induction motor power converter, which converts 4160 V, 3-phase ac to variable amplitude, variable frequency, 15-phase ac is shown in Fig. 4. The converter consists of three uncontrolled rectifiers connected to three dc links. Each dc link is connected to five H-bridge inverters (Fig. 5) and each H-bridge supplies one phase of the induction motor (Fig. 4). The parameters are given in Table 4.

Table 4. Induction motor power converter parameters.		
Symbol	Description	Value
	Effective thyristor on state resistance	10 m $\Omega$
	Effective thyristor off state resistance	100 $\Omega$
	Load commutated converter commutating inductance	10 $\mu\text{H}$
$L_{dc}$	DC link inductance	3 mH
$r_{dc}$	DC link resistance (associated with $L_{dc}$ )	10 $\mu\Omega$
$C_{dc}$	DC link capacitance	10 $\mu\text{F}$
	Effective diode voltage drop	5 V
	Effective thyristor voltage drop	8 V

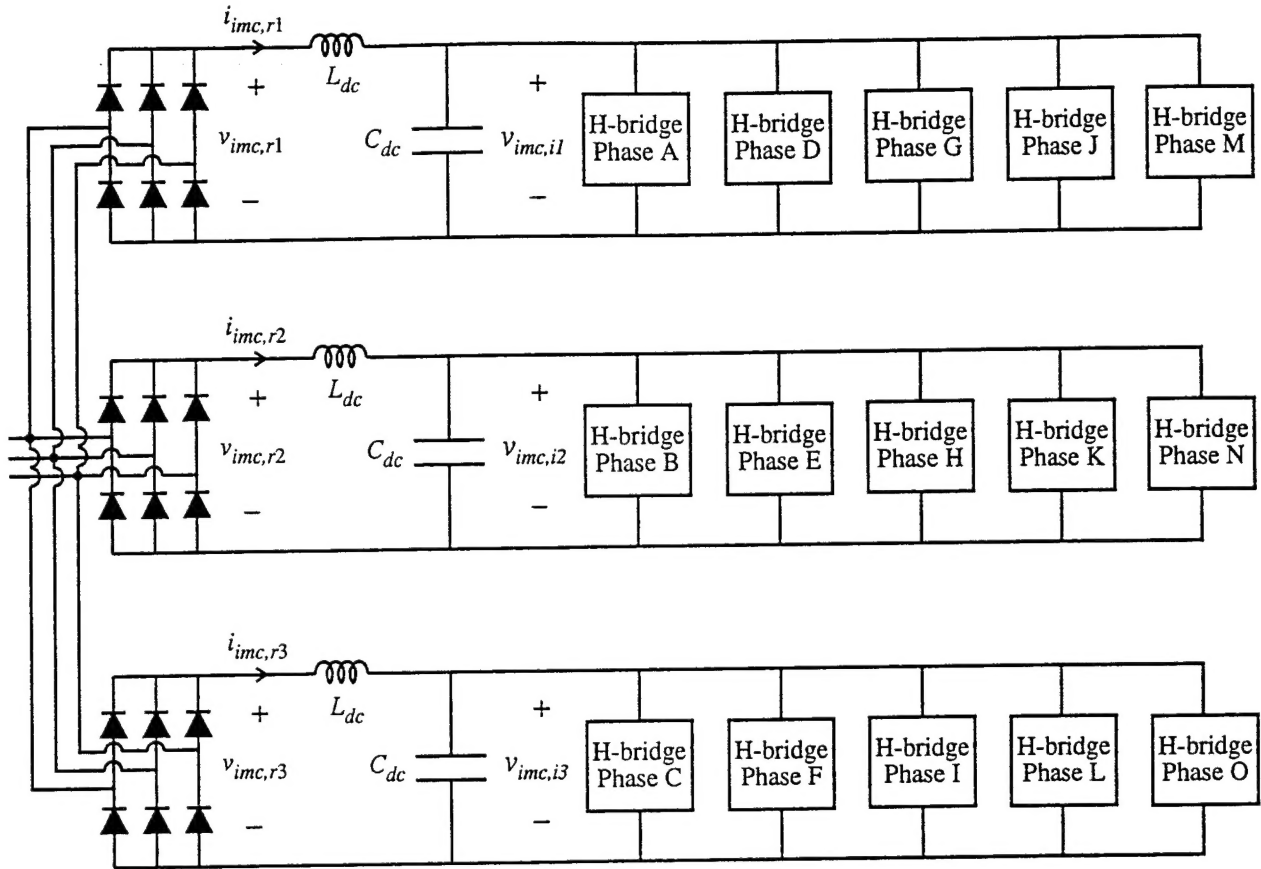


Figure 4. Induction motor power converter.

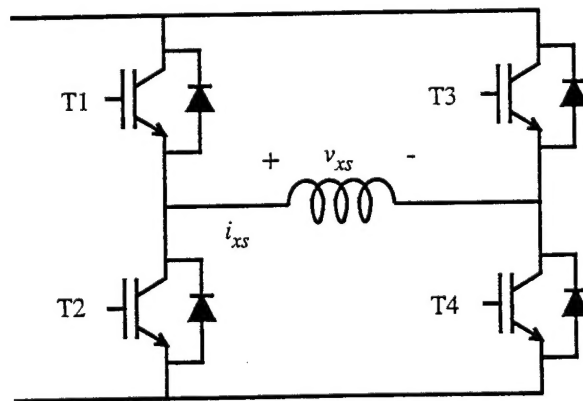


Figure 5. H-bridge.

The most difficult technical challenge of this project was the development of the appropriate algorithms to control each of the semiconductors in the 15 H-bridges. According to the manufacturer, the overall control strategy was to be based upon field oriented control. Furthermore, the control strategy was to be implemented in such a way that the switching frequency of the H-bridge semiconductors was to be constant. There were two principal difficulties in implementing such a control. First, since the machine is a 15-phase design, the interaction between the motor phases complicated the design of the current control loop. Secondly, and most importantly, it was discovered that if a standard field oriented control was used the induction motor propulsion drive would cause the system to become unstable. Therefore, a new concept which is denoted "link stabilizing field oriented control" was developed. This control acts much the same as a standard field oriented control with the exception that it does not cause the drive to exhibit the negative impedance instability as does the standard field-oriented control. This new concept in induction motor control has ramifications far beyond this system. It is described in detail in Appendices B and C.

### Ship Service Power Supply

The ship service power supply is depicted in Fig. 6. Therein,  $i_{xp}$ ,  $i_{xd}$ , and  $i_{xw}$  denote the x'th phase currents of the primary, delta-connected secondary, and wye-connected secondary transformers, respectively; the variables  $v_{abp}$ ,  $v_{abd}$ , and  $v_{abw}$  designate the a to b primary, delta-connected secondary, and wye-connected secondary transformer voltages, respectively. The rectifier voltage and current are denoted  $v_r$  and  $i_r$ . The transformer output voltage and current are denoted  $v_{dc}$  and  $i_{dc}$ . The individual SCR's of the upper load commutated converter are denoted D1-D6 and the SCR's of the lower converter are W1-W6. The rectifiers are connected in series and an LC filter is connected between the rectifier output and the load.

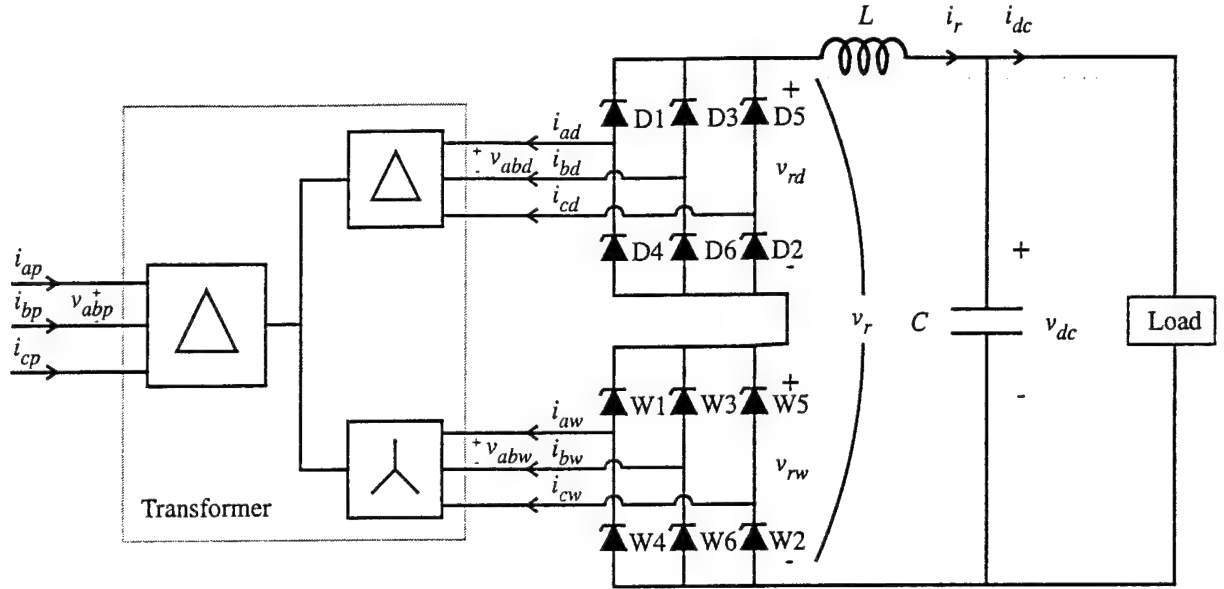


Figure 6. Power supply.

The supervisory control algorithm for the power supply is depicted in Fig. 7. Therein, the PI voltage control is the principal control loop with a current control to prevent over currents. The thyristor gate signals are fired based on the positive zero crossing (PZCD in Fig. 7) of the a to b delta connected secondary voltage. In particular, the individual thyristor valves are fired in accordance with Table 5.

Table 5. Thyristor turn on times			
SCR	Turn-on Time	SCR	Turn-on Time
D1	$\alpha / \omega_e$	W1	$(\alpha + 11\pi / 6) / \omega_e$
D2	$(\alpha + \frac{\pi}{3}) / \omega_e$	W2	$(\alpha + \pi / 6) / \omega_e$
D3	$(\alpha + \frac{2\pi}{3}) / \omega_e$	W3	$(\alpha + 3\pi / 6) / \omega_e$
D4	$(\alpha + \frac{3\pi}{3}) / \omega_e$	W4	$(\alpha + 5\pi / 6) / \omega_e$
D5	$(\alpha + \frac{4\pi}{3}) / \omega_e$	W5	$(\alpha + 7\pi / 6) / \omega_e$
D6	$(\alpha + \frac{5\pi}{3}) / \omega_e$	W6	$(\alpha + 9\pi / 6) / \omega_e$

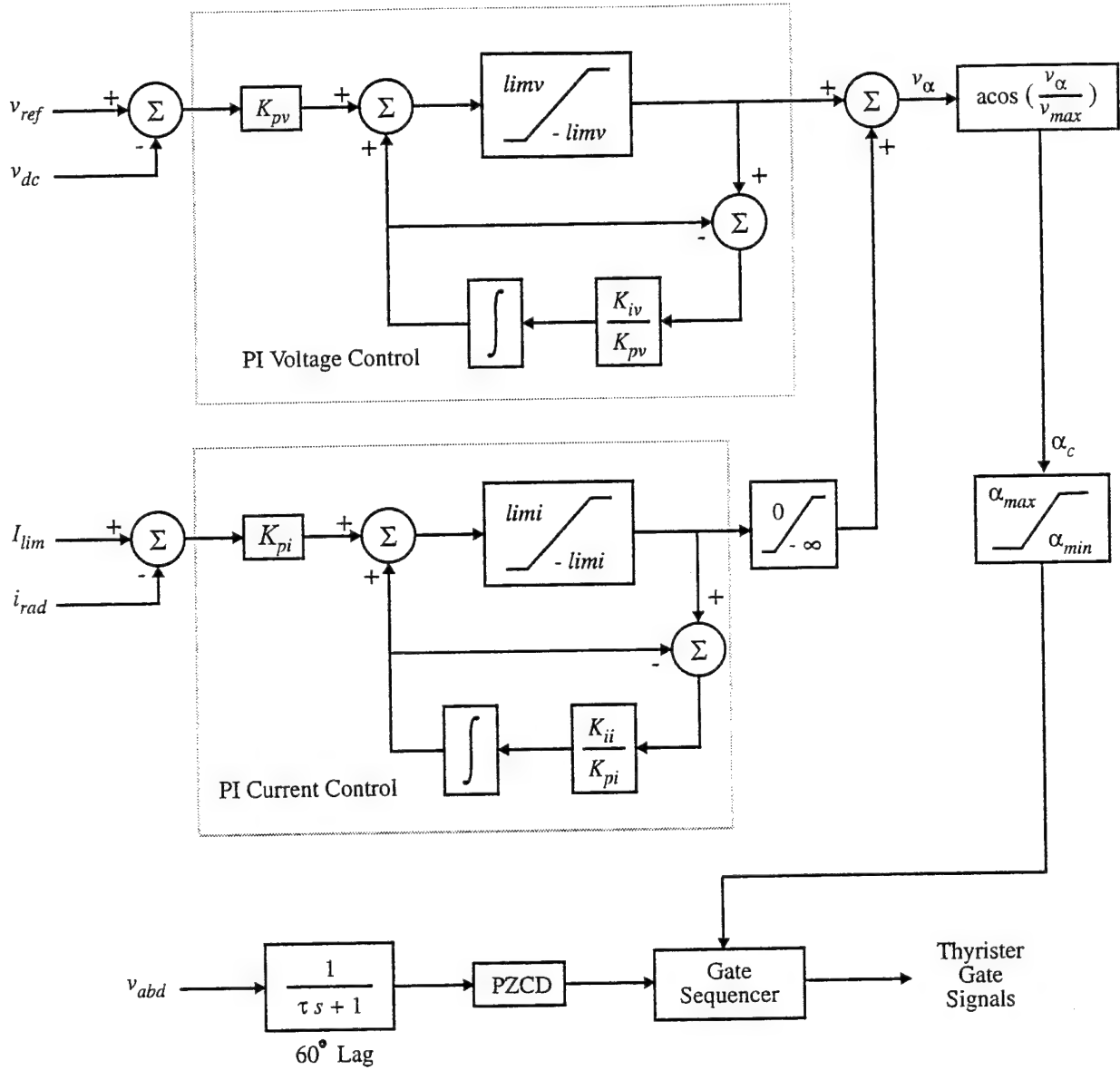


Figure 7. Power supply control algorithm.

Parameters of the ship service power supply are listed in Table 6; therein the transformer parameters are those of the simplified equivalent circuit shown in Fig. 8. Note that the primary leakage inductance is negative; this results from the fact that the primary leakage in Fig. 8 is actually an effective value based on several terms, not because any physical leakage is claimed to be negative [2].



Table 6. Power supply parameters

Symbol	Description	Value
$L_{ls}$	Secondary leakage inductance	28.2 mH
$r_s$	Secondary resistance	325 m $\Omega$
$N_p/N_d$	Primary effective turns / Delta-connected secondary effective turns (ratio to wye-connected secondary is selected to give the same line-to-line voltage)	9.8
$\hat{L}_{lp}$	Primary leakage inductance	-9.69 mH
$r_p$	Primary resistance	274 m $\Omega$
$L_{dc}$	Filter inductance	600 $\mu$ H
$r_{dc}$	Filter inductance resistance	1 m $\Omega$
$C_{dc}$	Filter capacitance	3200 $\mu$ F
	Thyristor off state resistance	100 $\Omega$
	Thyristor on state resistance	1 $\Omega$
$K_{pv}$	Voltage controller proportional gain	0.01
$K_{ip}$	Voltage controller integral gain	20/s
$\lim v$	Voltage regulator limit	10kV
$K_{pi}$	Current regulator proportional gain	0.01 V/A
$K_{ii}$	Current regulator integral gain	0 V/As
$\lim i$	Current regulator limit	10 kA
$\alpha_{\min}$	Minimum phase delay	0
$\alpha_{\max}$	Maximum phase delay	3.14 radians
$v_{\max}$	Maximum power supply output voltage	1147 V
$\tau$	Line-to-line voltage filter time constant	4.594 ms

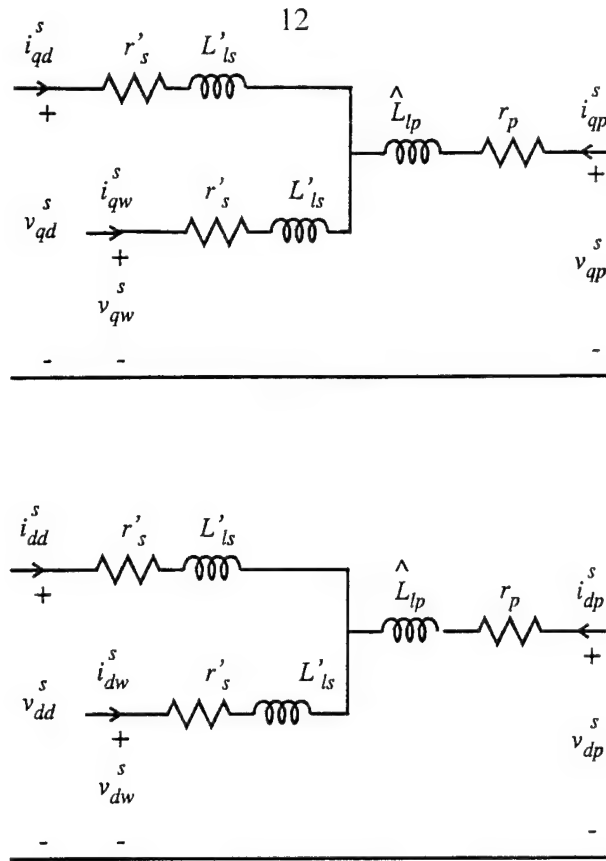


Figure 8. Power supply transformer simplified equivalent circuit.

The detailed computer model of the power supply was developed under previous Navy contracts [2]. The average-value model used in the studies, reported herein, was developed under this SBIR. Therefore, it is appropriate to set forth briefly the modeling strategy. The average-value model of the power supply is based upon the average-value model of a voltage behind inductance / controlled rectifier model. Although the system is a 12-pulse rectifier, it is convenient to consider the operation of a 6-pulse load commutated converter, as depicted in Fig. 9, before proceeding to the 12-pulse rectifier. Since an average-value model is desired, the known quantities will be considered to be the source voltage (in qd form) and the dc output voltage  $v_{dc}$ . The output of the model will be the fast-average q- and d-axis source currents and the fast-average of the rectifier current [3]. For this purpose, it is convenient to assume that the source voltage may be expressed in terms of q- and d- axis voltages as

$$v_{qg}^s = \sqrt{2} E \quad (1)$$

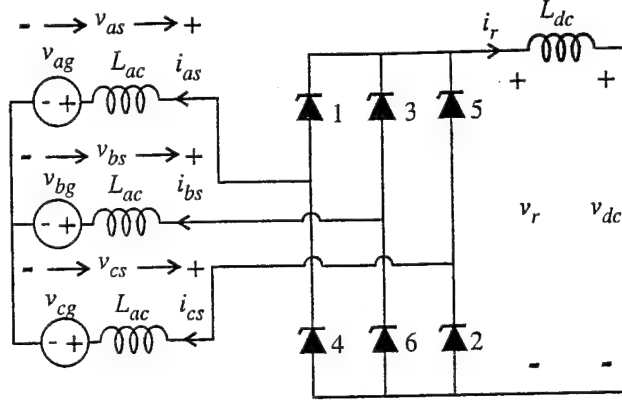


Figure 9. Equivalent circuit of 6-pulse power supply.

$$v_{dg}^g = 0 \quad (2)$$

where  $E$  is the rms magnitude of the source voltage. The d-axis voltage is zero; this can be obtained by appropriate selection of the reference frame. The reference frame is the source reference frame indicated by a superscript  $g$  and an angular displacement  $\theta_g$ .

In order to obtain the fast-average rectifier voltage and the q- and d-axis currents, it is convenient to note that these variables are periodic in  $\pi/3$  radians of  $\theta_g$ . Thus, the average may be taken over any  $\pi/3$  interval of  $\theta_g$ . It is convenient to consider the an interval which begins when a certain valve turns on and continues until the next valve is turned on. If the interval when valve 3 begins to conduct until valve 4 begins to conduct is selected

$$\bar{v}_r = \frac{3}{\pi} \int_{\frac{\pi}{3} + \alpha}^{\frac{2\pi}{3} + \alpha} (v_{bs} - v_{cs}) d\theta_g \quad (3)$$

In (3),  $\alpha$  is the firing angle relative to the source reference frame. In particular,  $\alpha$  is defined such that valve 3 fires when

$$\theta_g = \frac{\pi}{3} + \alpha \quad (4)$$

The average indicated in (3) may be carried out by noting from Fig. 9

$$v_{as} = v_{ag} + L_{ac} \frac{di_{as}}{dt} \quad (5)$$

$$v_{bs} = v_{bg} + L_{ac} \frac{di_{bs}}{dt} \quad (6)$$

$$v_{cs} = v_{cg} + L_{ac} \frac{di_{cs}}{dt} \quad (7)$$

Substitution of (5)-(7) into (3) yields

$$\bar{v}_r = \frac{3}{\pi} \int_{\frac{\pi}{3}+\alpha}^{\frac{2\pi}{3}+\alpha} (v_{bg} - v_{cg}) d\theta_g + \frac{\pi}{3} L_{ac} \omega_g (i_b - i_c) \Big|_{\frac{\pi}{3}+\alpha}^{\frac{2\pi}{3}+\alpha} \quad (8)$$

Equation (8) may be simplified by transforming (1) and (2) back to abc-variables, whereupon

$$v_{ag} = \sqrt{2} E \cos \theta_g \quad (9)$$

$$v_{bg} = \sqrt{2} E \cos \left( \theta_g - \frac{2\pi}{3} \right) \quad (10)$$

$$v_{cg} = \sqrt{2} E \cos \left( \theta_g + \frac{2\pi}{3} \right) \quad (11)$$

Substitution of (9) - (11) into (8) yields

$$\bar{v}_r = \frac{3\sqrt{3}}{\pi} \sqrt{2} E \cos \alpha + \frac{3}{\pi} L_{ac} \omega_g (i_b - i_c) \Big|_{\frac{\pi}{3}+\alpha}^{\frac{2\pi}{3}+\alpha} \quad (12)$$

Further simplification may be obtained by observing that, prior to the instant valve 3 begins to conduct, only valves 1 and 2 are conducting; therefore

$$\left| i_{abcg} \right|_{\theta_g = \frac{\pi}{3} + \alpha} = \begin{bmatrix} -\bar{i}_r & 0 & \bar{i}_r \end{bmatrix}^T \quad (13)$$

In (13), dc current ripple is neglected whereupon the instantaneous rectifier current is equal to it's fast-average value. Similarly, at the instant prior to valve 4 conducting only valves 2 and 3 are on, therefore

$$\left| i_{abcg} \right|_{\theta_g = \frac{2\pi}{3} + \alpha} = \begin{bmatrix} 0 & -\bar{i}_r - \Delta \bar{i}_r & \bar{i}_r + \Delta \bar{i}_r \end{bmatrix}^T \quad (14)$$

In (14),  $\Delta \bar{i}_r$  represents the change in the fast average of the rectifier current over the interval. It follows from this definition that the derivative of the fast-average of rectifier current may be approximated as

$$\frac{d\bar{i}_r}{dt} = \frac{\Delta \bar{i}_r}{\frac{3}{\pi}} \omega_g \quad (15)$$

Substitution of (13)-(15) into (12) yields the desired expression for the fast-average rectifier voltage,

$$\bar{v}_r = \frac{3\sqrt{3}}{\pi} \sqrt{2} E \cos \alpha - \frac{3}{\pi} L_{ac} \omega_g \bar{i}_r - 2L_{ac} \frac{d\bar{i}_r}{dt} \quad (16)$$

It is assumed, that the rectifier is connected to a dc-link inductor with inductance  $L_{dc}$  and resistance  $r_{dc}$ . This output voltage is denoted  $v_{dc}$  (Fig. 9). The voltage equation becomes

$$v_r = r_{dc} i_r + L_{dc} \frac{di_r}{dt} v_{dc} \quad (17)$$

The fast-average of (17) is

$$\bar{v}_r = r_{dc} \bar{i}_r + L_{dc} \frac{d\bar{i}_r}{dt} v_{dc} \quad (18)$$

Combining (16) with (18) yields

$$\frac{d\bar{i}_r}{dt} = \frac{\frac{3\sqrt{3}}{\pi} \sqrt{2} E \cos \alpha - \left(r_{dc} + \frac{3}{\pi} L_{ac} \omega_g\right) \bar{i}_r - \bar{v}_{dc}}{L_{dc} + 2L_{ac}} \quad (19)$$

It is necessary to calculate the average q- and d-axis source currents. In order to formulate the expressions for the average q- and d-axis currents, it is assumed that the rectifier current is constant throughout the interval and equal to its fast-average value. It is convenient to divide the interval into two parts in order to compute the average current; the commutation interval during which the current is transferred from valve 1 to valve 3, and the conduction interval during which only valves 2 and 3 are conducting. During the commutation interval, valves 1, 2, and 3 are conducting. Therefore, the current into the ac source must be of the form

$$i_{abcs} = [i_{as} \ -\bar{i}_r \ -i_{as} \ \bar{i}_r]^T \quad (20)$$

and

$$v_{as} - v_{bs} = 0 \quad (21)$$

Substitution of (5), (6), and (20) into (21) and solving for the a-phase current yields

$$i_{as}(\theta_g) = -\bar{i}_r + \frac{1}{L_{ac}\omega_g} \frac{\sqrt{3}}{2} \sqrt{2}E \left[ \cos(\alpha) - \cos(\theta_g - \frac{\pi}{3}) \right] \quad (22)$$

The commutation sub-interval ends when the current in valve 1, which is the a-phase current, becomes zero. The angle from the time valve 3 is turned on and valve 1 is turned off is known as the commutation angle  $u$ . It can be found by setting (22) equal to zero. In particular,

$$u = -\alpha + \arccos \left[ \cos \alpha - \frac{L_{ac}\omega_g \bar{i}_r}{E} \right] \quad (23)$$

After commutation, the a-phase current remains at zero, therefore

$$i_{abcs} = [0 \ -\bar{i}_r \ \bar{i}_r]^T \quad (24)$$

Equations (20), (22), and (24) specify the machine currents throughout the  $\pi/3$  interval which begins when valve 3 is fired.

The next step is to use the machine currents to calculate the average q- and d- axis currents, which are defined as

$$\bar{i}_{qs} = \frac{3}{\pi} \int_{\frac{\pi}{3}+\alpha}^{\frac{2\pi}{3}+\alpha} i_{qs}(\theta_g) d\theta_g \quad (25)$$

$$\bar{i}_{ds} = \frac{3}{\pi} \int_{\frac{\pi}{3}+\alpha}^{\frac{2\pi}{3}+\alpha} i_{ds}(\theta_g) d\theta_g \quad (26)$$

Since the form of machine currents is different in the conduction period than in the commutation period, it is convenient to break up (25) and (26) into components corresponding to those two intervals. In particular,

$$i_{qs} = i_{qs,com} + i_{qs,cond} \quad (27)$$

$$i_{ds} = i_{ds,com} + i_{ds,cond} \quad (28)$$

where

$$i_{qs.com} = \frac{3}{\pi} \int_{\frac{\pi}{3}+\alpha}^{\frac{\pi}{3}+\alpha+u} i_{qs}(\theta_g) d\theta_g \quad (29)$$

$$i_{qs.cond} = \frac{3}{\pi} \int_{\frac{\pi}{3}+\alpha+u}^{\frac{2\pi}{3}+\alpha} i_{qs}(\theta_g) d\theta_g \quad (30)$$

$$i_{ds.com} = \frac{3}{\pi} \int_{\frac{\pi}{3}+\alpha}^{\frac{\pi}{3}+\alpha+u} i_{ds}(\theta_g) d\theta_g \quad (31)$$

$$i_{ds.cond} = \frac{3}{\pi} \int_{\frac{\pi}{3}+\alpha+u}^{\frac{2\pi}{3}+\alpha} i_{ds}(\theta_g) d\theta_g \quad (32)$$

The commutation component of the current may be found by substituting (22) into (20), transforming the result to the source reference frame  $\omega_g$ , and then integrating in accordance with (29) and (31)

$$\begin{aligned} i_{qs.com} &= \frac{2\sqrt{3}}{\pi} \bar{i}_r \left[ \sin\left(u + \alpha - \frac{5\pi}{6}\right) - \sin\left(\alpha - \frac{5\pi}{6}\right) \right] \\ &\quad + \frac{3}{\pi} \frac{\sqrt{3}E}{L_{ac}\omega_g} \cos(\alpha) [\cos(u + \alpha) - \cos(\alpha)] + \\ &\quad + \frac{1}{4} \frac{3}{\pi} \frac{\sqrt{2}E}{L_{ac}\omega_g} [\cos(2u) - \cos(2\alpha + 2u)] \end{aligned} \quad (33)$$

$$\begin{aligned} i_{ds.com} &= \frac{2\sqrt{3}}{\pi} \bar{i}_r \left[ -\cos\left(u + \alpha - \frac{5\pi}{6}\right) + \cos\left(\alpha - \frac{5\pi}{6}\right) \right] \\ &\quad + \frac{3}{\pi} \frac{\sqrt{2}E}{L_{ac}\omega_g} \cos(\alpha) [\sin(u + \alpha) - \sin(\alpha)] + \\ &\quad + \frac{1}{4} \frac{3}{\pi} \frac{\sqrt{2}E}{L_{ac}\omega_g} [\sin(2u) - \sin(2\alpha + 2u)] - \frac{3}{\pi} \frac{\sqrt{2}E}{L_{ac}\omega_g} \frac{1}{2} u \end{aligned} \quad (34)$$

Similarly, the conduction component of the average currents may be expressed by transforming (24) to the source reference frame followed by the integration as set forth in (30) and (32)

$$i_{qs,cond} = \frac{2\sqrt{3}}{\pi} \bar{i}_r \left[ \sin\left(\alpha + \frac{7\pi}{6}\right) - \sin\left(\alpha + u + \frac{5\pi}{6}\right) \right] \quad (35)$$

$$i_{ds,cond} = \frac{2\sqrt{3}}{\pi} \bar{i}_r \left[ -\cos\left(\alpha + \frac{7\pi}{6}\right) + \cos\left(\alpha + u + \frac{5\pi}{6}\right) \right] \quad (36)$$

The block diagram of the basic rectifier model is illustrated in Fig. 10. Therein, the inputs are the firing angle  $\alpha$ , the q- and d-axis source voltage in an arbitrary reference frame  $v_q^a$  and  $v_d^a$ , and the dc output voltage  $v_{dc}$ . The outputs of the model are the fast-average of the rectifier current  $\bar{i}_r$  and the fast-average of the q- and d- axis currents in the arbitrary reference frame  $\bar{i}_{qg}^a$  and  $\bar{i}_{dg}^a$ . The calculation in Block 1 determines the peak magnitude of the source voltage  $\sqrt{2}E$ .

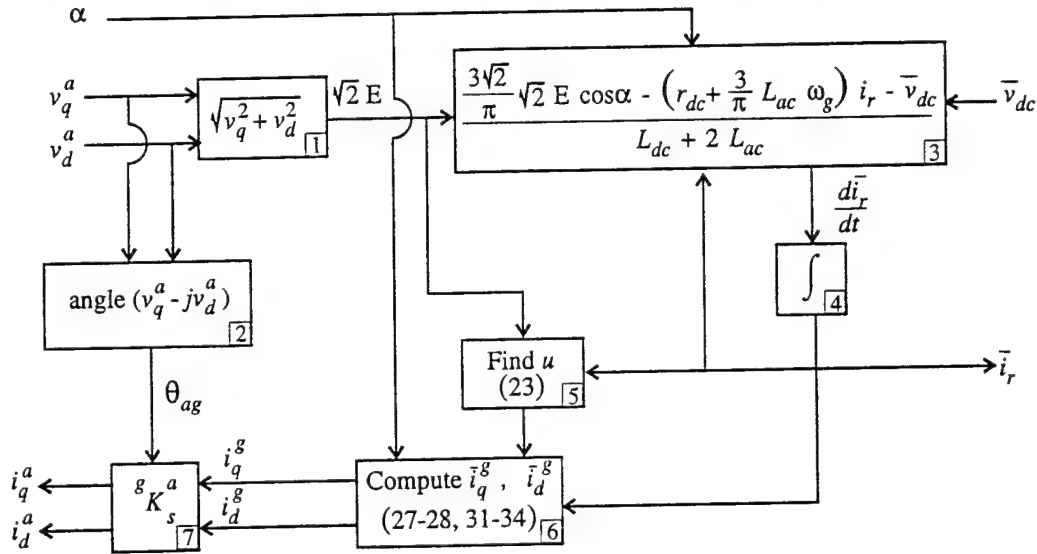


Figure 10. Diagram of rectifier model for 6-pulse power supply.

The calculation in Block 2 determines the angle of the source reference frame relative to the reference frame in which the qd voltages are inputs. This calculation is necessary since the q- and d- axis currents are calculated in the source reference frame ( $\omega_g$ ) which may not be the reference frame in which the voltages are input to the rectifier model. With the magnitude of the source voltage and the dc-link voltage, the time derivative of the rectifier current can be calculated (Block 3), which is integrated in order to determine the fast-average rectifier current  $\bar{i}_r$  (Block 4). With the rectifier current, the magnitude of the source voltage, and the firing angle, the commutation angle can be calculated using (23), (Block 5). Based upon the rectifier current,



the commutation angle, and the firing angle, the q- and d-axis currents are calculated in the source reference frame using (27), (28), and (33) - (36) in Block 6. Finally the q- and d- axis currents, in the source reference frame, are transformed to the arbitrary reference frame in Block 7.

The rectifier model in Fig. 10 is for a 6-pulse rectifier as depicted in Fig. 9. In order to modify the model to accommodate the 12-pulse rectifier, it should be noted that as long as the commutation angle is less than  $\pi/6$ , the two 6-pulse rectifiers will not interact. In other words, each rectifier can be analyzed separately, ignoring the current in the other rectifier. A detailed explanation of the interaction between 6-pulse units can be found in [4]. The changes in the structure of the model are, (1) the output voltage  $\bar{v}_r$  is doubled since there are two rectifiers connected in series, and (2) the current into the source (the primary current) is also doubled. The model is illustrated in Fig. 11. An additional modification has been incorporated in order to account for the turns ratio of the transformer; the model in Fig. 11 is referred to the secondary of the transformer.

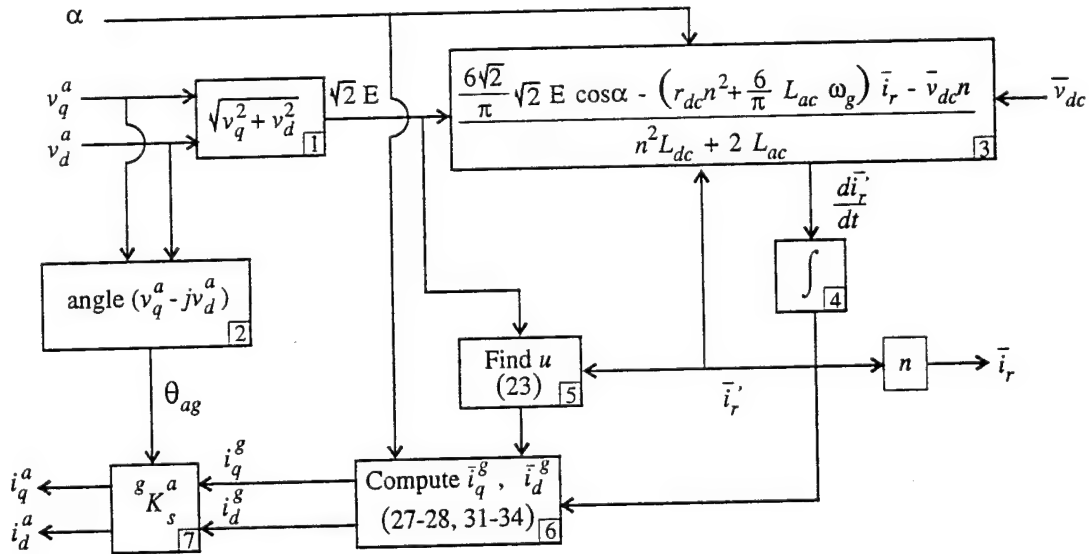


Figure 11. Diagram of rectifier model for 12-pulse power supply.

In order to complete the average-value model, it is necessary to integrate the rectifier model depicted in Fig. 11 with the model of the output capacitor shown in Fig. 6 and to add the model

of the controls shown in Fig. 7. It is clear, that the capacitor voltage (in average-value form) can be calculated from

$$p\bar{v}_{dc} = \frac{\bar{i}_r - \bar{i}_{dc}}{C_{dc}} \quad (37)$$

An interesting aspect of the modeling is representing the single-phase filter, the positive zero crossing detector, and the gate sequencer in average-value qd form. This is somewhat involved since the firing angle is determined by the controller  $\alpha_c$  (Fig. 7) relative to the filtered  $a$  to  $b$  delta connected secondary voltage whereas the firing angle required in the rectifier model is relative to the primary voltage. The firing of the power supply thyristors is derived from the filtered zero crossing of the  $a$  to  $b$  delta connected secondary voltage. This first-order low-pass filter has a time constant such that it introduces a  $60^\circ$  phase lag. In terms of abc variables,

$$\frac{d\tilde{v}_{abd}}{dt} = \frac{v_{ad} - v_{bd} - \tilde{v}_{abd}}{\tau} \quad (38)$$

For the purpose of representing the filter as an average-value model, it is convenient to treat the system as if each line-to-ground voltage is filtered individually and then subtracting the b-phase voltage from the a-phase voltage in order to determine  $v_{abd}$ . The 3-phase set of filters may be represented in fast-average qd form as

$$\frac{d\tilde{v}_{qd}}{dt} = \frac{1}{\tau} (v_{qd} - \tilde{v}_{qd}) - \omega_e \tilde{v}_{dd} \quad (39)$$

$$\frac{d\tilde{v}_{dd}}{dt} = \frac{1}{\tau} (v_{dd} - \tilde{v}_{dd}) + \omega_e \tilde{v}_{qd} \quad (40)$$

where  $v_{qd}$  and  $v_{dd}$  are the q- and d-axis delta connected secondary voltages,  $\tilde{v}_{qd}$  and  $\tilde{v}_{dd}$  are the corresponding filtered secondary voltages, and  $\omega_e$  is the speed of the synchronous reference frame.

The voltages  $v_{qd}$  and  $v_{dd}$  are not directly available from the model; instead they are calculated with a reduced-order representation of the circuit depicted in Fig. 8. In particular,  $v_{qd}$  and  $v_{dc}$  may be estimated as

$$v_{qd} = \left[ \frac{1}{2} r'_s i_{qp} - \omega_e \left( \frac{1}{2} L'_{ls} + \hat{L}_{lp} \right) i_{dp} \right] / n \quad (41)$$

$$v_{dd} = \left[ \frac{1}{2} r'_s i_{qp} - \omega_e \left( \frac{1}{2} L'_{ls} + \hat{L}_{lp} \right) i_{qp} \right] / n \quad (42)$$

The electrical dynamics are neglected in (41) and (42); however, this does not introduce any noticeable inaccuracy since the time constant of the filter is relatively large.

The filtered a- to b- phase line-to-line voltage may be expressed

$$v_{abd} = \sqrt{2} v_{sd} \cos(\theta_e + \tilde{\phi}_{vd}) \quad (43)$$

where  $v_{qd}$  is the rms amplitude and

$$\phi_{vd} = \text{angle}(\tilde{v}_{qd} - j\tilde{v}_{dd}) \quad (44)$$

In (44),  $j = \sqrt{-1}$ . The positive zero crossing of  $v_{abd}$  (43) occurs at

$$\theta_e = -\tilde{\phi}_{vd} - \frac{\pi}{2} \quad (45)$$

The gate sequencer will turn on valve 3 of the delta-connected rectifier at an angle of  $\alpha_c + 2\pi/3$  after the zero crossing, which occurs when the position of the synchronous reference frame is at

$$\theta_e = -\tilde{\phi}_{vd} + \frac{\pi}{6} + \alpha_c \quad (46)$$

Recall, from the derivation of the reduced-order model, valve 3 fires at an angle of  $\alpha_c + \pi/3$  past the peak value of the a-phase voltage, which is

$$\theta_e = \frac{\pi}{3} + \alpha - \phi_{vp} \quad (47)$$

where

$$\phi_{vp} = \text{angle}(v_{qp} - jv_{dp}) \quad (48)$$

Comparing (47) and (46) yields the expression for the effective firing angle relative to the source voltage

$$\alpha = \alpha_c + \phi_{vp} - \tilde{\phi}_{vd} - \frac{\pi}{6} \quad (49)$$

A block diagram of the average-value model of the gating controls is shown in Fig. 12.

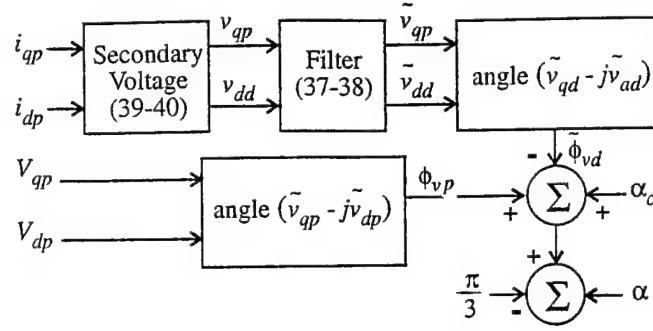


Figure 12. Average-value model of gate control.

### Pulsed Power Weapon

The pulsed power weapon considered is shown in Fig. 13. It consists of a 6-pulse rectifier with a LC pulse forming network interfaced to the system by a wye-to-wye transformer. The rectifier is controlled so as to gradually charge the capacitor which is then suddenly discharged. The control of the pulsed power unit is divided into three parts; a charge profile generator, a firing angle control, and a gate sequencer.

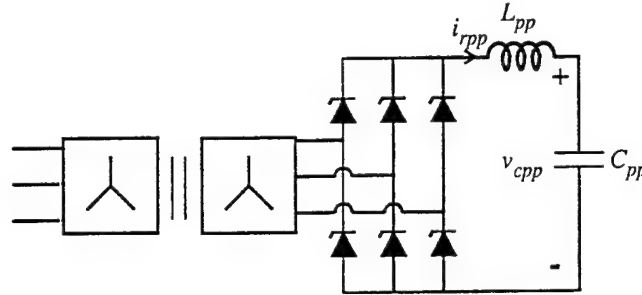


Figure 13. Pulsed power charger.

The charging profile control (Fig. 14) generates the commanded capacitor voltage as a function of time. As shown in Fig. 14, the capacitor voltage increases linearly to a prescribed value of over a time interval  $t_{ch}$ . The voltage command then remains constant for  $t_{ca}$ . This brief period is used to allow the rectifier to finish charging the capacitor to the final value. After this period is concluded, the firing of the rectifier is disabled and gating signals cease. The period  $t_{off}$  is provided to allow any remaining thyristor valves to commutate off. The cycle is completed with the time  $t_d$  during which the capacitor is discharged.

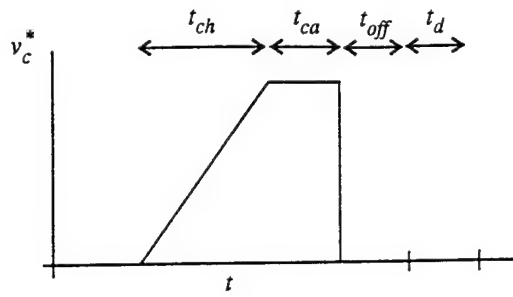


Figure 14. Charging profile generator.

The firing angle control varies the converter firing angle so that the capacitor voltage tracks the desired voltage established by the charging profile generator. This control is illustrated in Fig. 15. Therein, the commanded capacitor voltage  $v_{cpp}^*$  is compared to the actual capacitor voltage  $v_{cpp}$  and the difference is multiplied by a gain and limited to give the current command  $i_{rpp}^*$ . The difference between the commanded rectifier current and the actual current  $i_{rpp}$  is then multiplied by a proportional gain and the result added to the capacitor voltage to obtain the rectifier voltage command  $v_{rpp}^*$ . The capacitor voltage is included in the rectified voltage command since it decouples the capacitor and inductor. Finally, the voltage command is divided by the maximum rectifier voltage  $V_{rmax}$ , limited, and translated into a commanded firing angle  $\alpha_{cpp}$ .

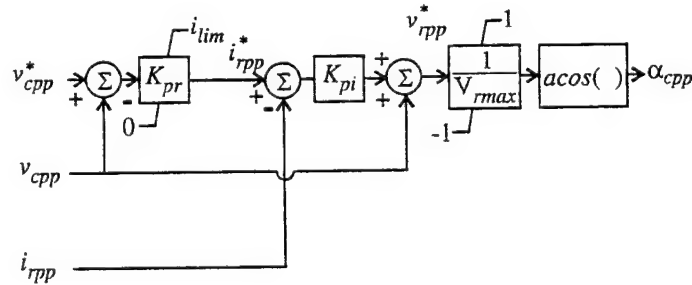


Figure 15. Firing angle control.

The gate sequencer is illustrated in Fig. 16 and is considerably different from that used for the power supply. In particular, all three line-to-line voltages are filtered, and the firing of individual valves is timed (via the delay blocks) from either the positive or negative zero crossings of line-to-line voltages as indicated in Fig. 16. Each DELAY block represents a delay

of radians from the zero crossing. In this control the firing angle is updated 6 times every cycle rather than once a cycle as in the case of the power supply. Parameters of the charging profile generator, the firing angle control, and the gate sequence are given in Table 7.

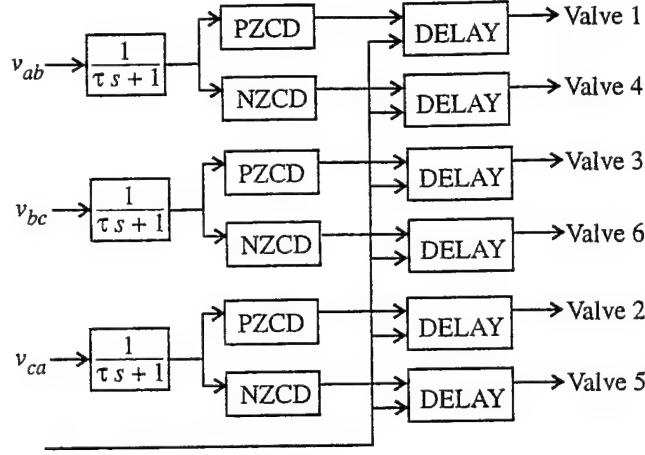


Figure 16. Gate sequencer.

The average-value modeling of the pulsed power weapon is based on the 6-pulse load-commutate converter model set forth previously in the derivation of the power supply. The significant differences are; (1) an extension to the 12-pulse case is not necessary, and (2) the representation of the gate sequence control is different. In order to derive an average-value model of the gate sequence controls it is appropriate to begin with the abc model of the filter. In particular

$$\frac{dv_f}{dt} = \frac{1}{\tau} \begin{pmatrix} 1 & -1 & 0 \\ 0 & 1 & -1 \\ -1 & 0 & 1 \end{pmatrix} v_{abc} - v_f \quad (50)$$

where  $v_f$  is the filtered voltage vector,

$$v_f = [\tilde{v}_{ab} \ \tilde{v}_{bc} \ \tilde{v}_{ca}]^T \quad (51)$$

Transforming (51) to the synchronous reference frame yields

$$\frac{dv_{qf}}{dt} = \frac{1}{\tau} \left( \frac{3}{2} v_{qp} + \frac{\sqrt{3}}{2} v_{dp} - v_{qf} \right) - \omega_e v_{df} \quad (52)$$

Table 7. Pulsed Power Parameters.		
Name	Description	Value
$t_{ch}$	Charge time	0.8 s
$t_{ca}$	Catch-up time	0.1 s
$t_{off}$	Off time	0.05 s
$t_d$	Dead time	0.05 s
$C$	Pulse Forming capacitance	4 F
$L$	Pulse forming inductance	3.21 mH
$r$	Resistance at pulse forming inductance	2.42 m $\Omega$
$L_l$	Transformer leakage inductance	64.3 $\mu$ H
$r_l$	Transformer resistance	2.42 m $\Omega$
$n_{ps}$	Transformer primary-to-secondary turns ratio	5.00
$K_{pi}$	Current gain	0.3213 V/A
$K_{pv}$	Voltage gain	80 A/V
$L_{lim}$	Current limit	6 KA
$\tau$	Filter time constant	4.594 ms
$V_c^*$	Maximum charging voltage	1000 V

$$\frac{dv_{df}}{dt} = \frac{1}{\tau} \left( \frac{\sqrt{3}}{2} v_{qp} + \frac{3}{2} v_{dp} - v_{df} \right) - \omega_e v_{df} \quad (53)$$

Together (52) and (53) are used to represent the average-value model of the filter. From these equations note that the b to c voltage may be expressed

$$v_{bc} = \sqrt{2} v_{sf} \cos \left( \theta_e - \frac{2\pi}{3} + \phi_{fpp} \right) \quad (54)$$

where

$$\phi_{fpp} = \text{angle}(v_{qf} + jv_{df}) \quad (55)$$

from which it can be seen that the positive zero crossing of the filtered b to c line-to-line voltage occurs at

$$\theta_e = \frac{\pi}{6} - \phi_{fpp} \quad (56)$$

Thus, valve 3 is fired when the position of the synchronous reference frame is

$$\theta_e = \frac{\pi}{6} - \phi_{fpp} + \alpha_c \quad (57)$$

By definition, valve 3 fires at an angle  $\alpha + \pi/3$  after the peak of the a-phase primary voltage.

This voltage may be expressed as

$$v_{ap} = \sqrt{2}v_s \cos(\theta_e + \phi_v) \quad (58)$$

where

$$\phi_v = \text{angle}(v_q - jv_d) \quad (59)$$

Therefore, valve 3 fires at

$$\theta_e = \alpha + \frac{\pi}{3} - \phi_v \quad (60)$$

Comparing (60) to (57)

$$\alpha = \alpha_c + \phi_v - \phi_{fpp} - \frac{\pi}{6} \quad (61)$$

The average value model of the pulsed power system is illustrated in Fig. 17.

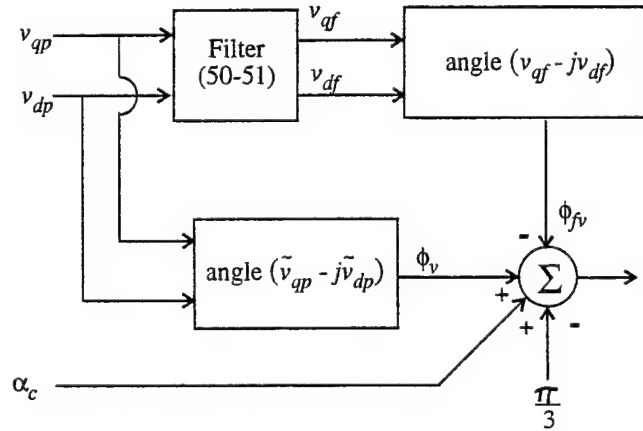


Figure 17. Average-value model of pulsed power gate sequencer.



## Harmonic Filter

In order to reduce the harmonic content at the ac bus, a wye-connected series RLC filter is used (Fig. 18). In the detailed computer model, this filter is represent in terms of abc variables as

$$\frac{dv_{abcf}}{dt} = \frac{1}{C_f} i_{abcf} \quad (62)$$

$$\frac{di_{abcf}}{dt} = \frac{1}{L_f} (v_{abc} - v_{abcf} - r_f i_{abcf}) \quad (63)$$

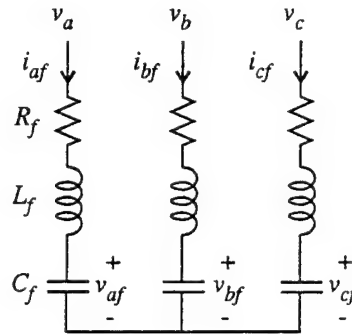


Figure 18. Harmonic filter.

For the purpose of the average-value model, it is convenient to represent (62) and (63) in the synchronous reference frame

$$\frac{dv_{qdf}}{dt} = \frac{1}{C_f} i_{qdf} - \omega_e \begin{bmatrix} 0 & 1 \\ -1 & 0 \end{bmatrix} v_{qdf} \quad (64)$$

$$\frac{di_{qdf}}{dt} = \frac{1}{L_f} (v_{qd} - v_{qdf} - r_f i_{qdf}) + \omega_e \begin{bmatrix} 0 & 1 \\ -1 & 0 \end{bmatrix} v_{qd} \quad (65)$$

The filter parameters are given in Table 8.

Table 8. Harmonic Filter		
$L = 8.04 \text{ mH}$	$R = 0.319 \text{ } \Omega$	$C = 35 \text{ } \mu\text{H}$

## Hydrodynamic Model

The hydrodynamic model used in the representation of the ship propulsion system is

$$\frac{d\omega_{rm}}{dt} = \frac{1}{J}(T_e - T_L) \quad (66)$$

where  $T_e$  is the induction motor torque and  $T_L$  is the load torque represented by

$$T_L = T_{L,base} \text{sgn}(\omega_{rm}) \left( \left| \frac{\omega_{rm}}{\omega_{rm,base}} \right| \right) \quad (67)$$

The assumed value of parameters are listed in Table 9. This model is over simplified with the inertia selected low compared to the actual system. A more detailed model can be readily substituted for the model presented herein if the actual hydrodynamic data is available.

Table 9. Hydrodynamic Model			
$J = 50 \mu Nms^2$	$\omega_{rmh} = 15.51 \text{ rad / s}$	$N = 3$	$T_{Lbs} = 1.2 \text{ MNm}$

## Component Model Interconnection

Model component interconnection is always an issue in detailed and average-value modeling. In a previous SBIR, PCKA developed interconnection strategy based on neglecting fast transients [5]. In this present SBIR, an alternate approach of retaining those transients has been explored. This is accomplished conveniently by representing a small capacitance at the ac bus. Although this introduces artificially fast time constants, these fast time constants do not present the same difficulties which are introduced in the case of detailed simulations since the fast time constants are not repeatedly excited. Therefore, integration algorithms applicable to stiff systems such as Gear's Method, are effective. In terms of q- and d-variables, the capacitor is represented as

$$\frac{dv_q}{dt} = \frac{1}{C} \sum_{j=1}^N i_{qj} - \omega_e v_d \quad (68)$$

$$\frac{dv_d}{dt} = \frac{1}{C} \sum_{j=1}^N i_{dj} - \omega_e v_q \quad (69)$$

Equation (68) and (69) establish the ac bus voltage as state variables. The capacitance  $C$  in (68) and (69) was selected as  $10\text{ }\mu\text{F}$ .

## COMPUTER STUDIES

Results of several computer studies are given in this section for the purposes of demonstrating the facility of the detailed and reduced-order simulations of the IPS shown in Fig. 1 and to compare the system response predicted by the detailed and reduced-order simulations. Four studies are given. With the exception of Study 2, each is divided into two parts. In part "a" the system response predicted by the detailed simulation is given; in part "b" the predicted reduced-order response is shown. In most cases, the studies are self-explanatory; therefore a lengthy discussion is not given. When evaluating the studies, it is convenient to refer to Fig. 1 and a listing of the variables plotted for the detailed and reduced-order simulations. For convenience Fig. 1 and the list of variables plotted are repeated at the beginning of each study.

### Study 1

In this study, the IPS is initially operating in the steady state with the ship service power supply operating at full load; however, the pulsed power system is out-of-service. At  $t = 15.5$ , the torque command of the vector controlled 15-phase propulsion induction motor is increased from zero to  $1.2 \text{ MN}\cdot\text{m}$  (full load). The dc bus stabilizer is incorporated into the vector control of the induction motor.

There are some differences between the system responses predicted by the detailed and the reduced-order simulations. These are due primarily to the fact that PCKA has not been totally successful in developing a reduced-order model of two or more converters operating in parallel from the same bus. Nevertheless, the accuracy is certainly acceptable for this application.

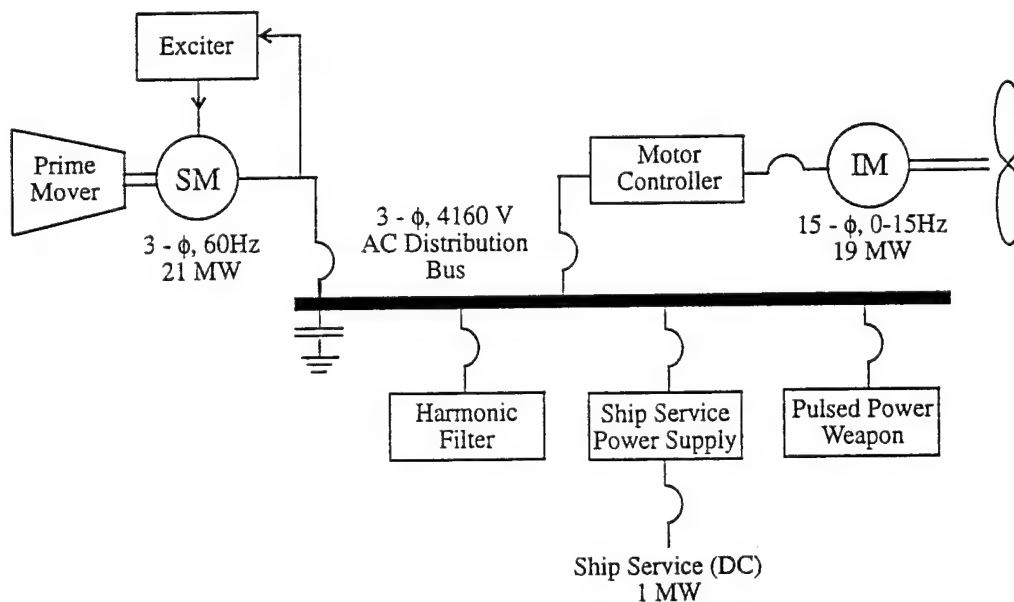
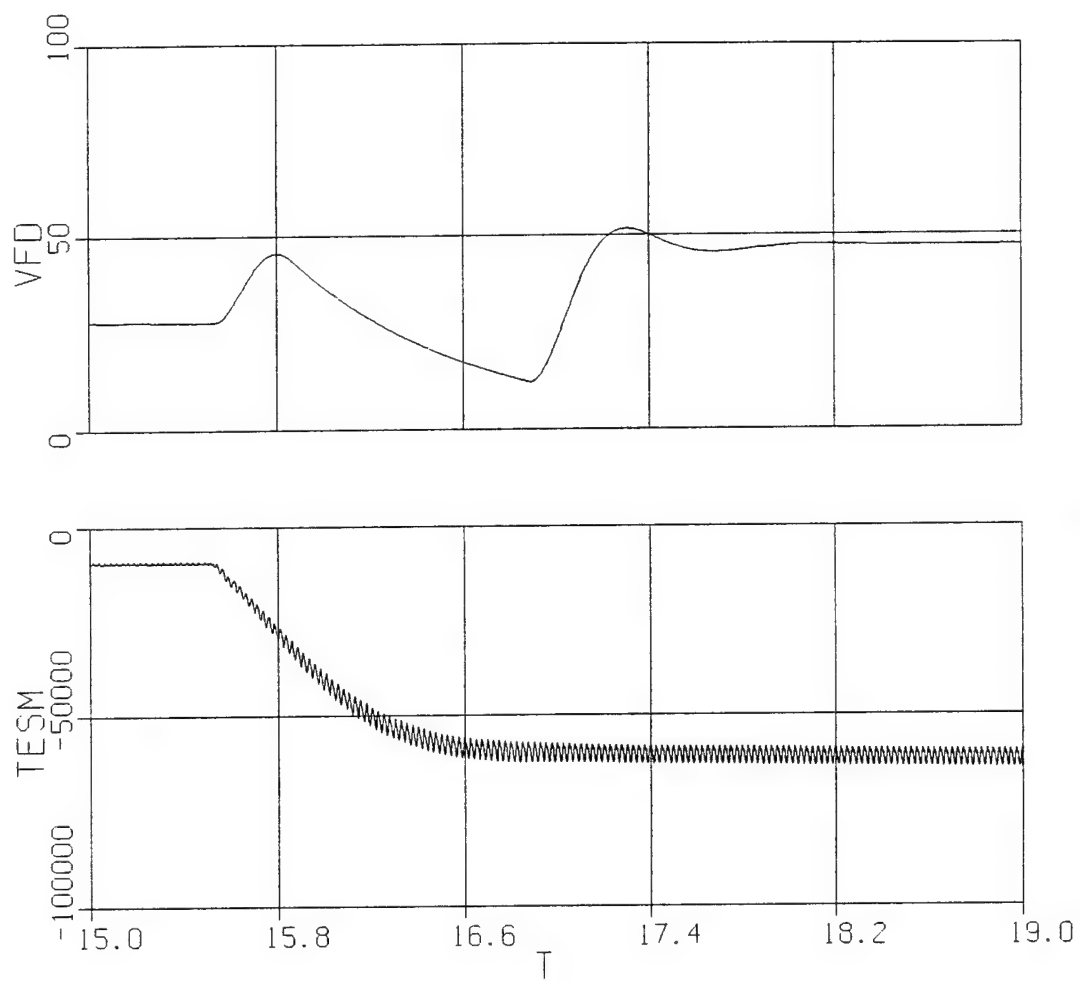


Figure 1. System studied.

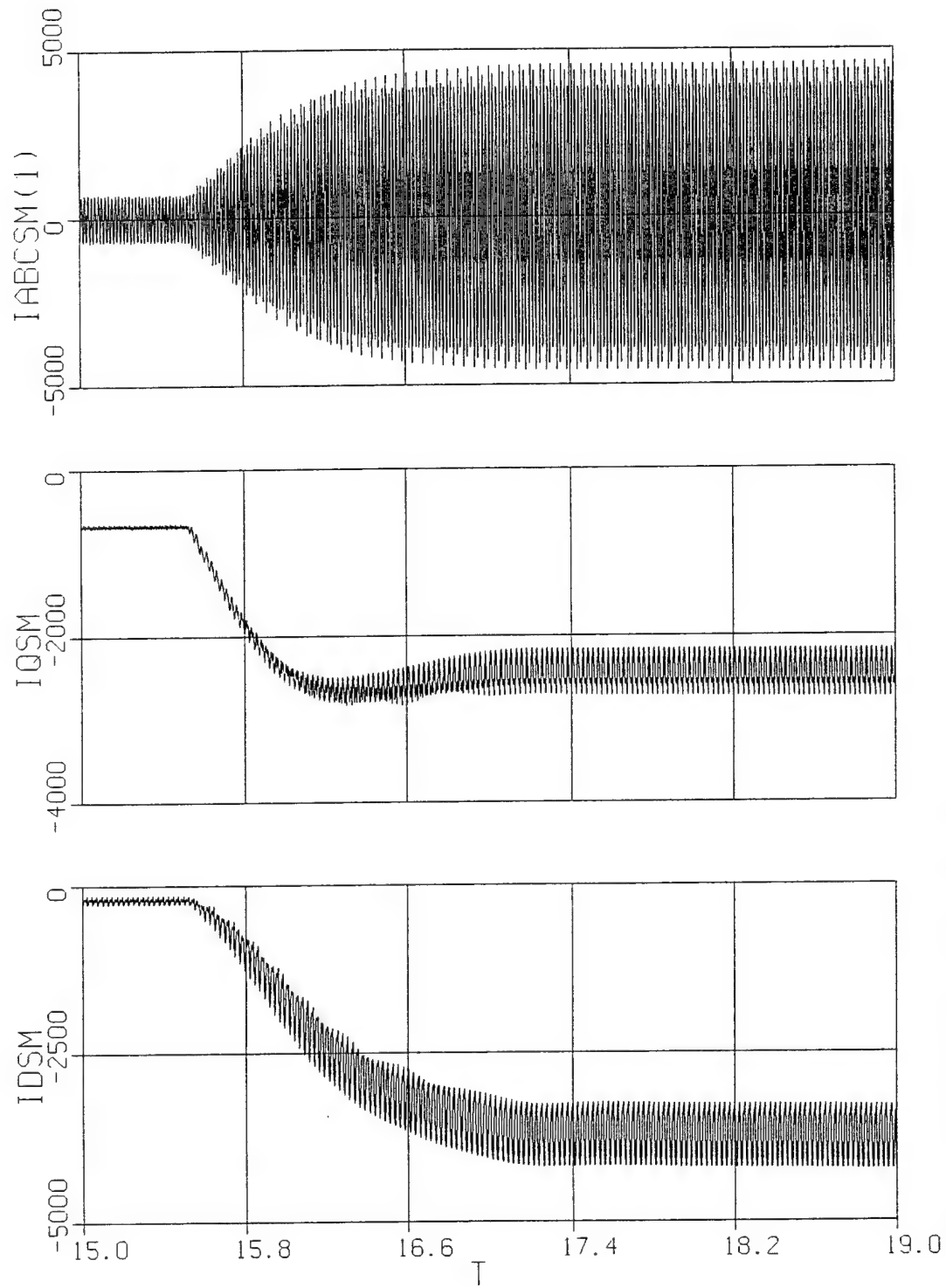
**Study 1a**

## Variable Description - Detailed Simulation

<u>ACSL Name</u>	<u>Description</u>
alphapwsp	power supply rectifier phase delay (rad)
iabcimc(1)	a-phase current into induction motor power converter (A)
iabcpw(1)	a-phase current into pulse power device (A)
iabcpwsp(1)	a-phase current into power supply (A)
iabscm(1)	a-phase synchronous machine current (positive in) (A)
iaoml(1)	a-phase induction motor current (A)
idcll	dc current into first 5 H-bridge inverter (not filtered) (A)
idcllf	low pass filtered inverter current into first set of five H-bridges (filtered so it could be compared to average value model) (A)
iddrv	d-axis current into induction motor power converter (A)
idppw	d-axis current into pulse power device (A)
idpwsp	d-axis current into power supply (A)
idsm	d-axis synchronous machine current (positive in) (A)
iqdrv	q-axis current into induction motor power converter (A)
iqppw	q-axis current into pulse power device (A)
iqpwsp	q-axis current into power supply (A)
iqsm	q-axis synchronous machine current (positive in) (A)
irectpwsp	dc link current in power supply (positive out of rectifier) (A)
irppw	inductor current in pulse power device (A)
teiml	induction motor electromagnetic torque (Nm)
tesm	synchronous machine torque (positive for motor operation) (Nm)
vabc(1)	a-phase 4160 V bus voltage (V)
vaoiml(1)	a-phase induction motor voltage (V)
vcappw	capacitor voltage of pulse power device (A)
vd	d-axis bus voltage (V)
vdcll	dc voltage at input of first 5 H-bridges (V)
vdcpwsp	power supply dc output voltage (V)
vfd	synchronous machine field voltage (unreferred) (V)
vq	q-axis bus voltage (V)
wrmiml	induction motor speed - mechanical (rad/s)

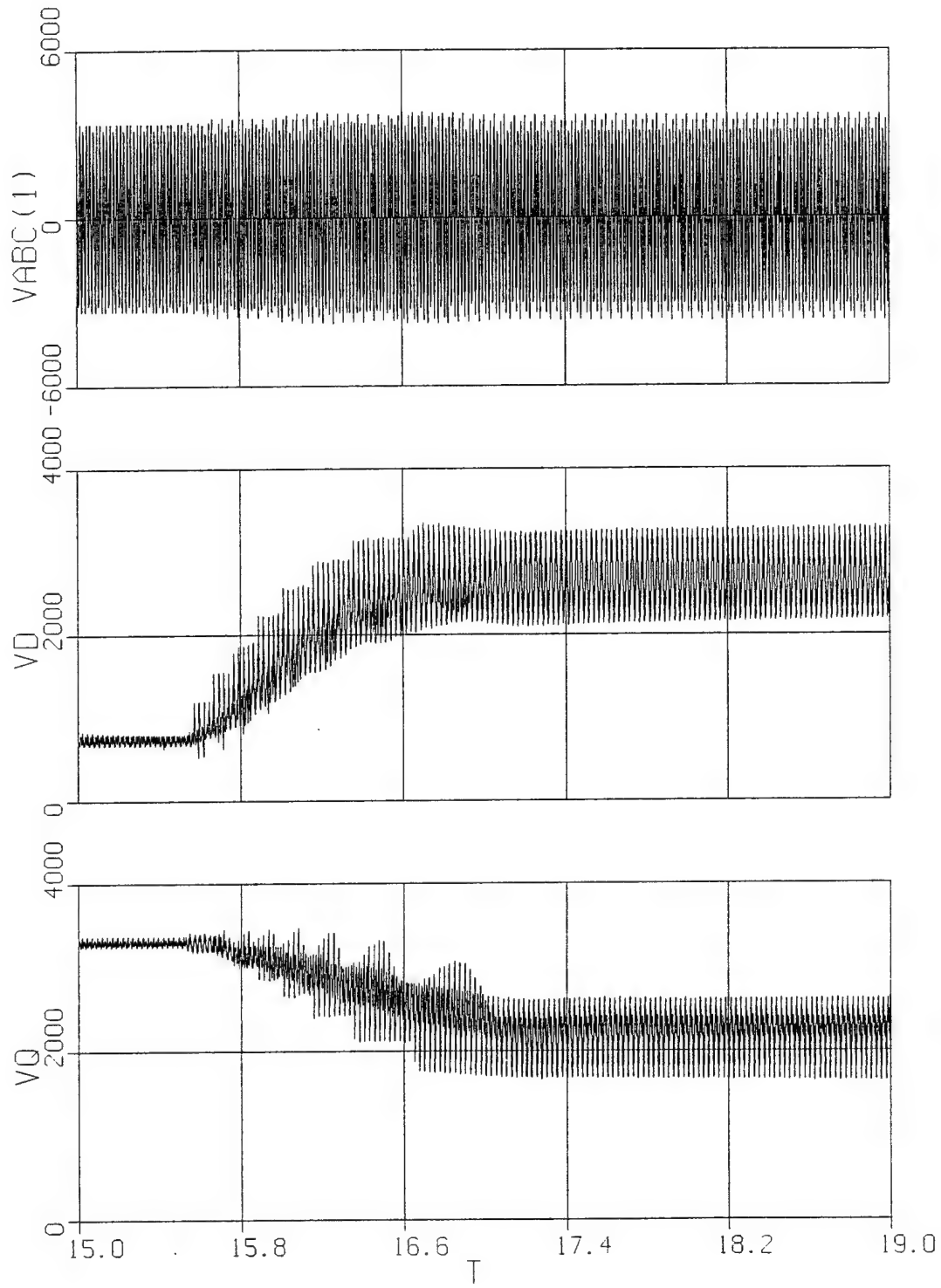


4 96/06/19 20:23:25

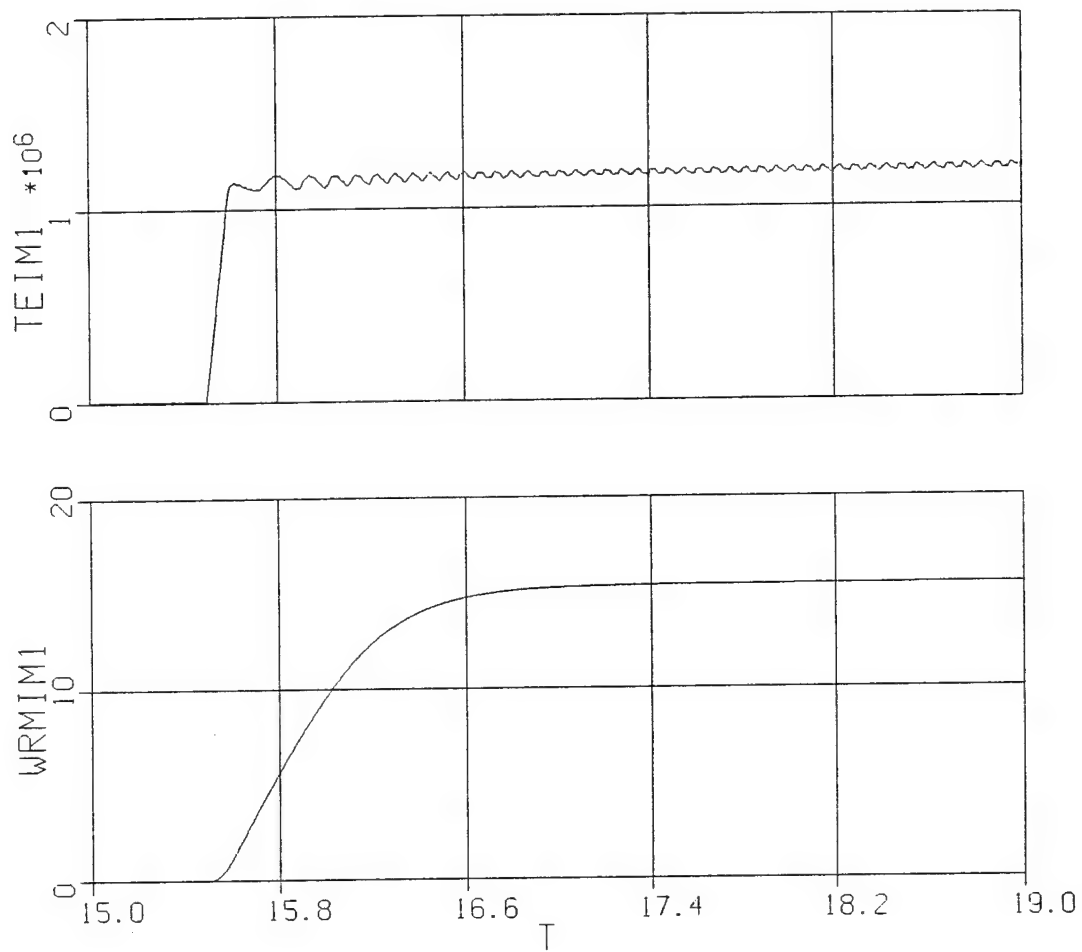


6 96/06/19 20:23:25

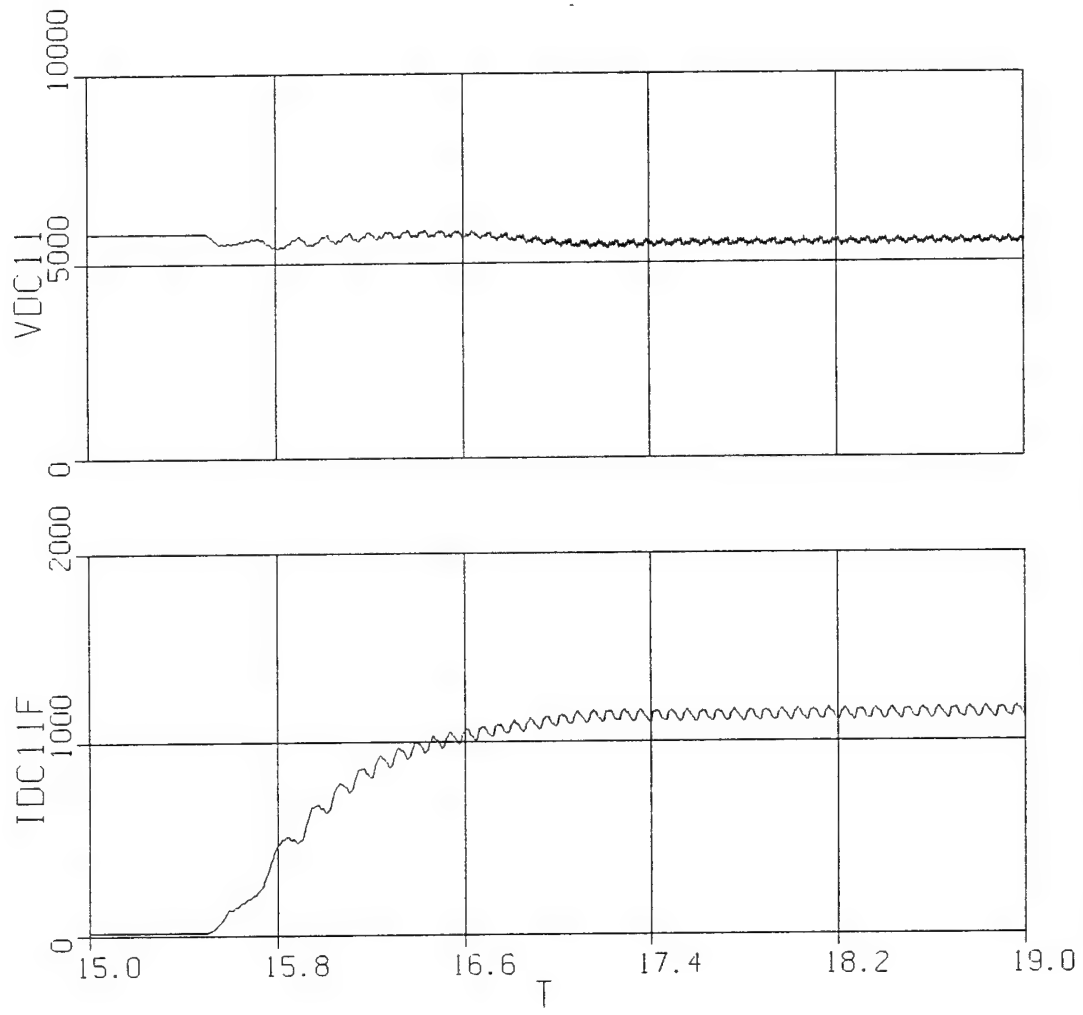




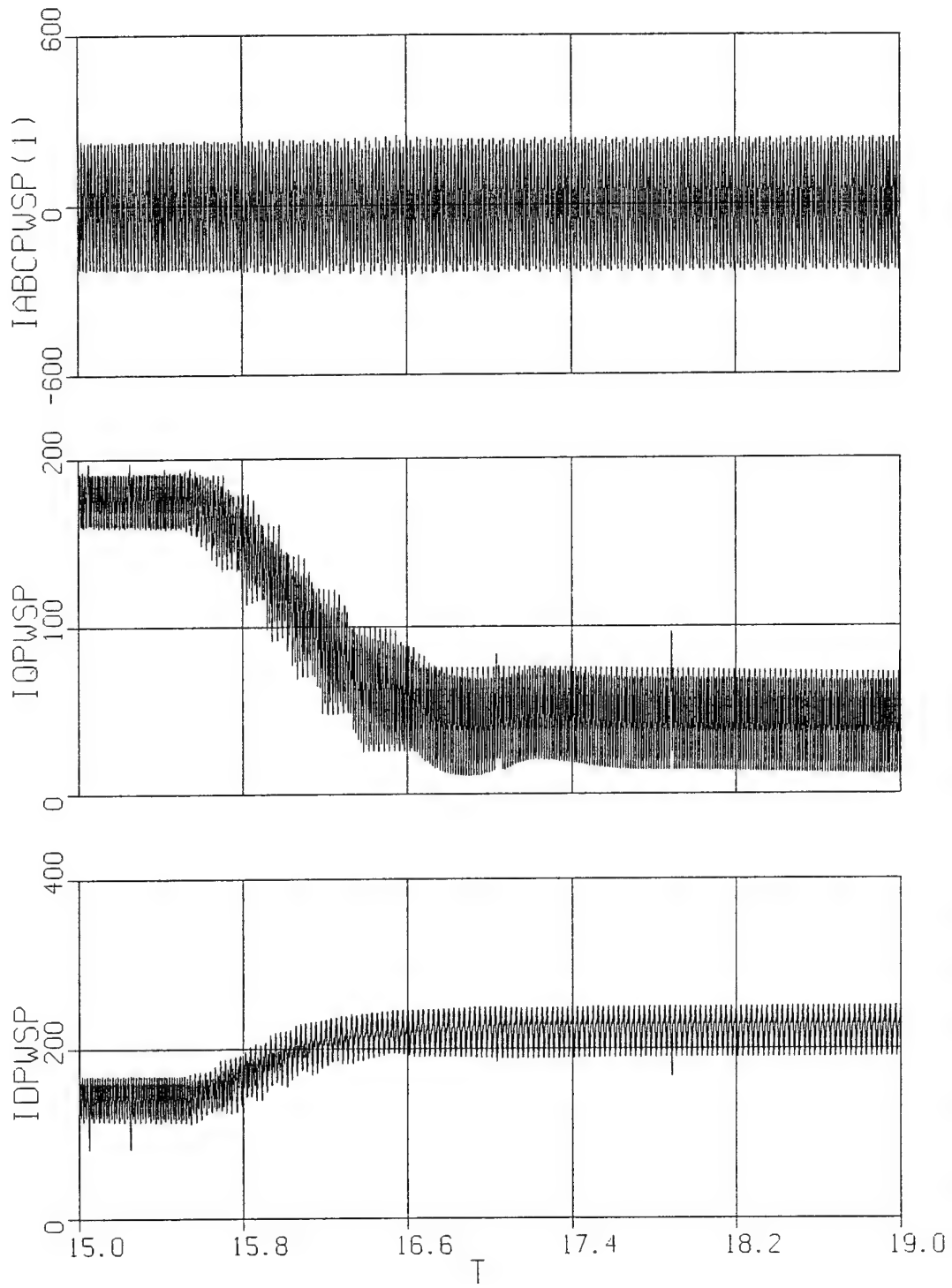
8 96/06/19 20:23:25



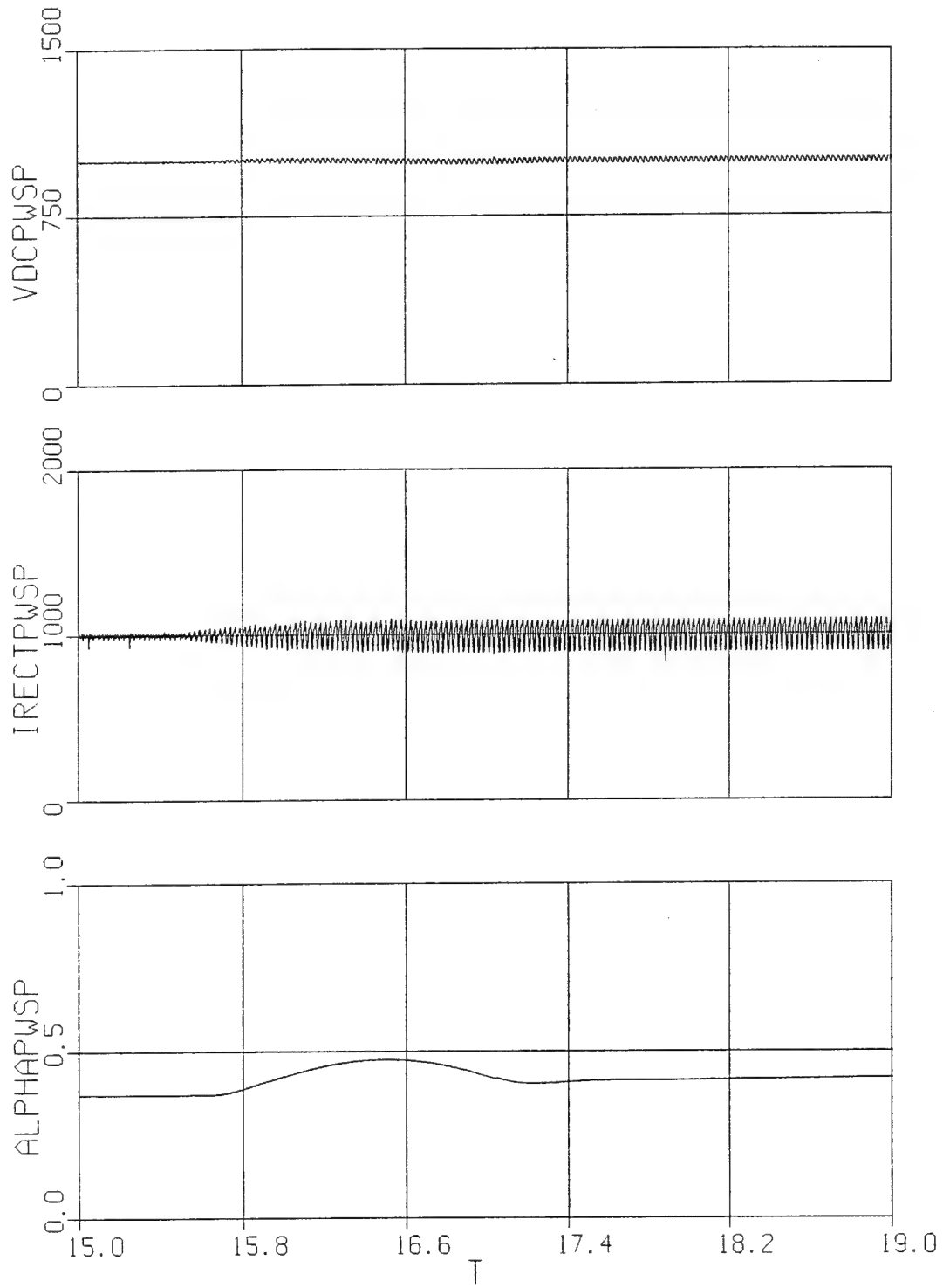
9 96/06/19 20:23:25



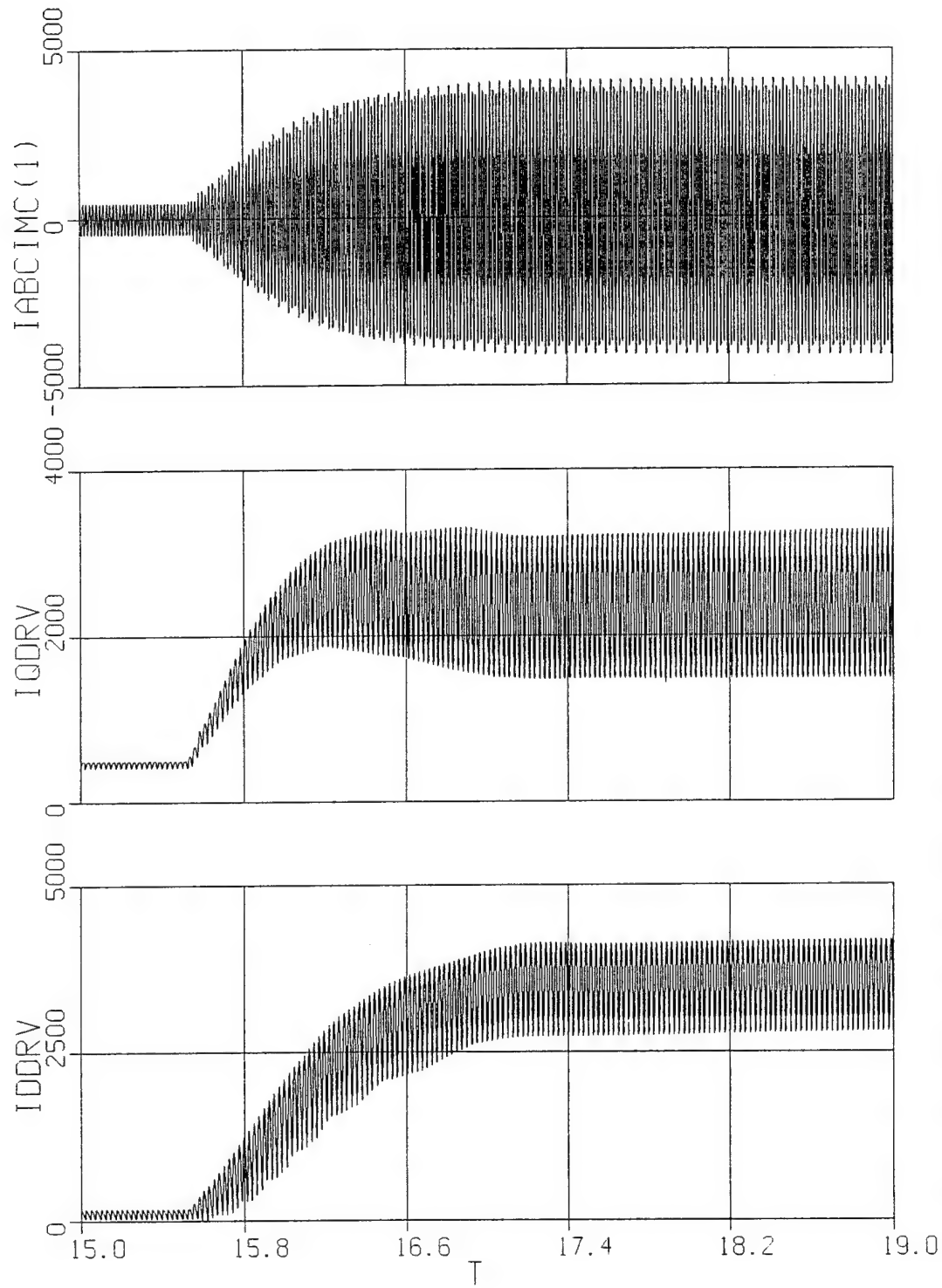
12 96/06/19 20:23:25



15 96/06/19 20:23:25



17 96/06/19 20:23:25

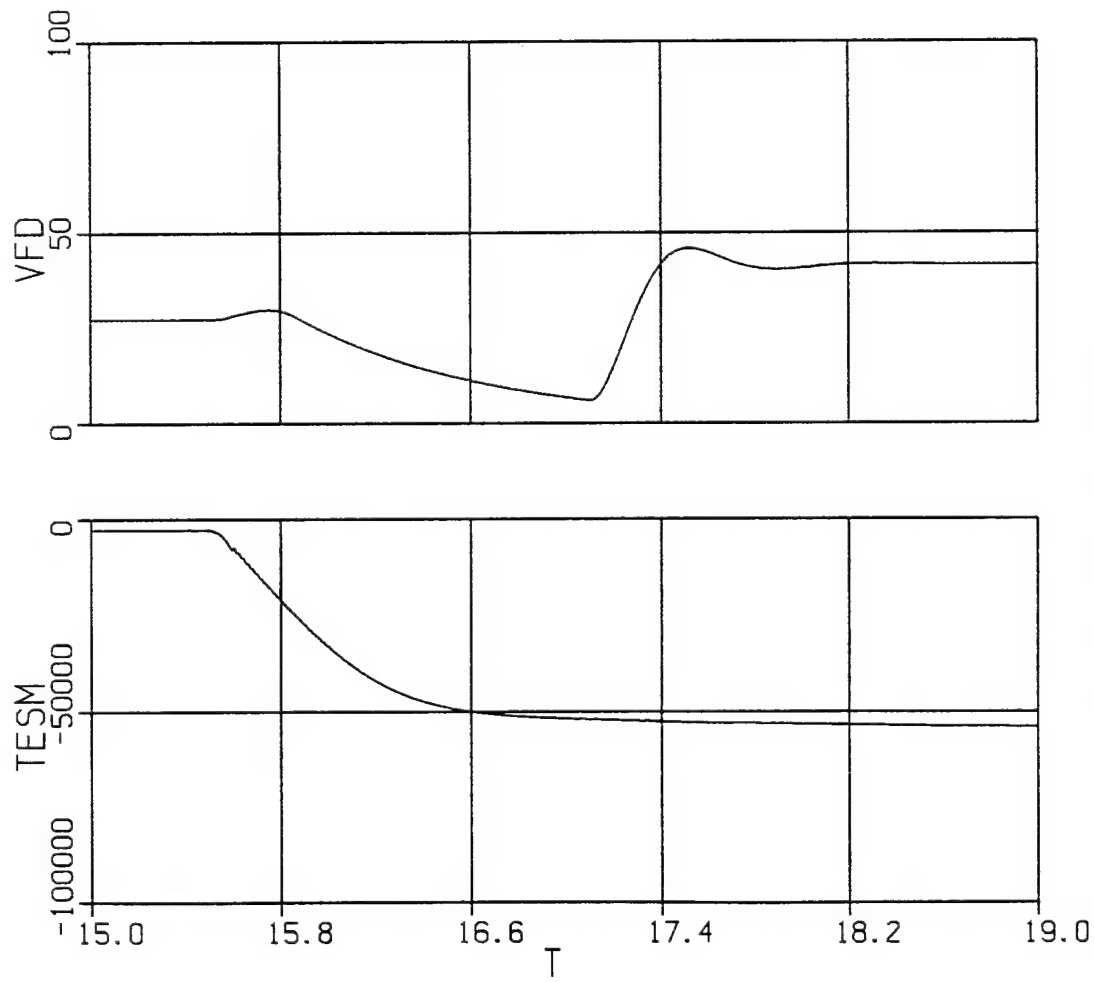


18 96/06/19 20:23:25

**Study 1b**

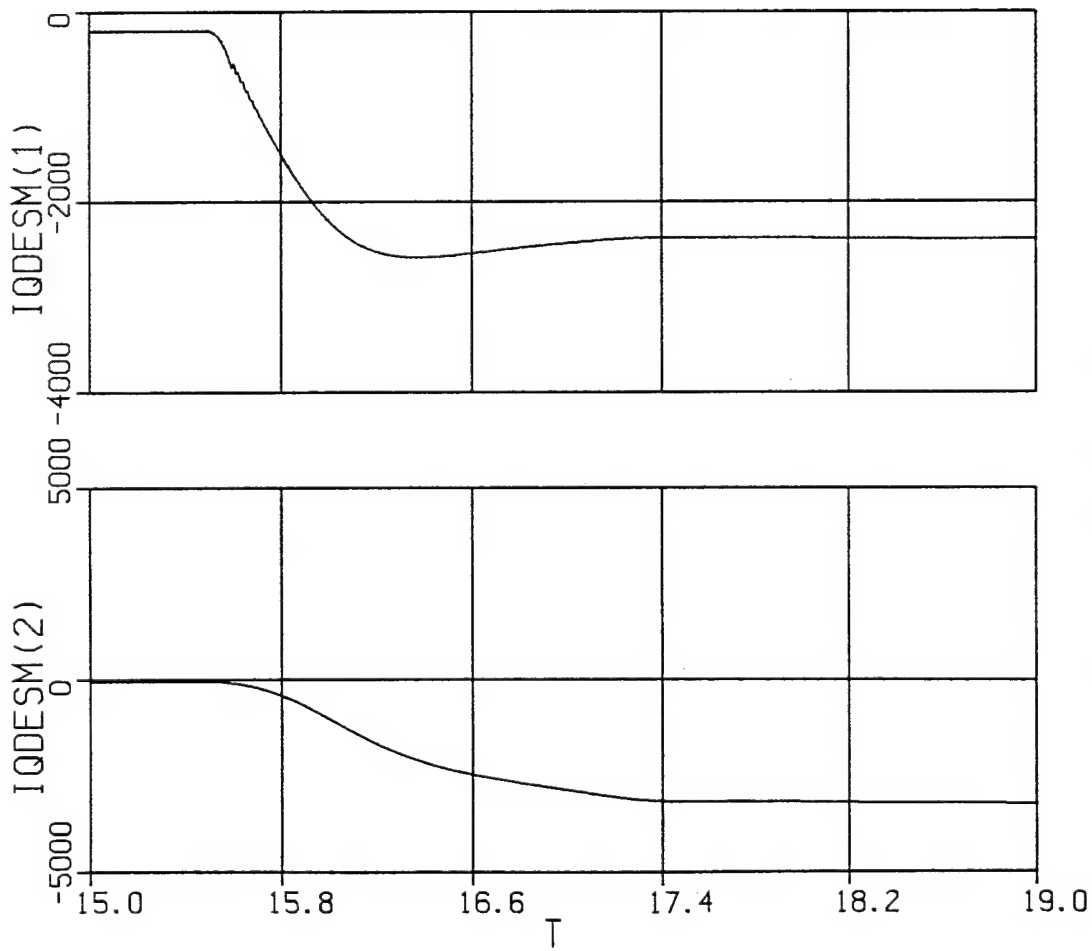
## Variable Description - Nonlinear Reduced-Order Model Simulation

<u>ACSL Name</u>	<u>Description</u>
alphaspwsp	power supply rectifier phase delay (rad)
idcl1	inverter current into first set of five H-bridges (A)
iddepwsp(2)	d-axis current into pulse power device (A)
iqdeimc(1)	q-axis current into induction motor power converter (A)
iqdeimc(2)	d-axis current into induction motor power converter (A)
iqdepwsp(1)	q-axis current into pulse power device (A)
iqdepwsp(1)	q-axis current into power supply (A)
iqdepwsp(2)	d-axis current into power supply (A)
iqdesm(1)	q-axis synchronous machine current (positive in) (A)
iqdesm(2)	d-axis synchronous machine current (positive in) (A)
irectpwsp	dc link current in power supply (positive out of rectifier) (A)
irppw	inductor current in pulse power device (A)
teiml	induction motor electromagnetic torque (Nm)
tesm	synchronous machine torque (positive for motor operation) (Nm)
vcapppw	capacitor voltage of pulse power device (A)
vdc11	dc voltage at input of first 5 H-bridges (V)
vdcpwsp	power supply dc output voltage (V)
vfd	synchronous machine field voltage (unreferred) (V)
vqde(1)	q-axis bus voltage (V)
vqde(2)	d-axis bus voltage (V)
wrmiml	induction motor speed - mechanical (rad/s)

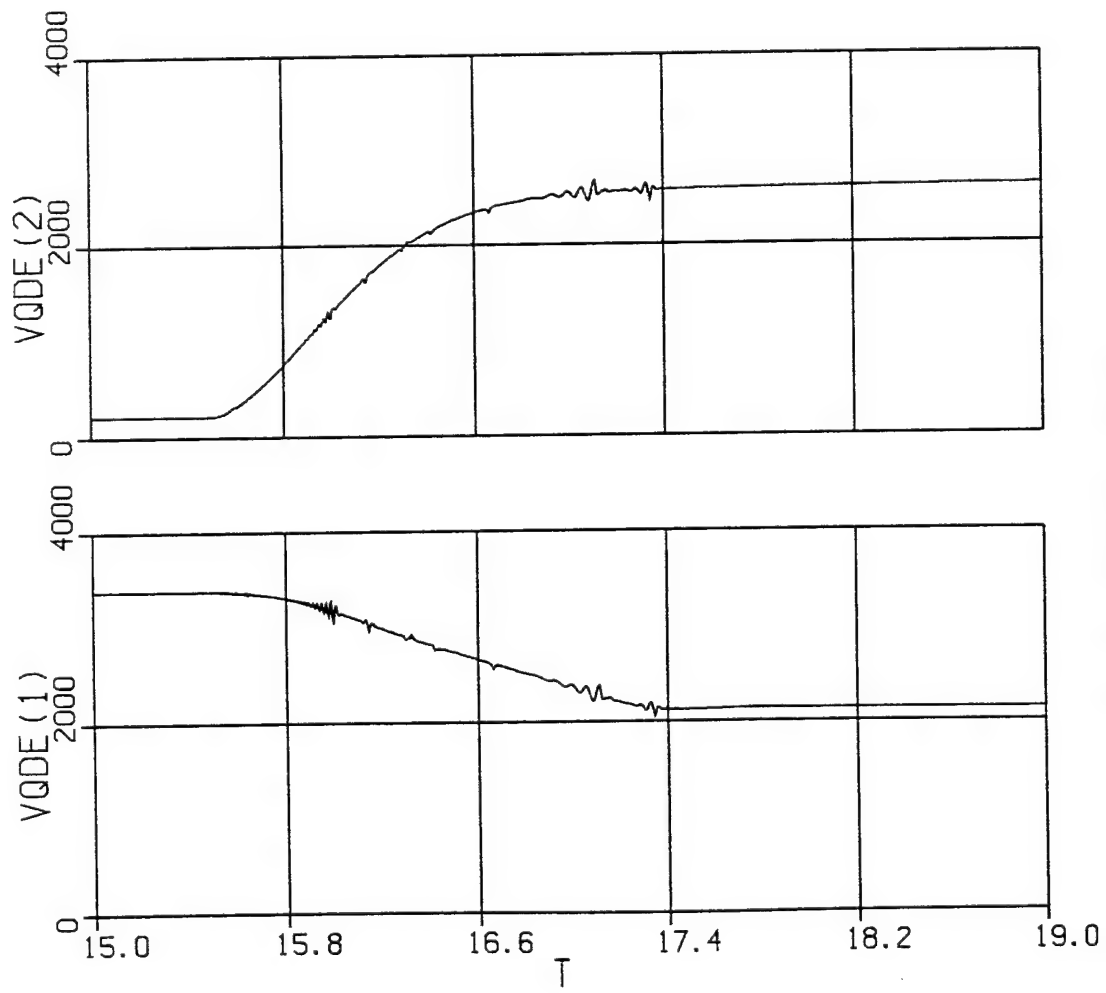


2 Jun 26 11:37:58 1996

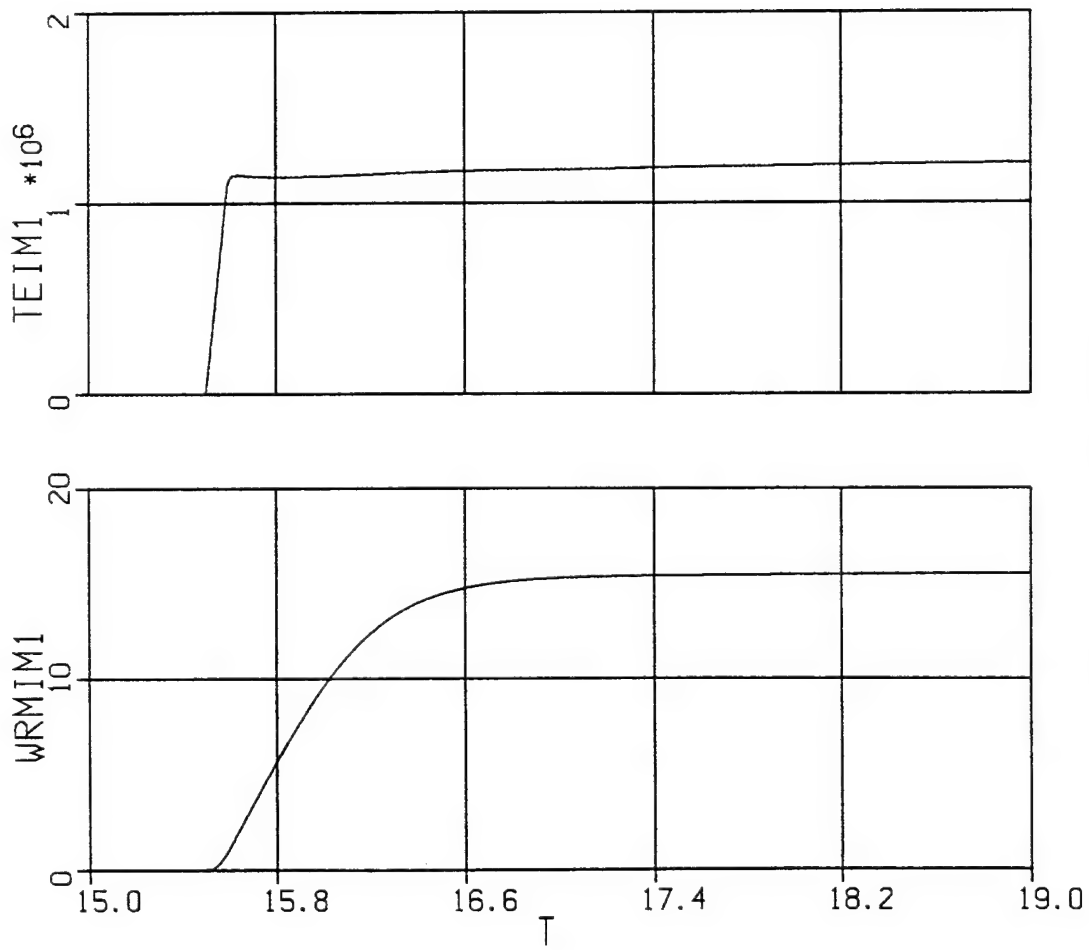




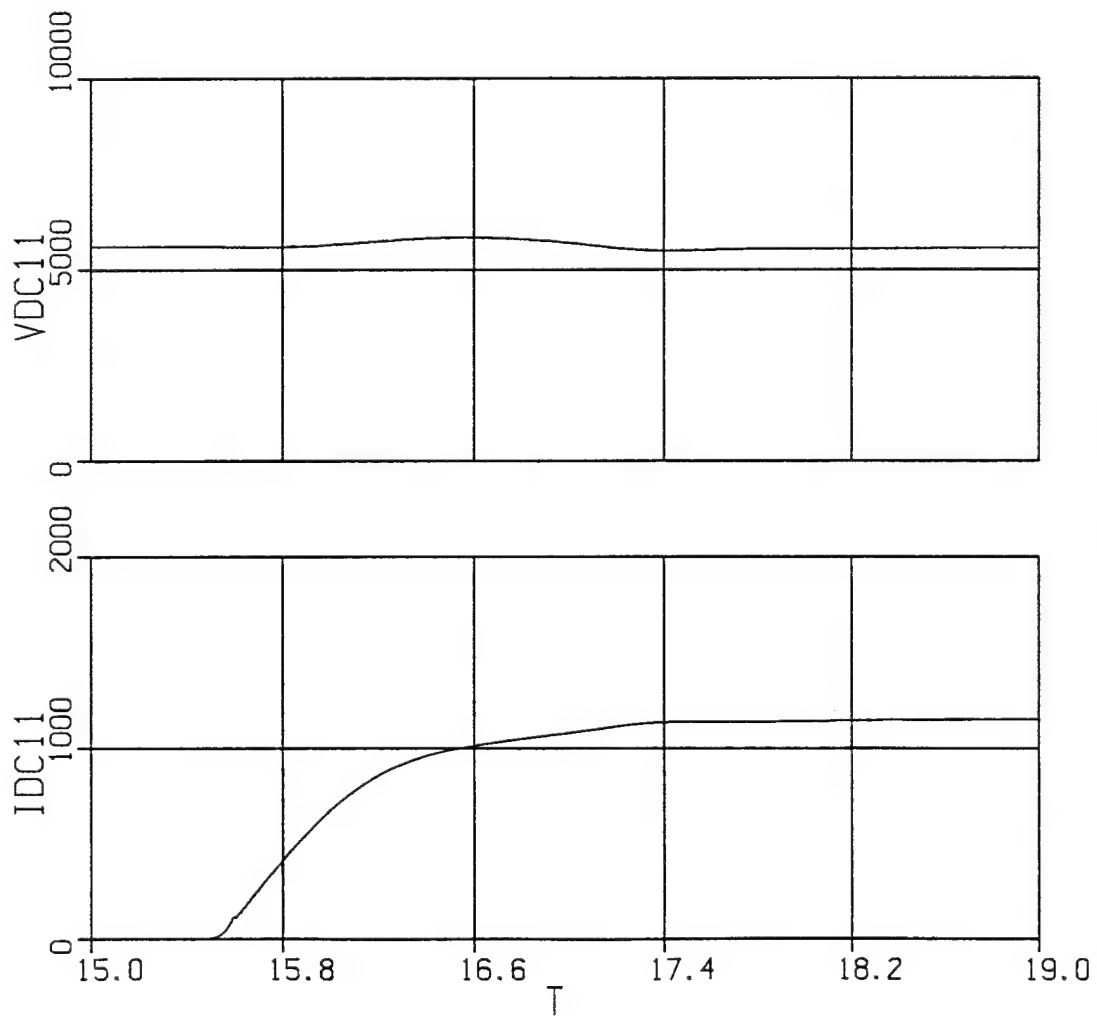
3 Jun 26 11:37:58 1996



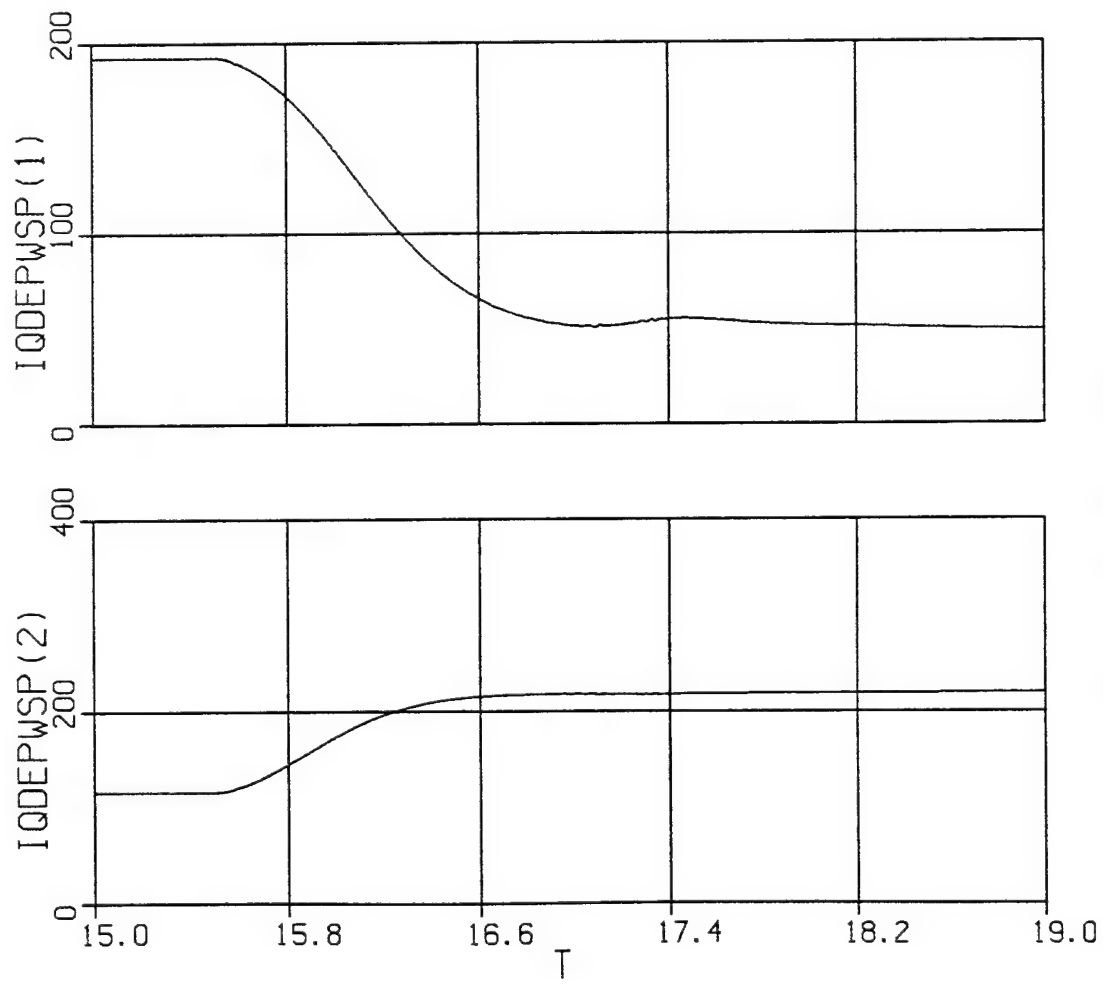
4 Jun 26 11:37:58 1996



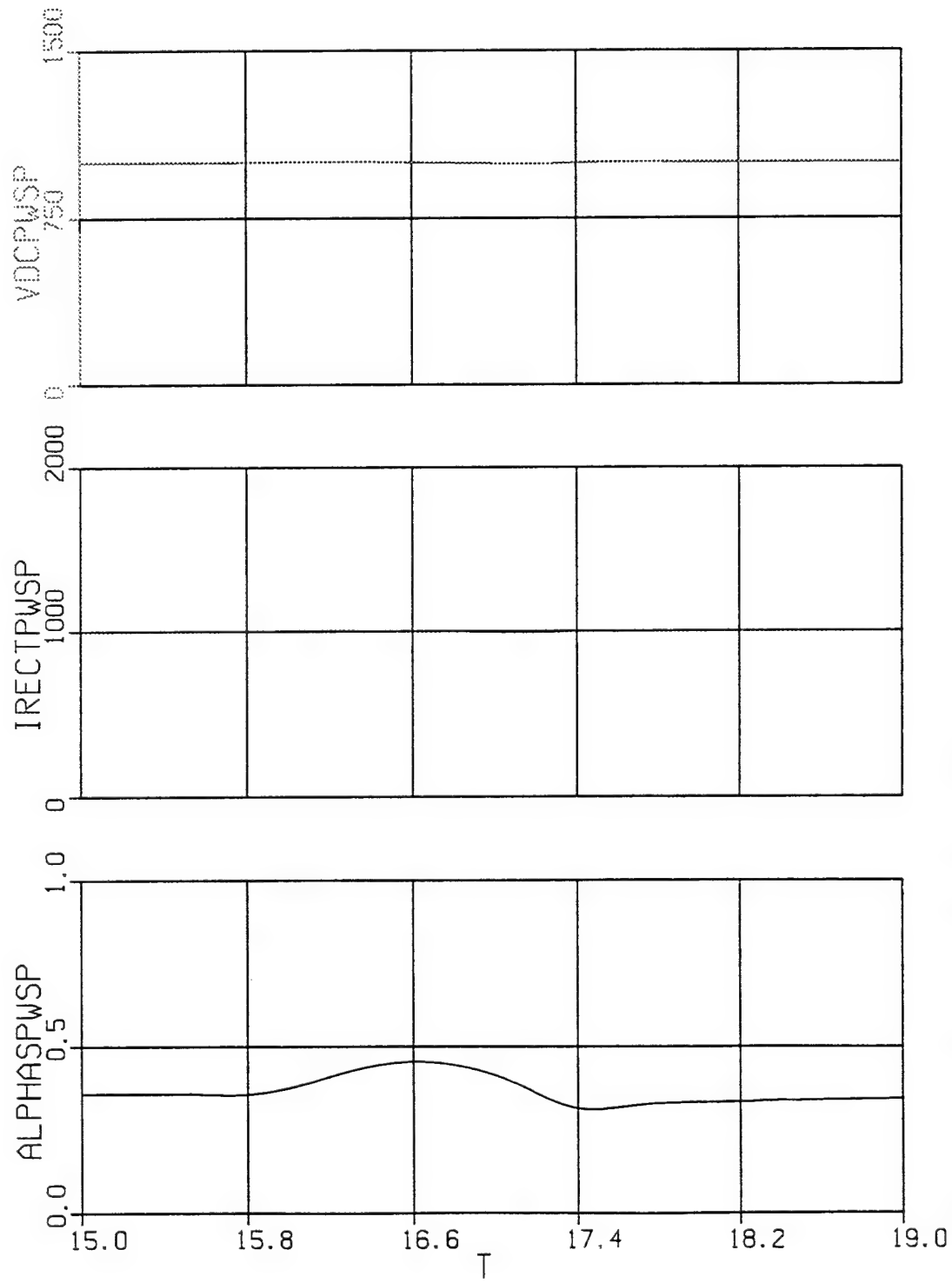
5 Jun 26 11:37:58 1996



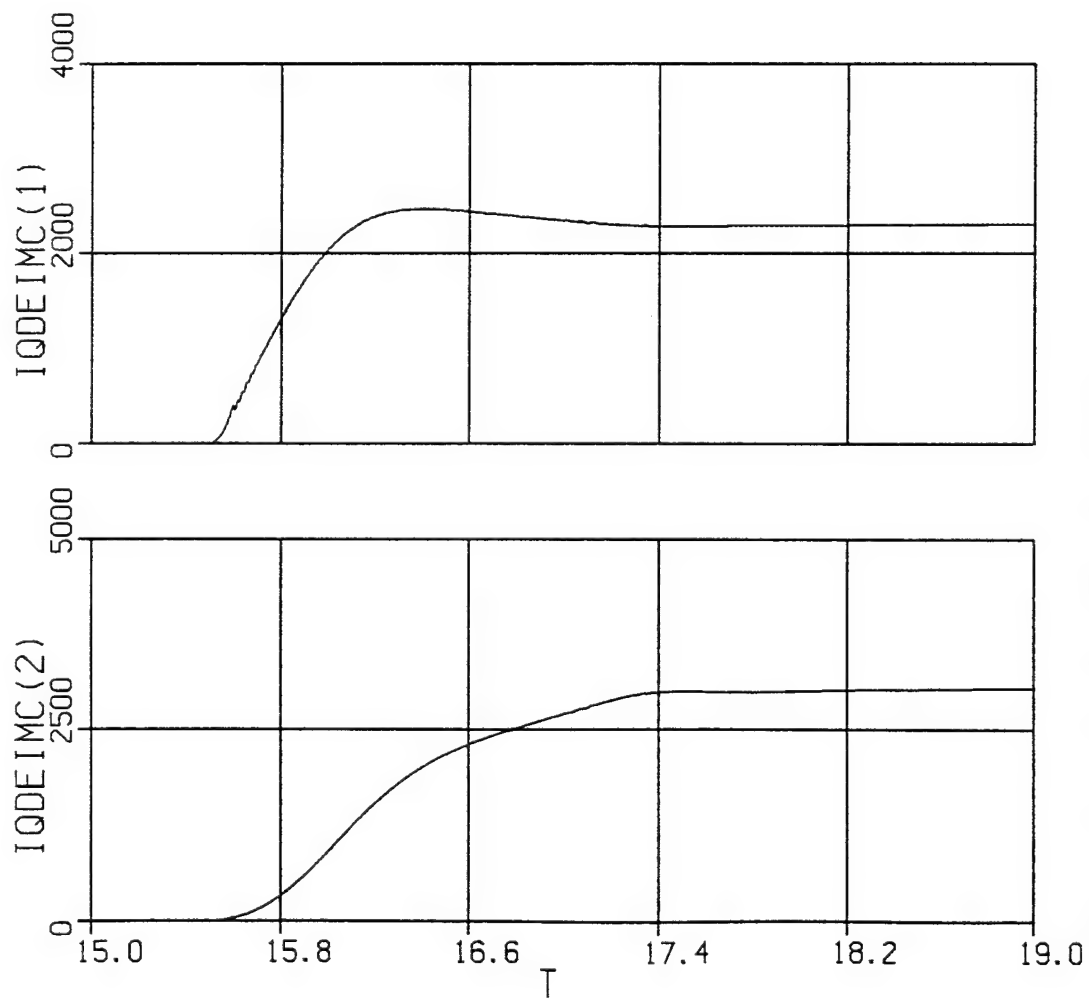
6 Jun 26 11:37:58 1996



7 Jun 26 11:37:58 1996



8 Jun 26 11:37:58 1996



9 Jun 26 11:37:58 1996

**Study 2**

In this study, the steady-state waveforms of several system variables are shown. The ship service power supply is operating at full load with the pulsed power system again out-of-service. The torque command for the propulsion induction motor is constant at full load ( $12 \text{ M N}\cdot\text{m}$ ).

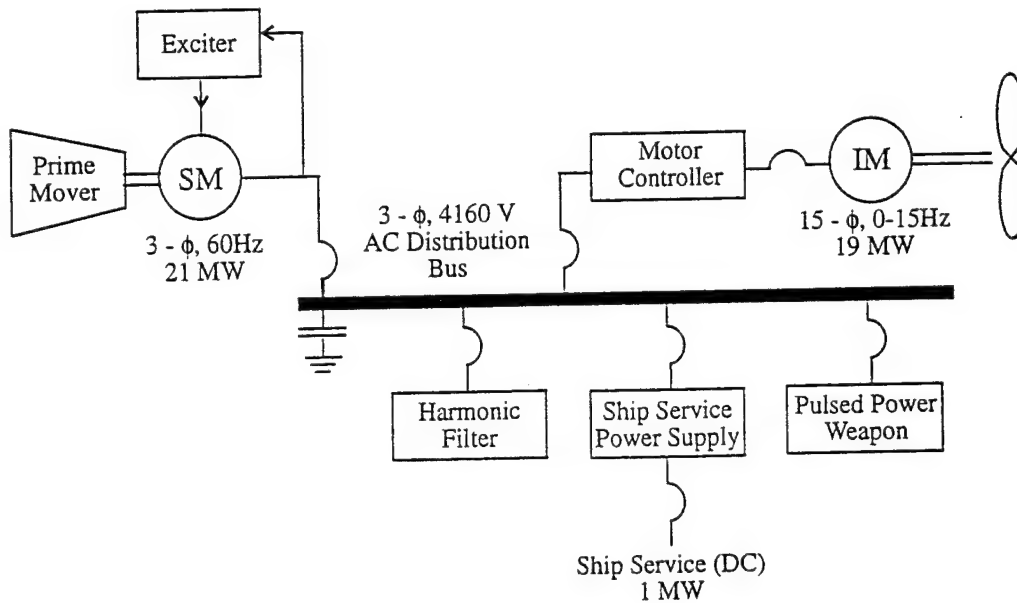
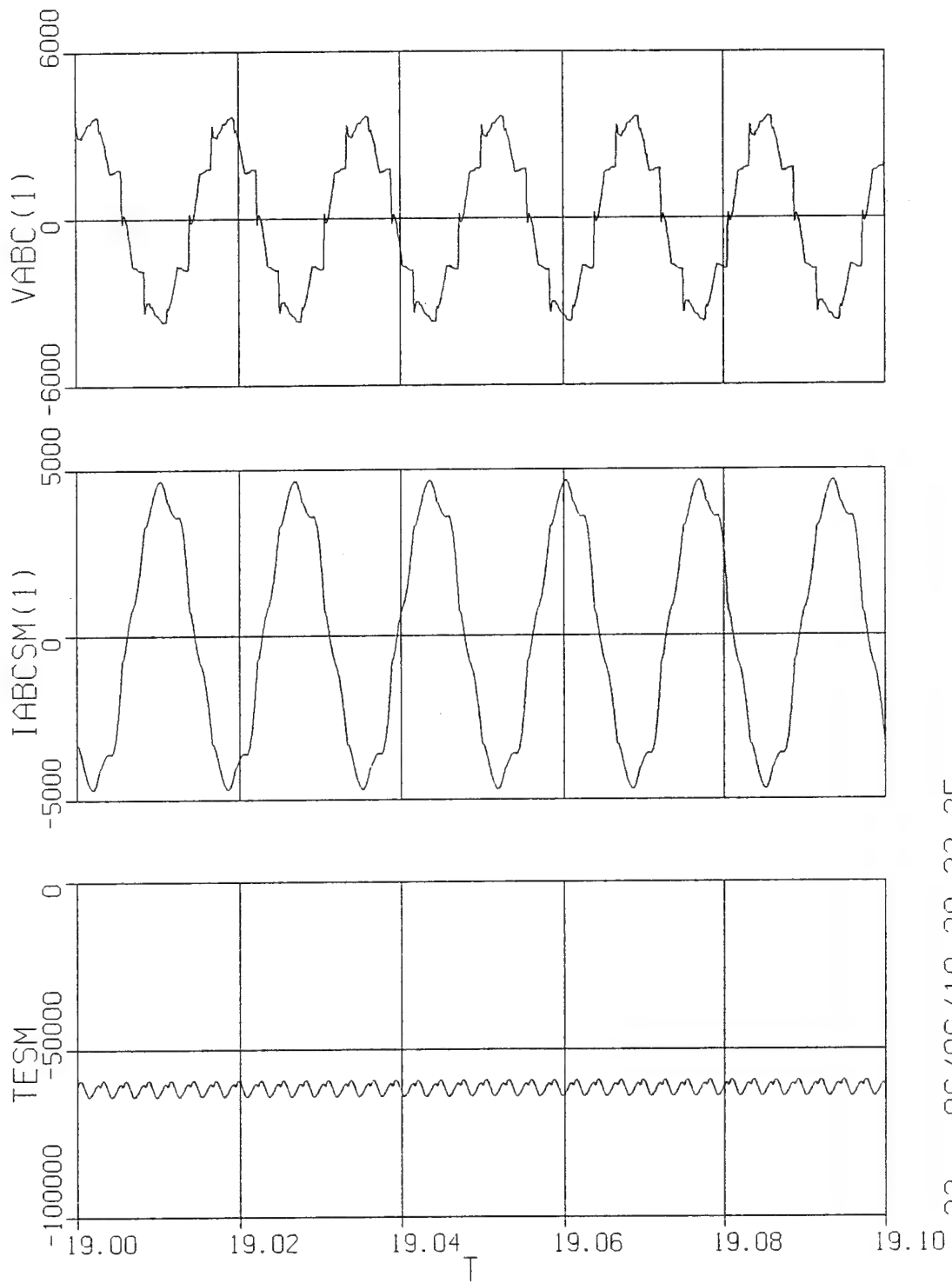


Figure 1. System studied.

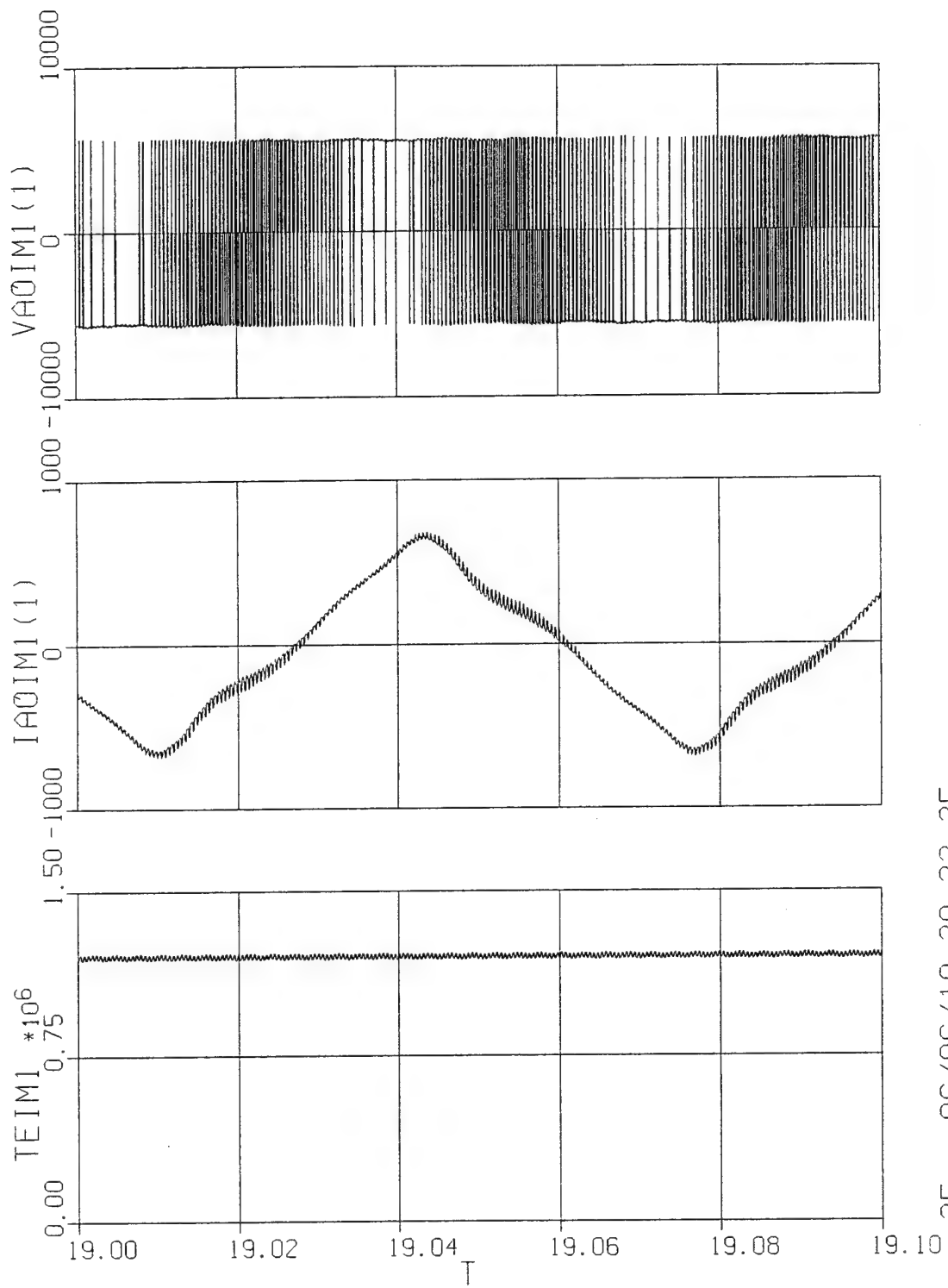


## Variable Description - Detailed Simulation

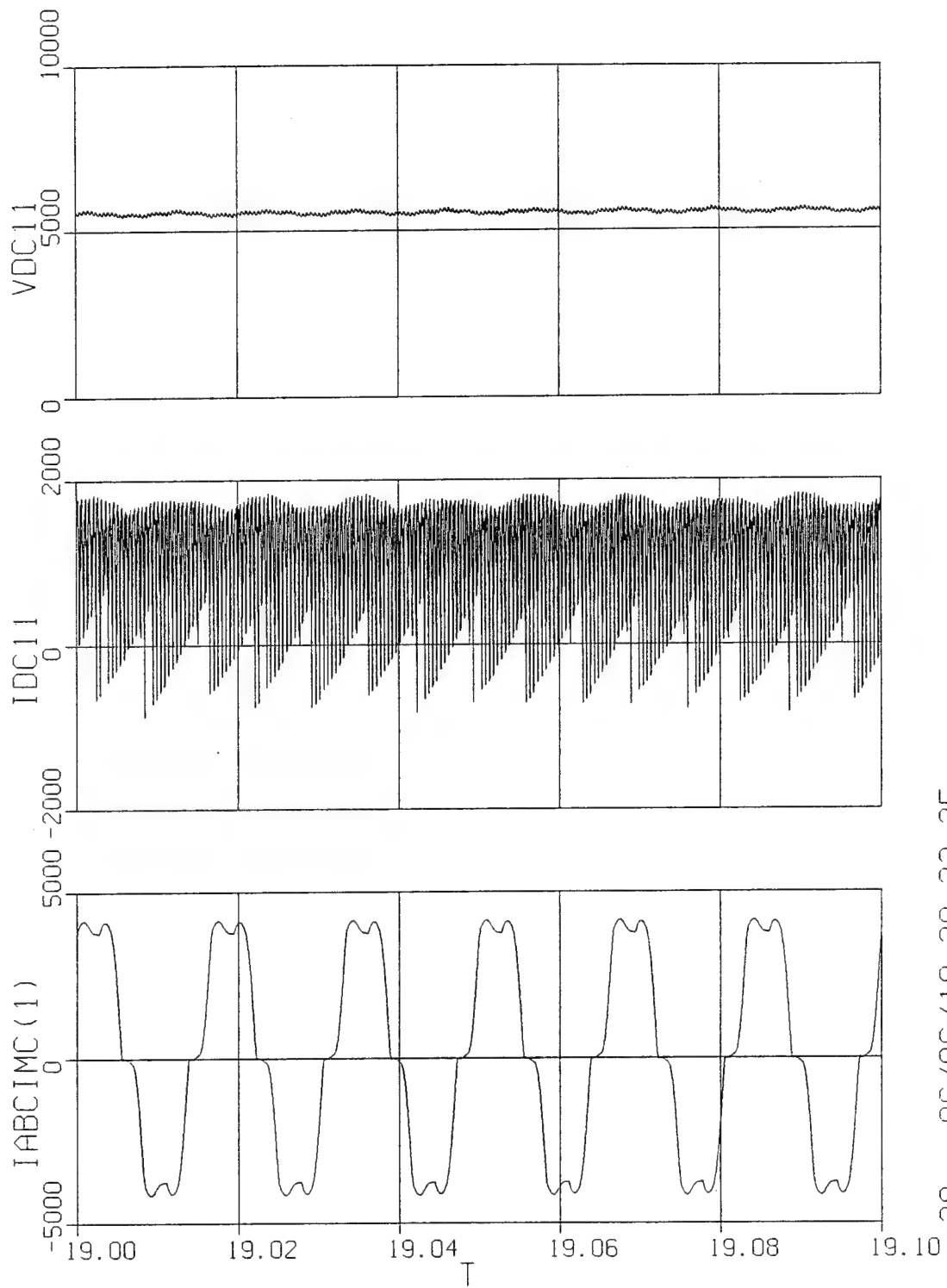
<u>ACSL Name</u>	<u>Description</u>
alphapwsp	power supply rectifier phase delay (rad)
iabcimc(1)	a-phase current into induction motor power converter (A)
iabcppw(1)	a-phase current into pulse power device (A)
iabcpwsp(1)	a-phase current into power supply (A)
iabcs(1)	a-phase synchronous machine current (positive in) (A)
iaom1(1)	a-phase induction motor current (A)
idcl1	dc current into first 5 H-bridge inverter (not filtered) (A)
idcl1f	low pass filtered inverter current into first set of five H-bridges (filtered so it could be compared to average value model) (A)
iddrv	d-axis current into induction motor power converter (A)
idppw	d-axis current into pulse power device (A)
idpwsp	d-axis current into power supply (A)
idsm	d-axis synchronous machine current (positive in) (A)
iqdrv	q-axis current into induction motor power converter (A)
iqppw	q-axis current into pulse power device (A)
iqpwsp	q-axis current into power supply (A)
iqsm	q-axis synchronous machine current (positive in) (A)
irectpwsp	dc link current in power supply (positive out of rectifier) (A)
irppw	inductor current in pulse power device (A)
teim1	induction motor electromagnetic torque (Nm)
tesm	synchronous machine torque (positive for motor operation) (Nm)
vabc(1)	a-phase 4160 V bus voltage (V)
vaoim1(1)	a-phase induction motor voltage (V)
vcapppw	capacitor voltage of pulse power device (A)
vd	d-axis bus voltage (V)
vdcl1	dc voltage at input of first 5 H-bridges (V)
vdcpwsp	power supply dc output voltage (V)
vfd	synchronous machine field voltage (unreferred) (V)
vq	q-axis bus voltage (V)
wrmim1	induction motor speed - mechanical (rad/s)



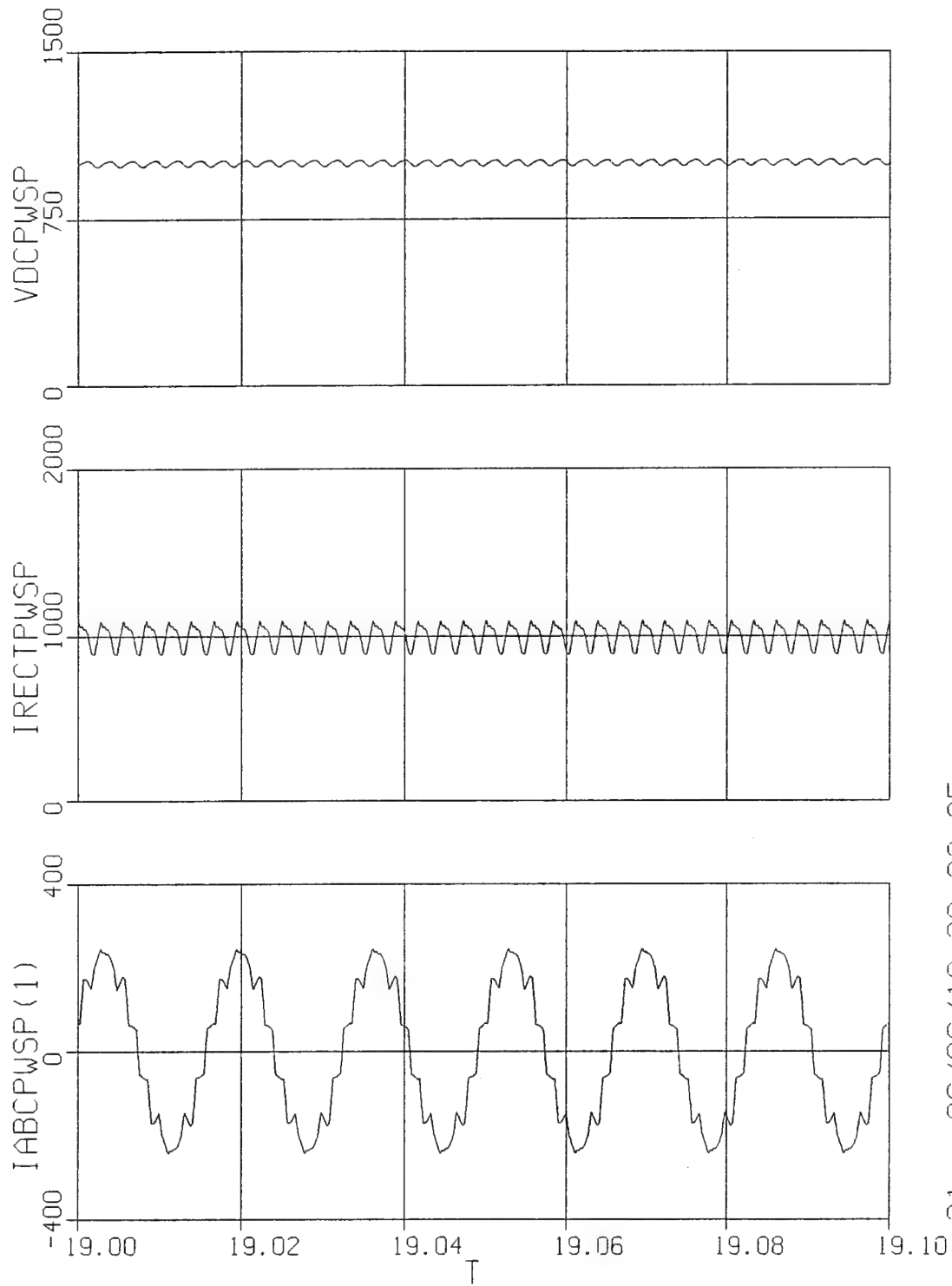
23 96/06/19 20:23:25



25 96/06/19 20:23:25



29 96/06/19 20:23:25



31 96/06/19 20:23:25

**Study 3**

Initially the system is operating in the steady state with the propulsion system (induction motor) and the ship service power supply operating at full load. At  $t = 20.5$  the pulsed power weapon is fired.

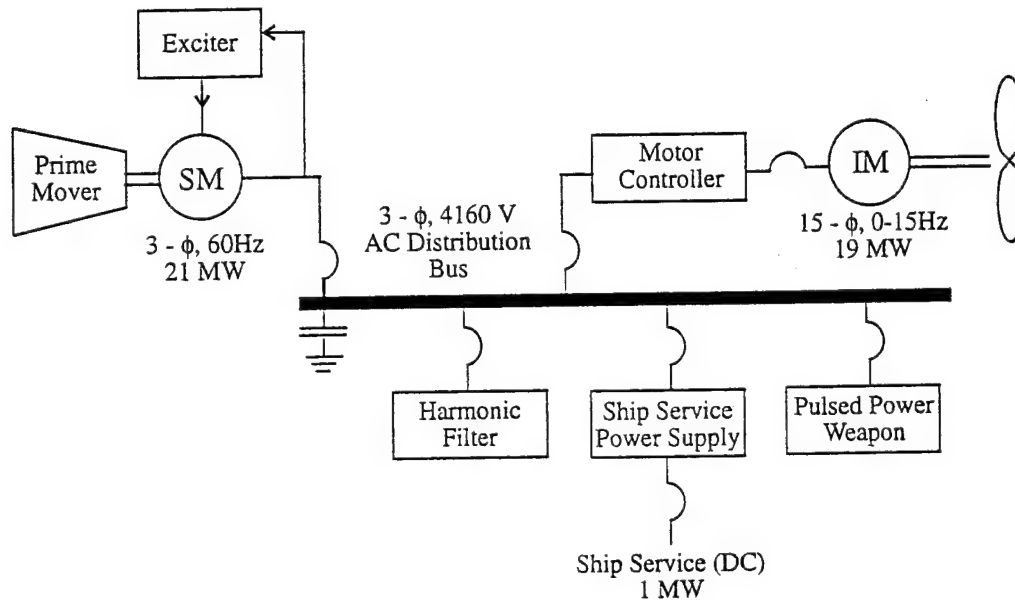
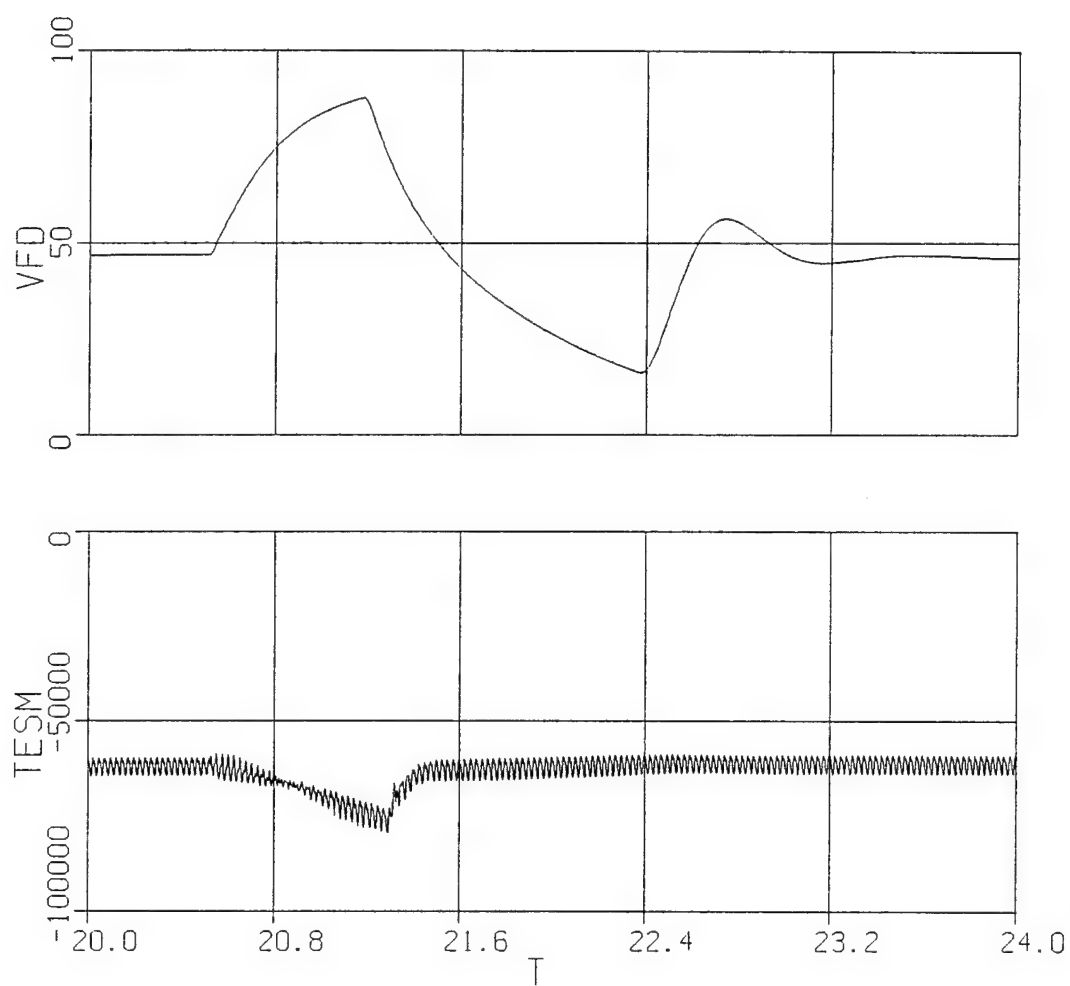


Figure 1. System studied.

**Study 3a**

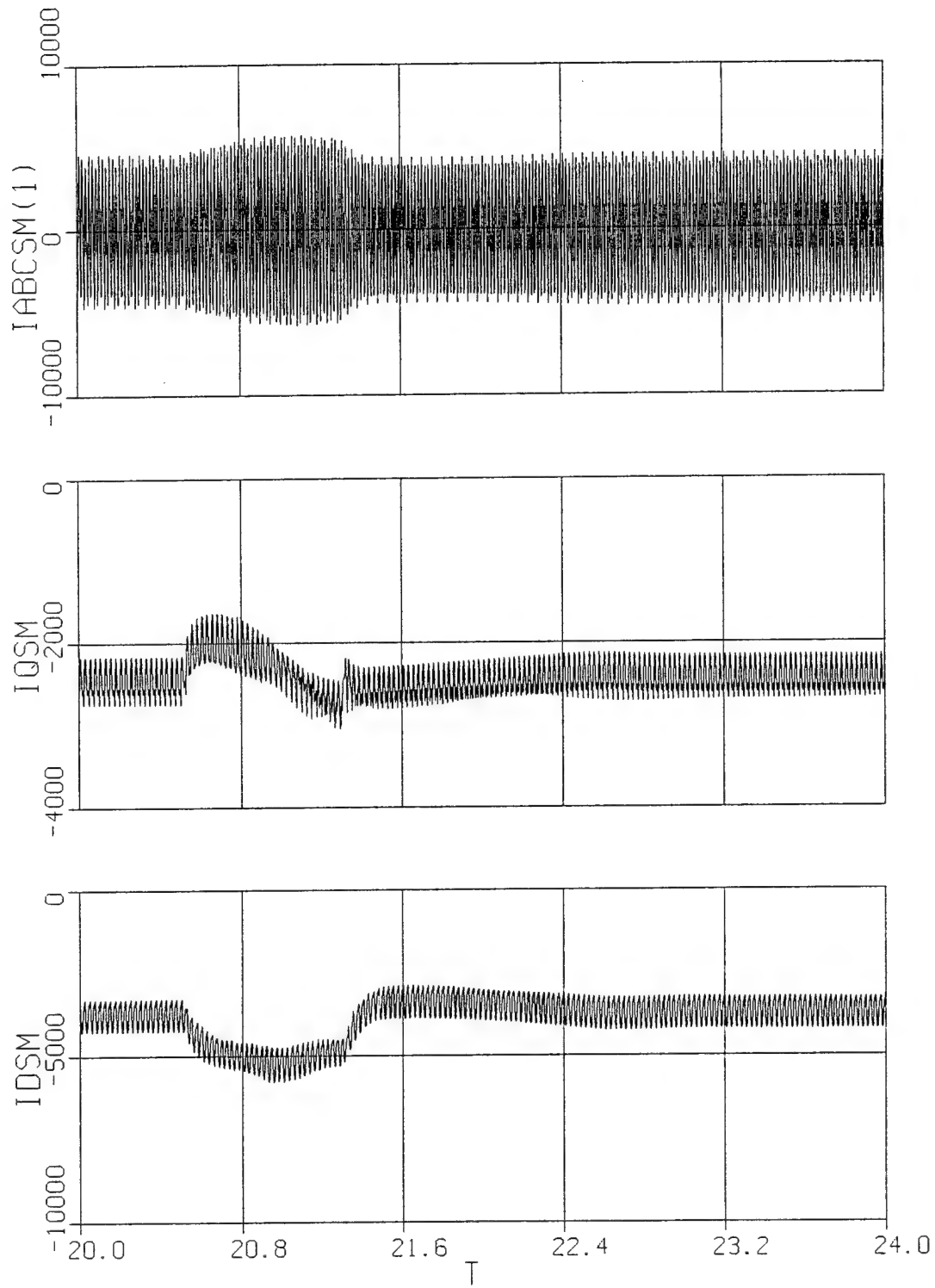
## Variable Description - Detailed Simulation

<u>ACSL Name</u>	<u>Description</u>
alphapwsp	power supply rectifier phase delay (rad)
iabcimc(1)	a-phase current into induction motor power converter (A)
iabcppw(1)	a-phase current into pulse power device (A)
iabcpwsp(1)	a-phase current into power supply (A)
iabscsm(1)	a-phase synchronous machine current (positive in) (A)
iaaiml(1)	a-phase induction motor current (A)
idcll	dc current into first 5 H-bridge inverter (not filtered) (A)
idcllf	low pass filtered inverter current into first set of five H-bridges (filtered so it could be compared to average value model) (A)
iddrv	d-axis current into induction motor power converter (A)
idppw	d-axis current into pulse power device (A)
idpwsp	d-axis current into power supply (A)
idsm	d-axis synchronous machine current (positive in) (A)
iqdrv	q-axis current into induction motor power converter (A)
iqppw	q-axis current into pulse power device (A)
iqpwsp	q-axis current into power supply (A)
iqsm	q-axis synchronous machine current (positive in) (A)
irectpwsp	dc link current in power supply (positive out of rectifier) (A)
irppw	inductor current in pulse power device (A)
teiml	induction motor electromagnetic torque (Nm)
tesm	synchronous machine torque (positive for motor operation) (Nm)
vabc(1)	a-phase 4160 V bus voltage (V)
vaaiml(1)	a-phase induction motor voltage (V)
vcapppw	capacitor voltage of pulse power device (A)
vd	d-axis bus voltage (V)
vdc1l	dc voltage at input of first 5 H-bridges (V)
vdcpwsp	power supply dc output voltage (V)
vfd	synchronous machine field voltage (unreferred) (V)
vq	q-axis bus voltage (V)
wrmiml	induction motor speed - mechanical (rad/s)

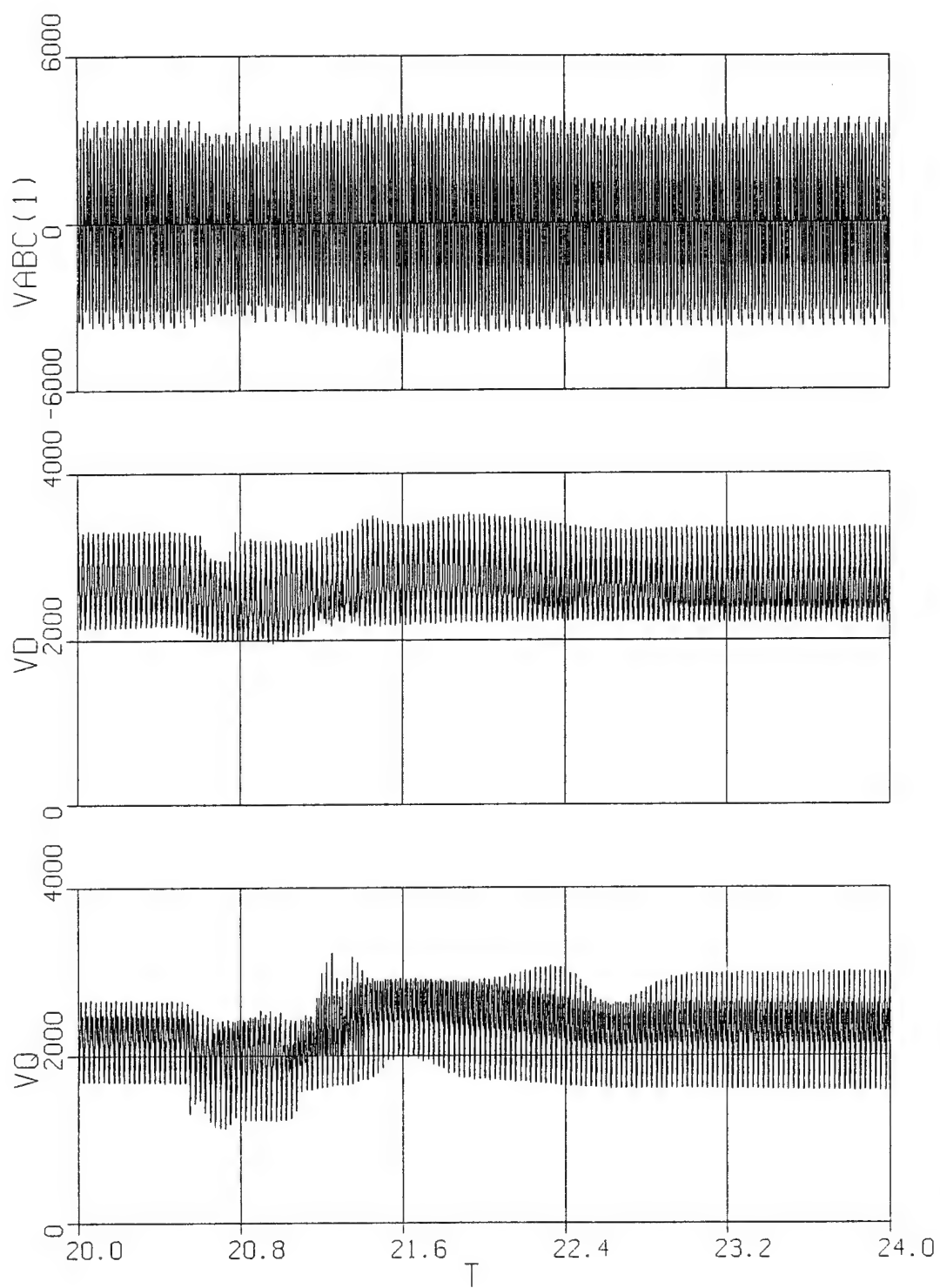


35 96/06/19 20:23:25

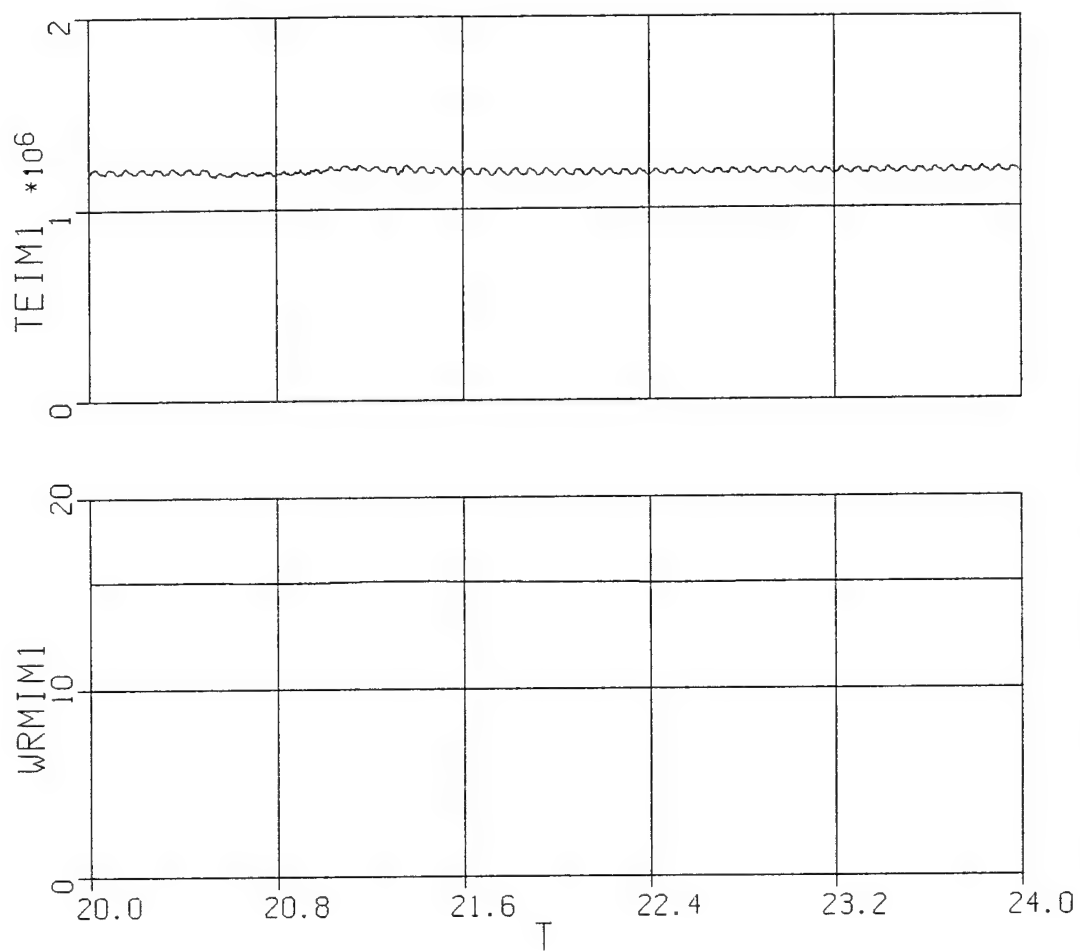




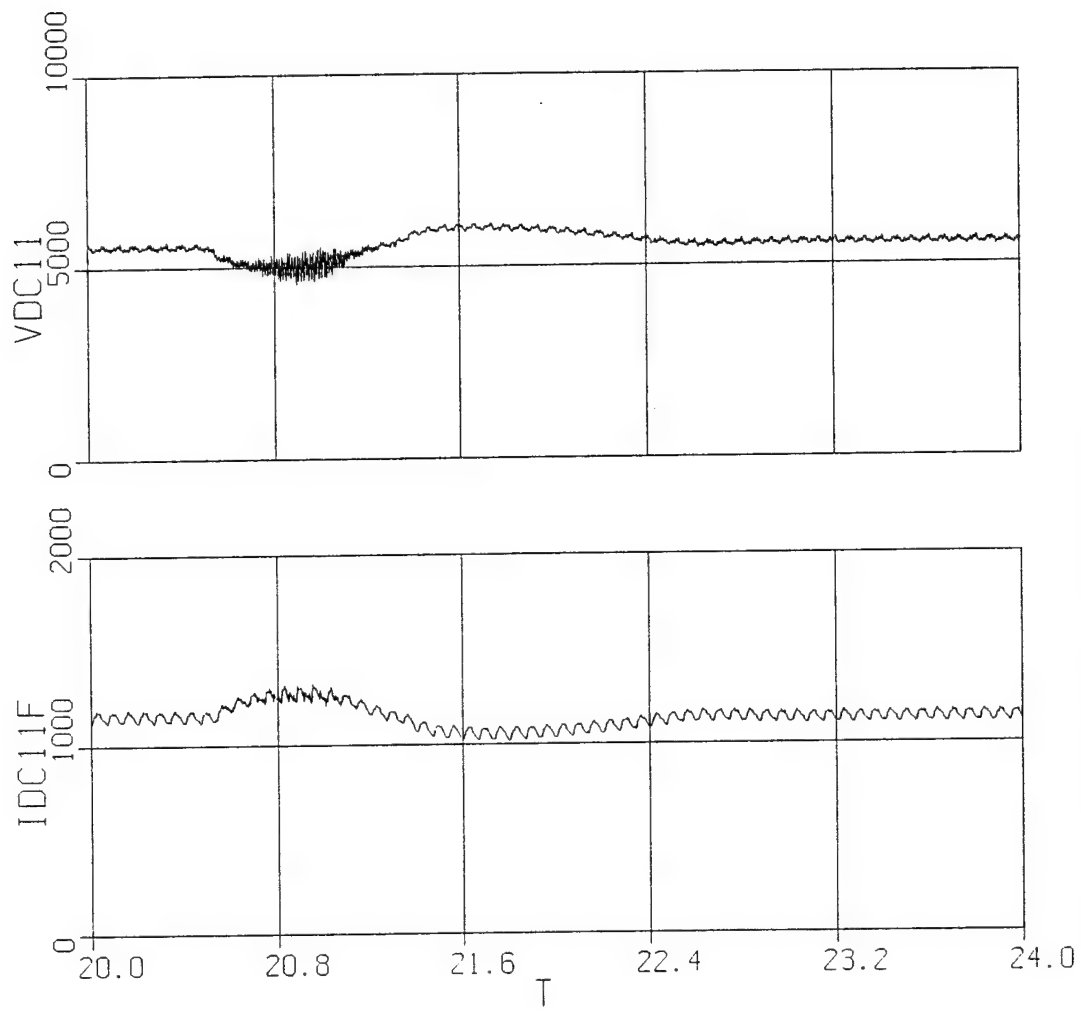
36 96/06/19 20:23:25



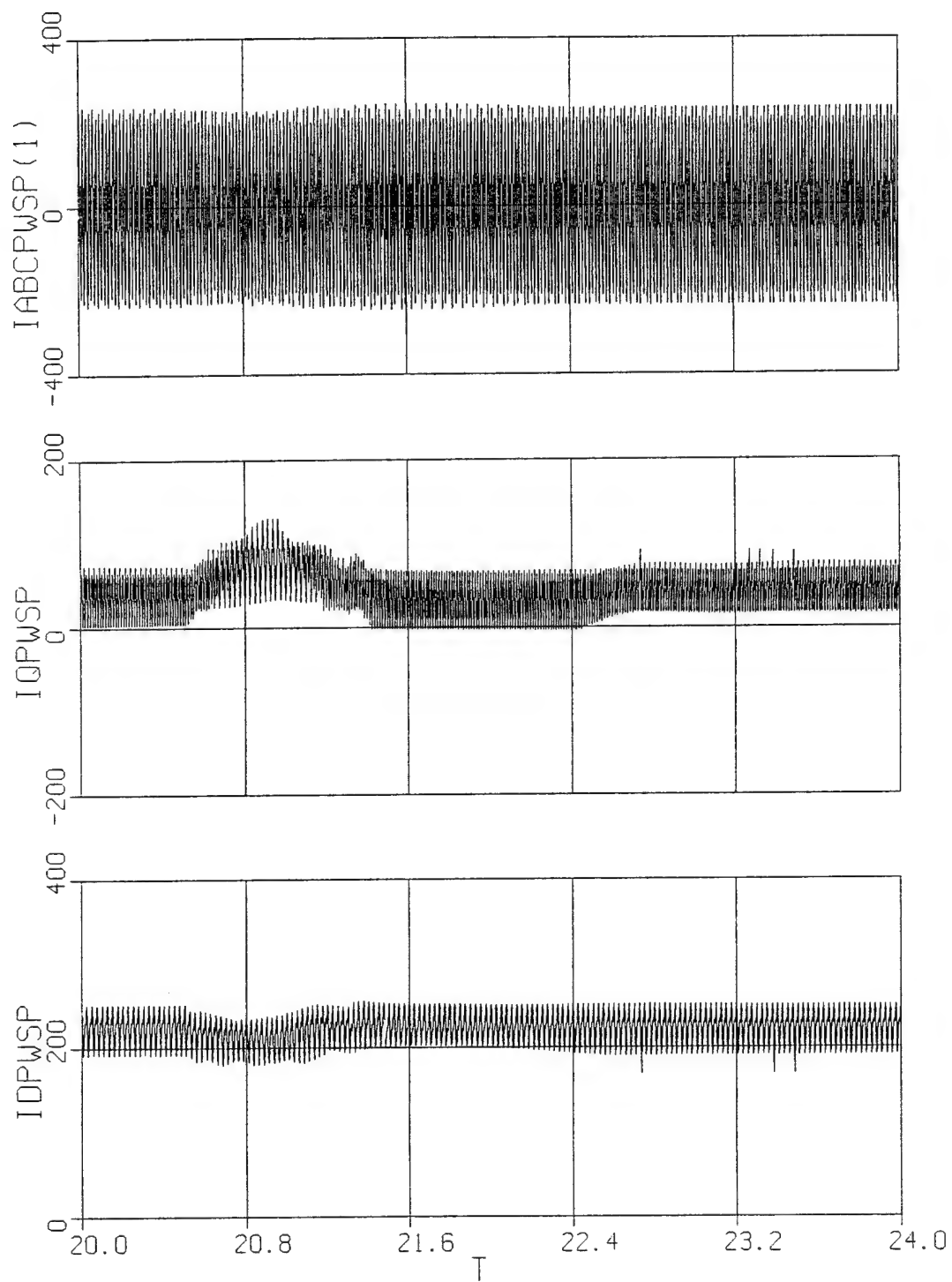
38 96/06/19 20:23:25



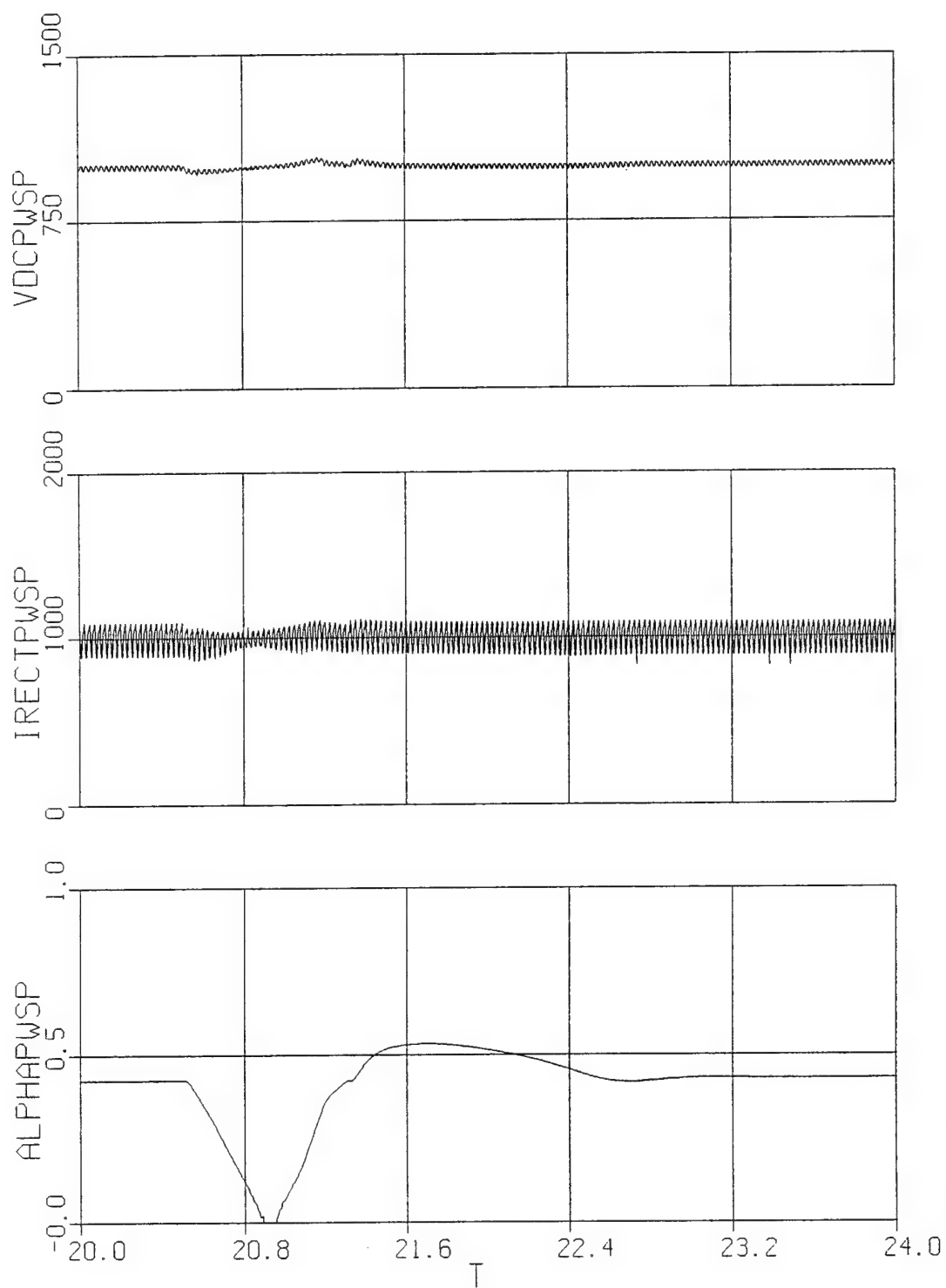
40 96/06/19 20:23:25



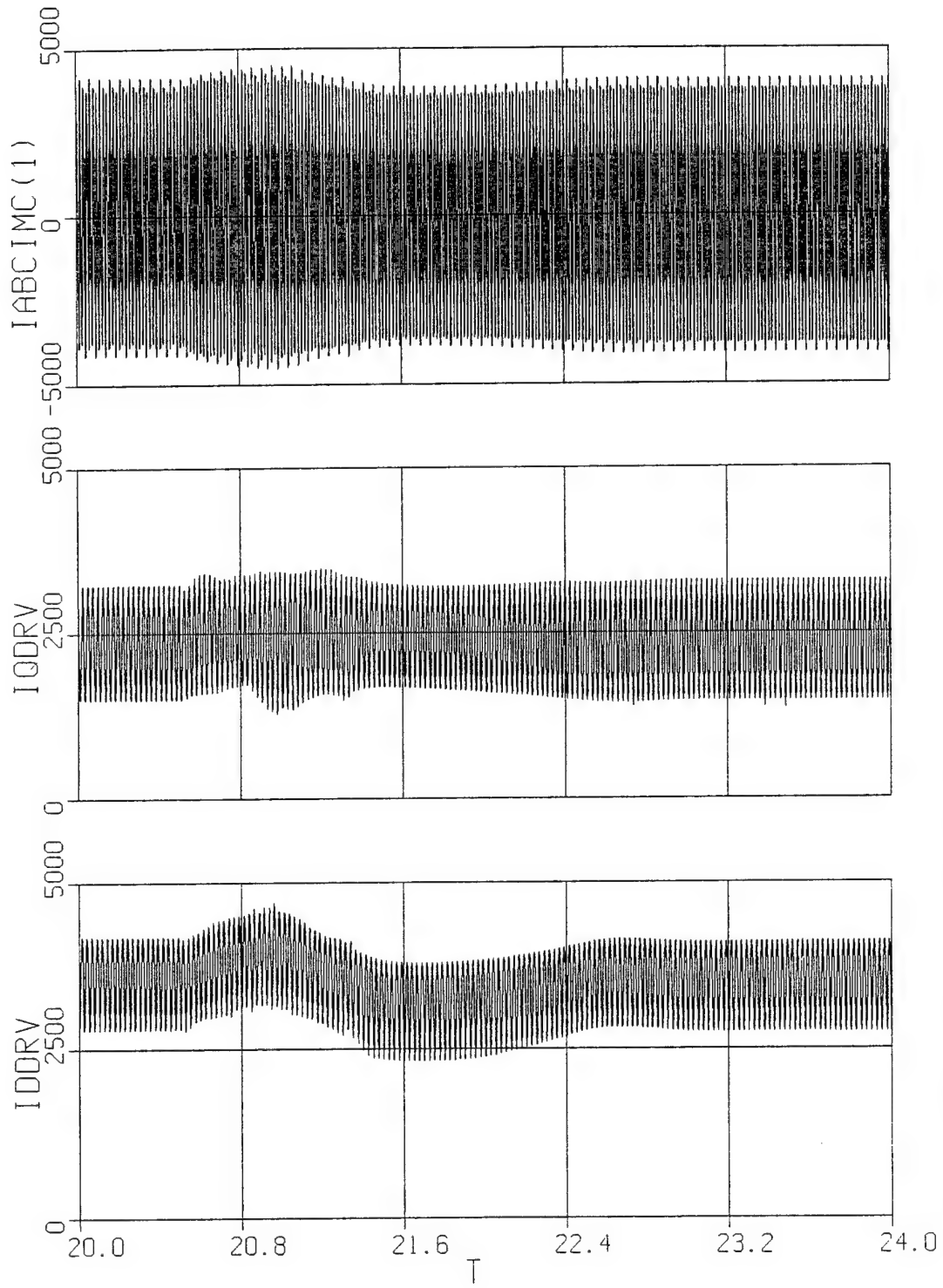
41 96/06/19 20:23:25



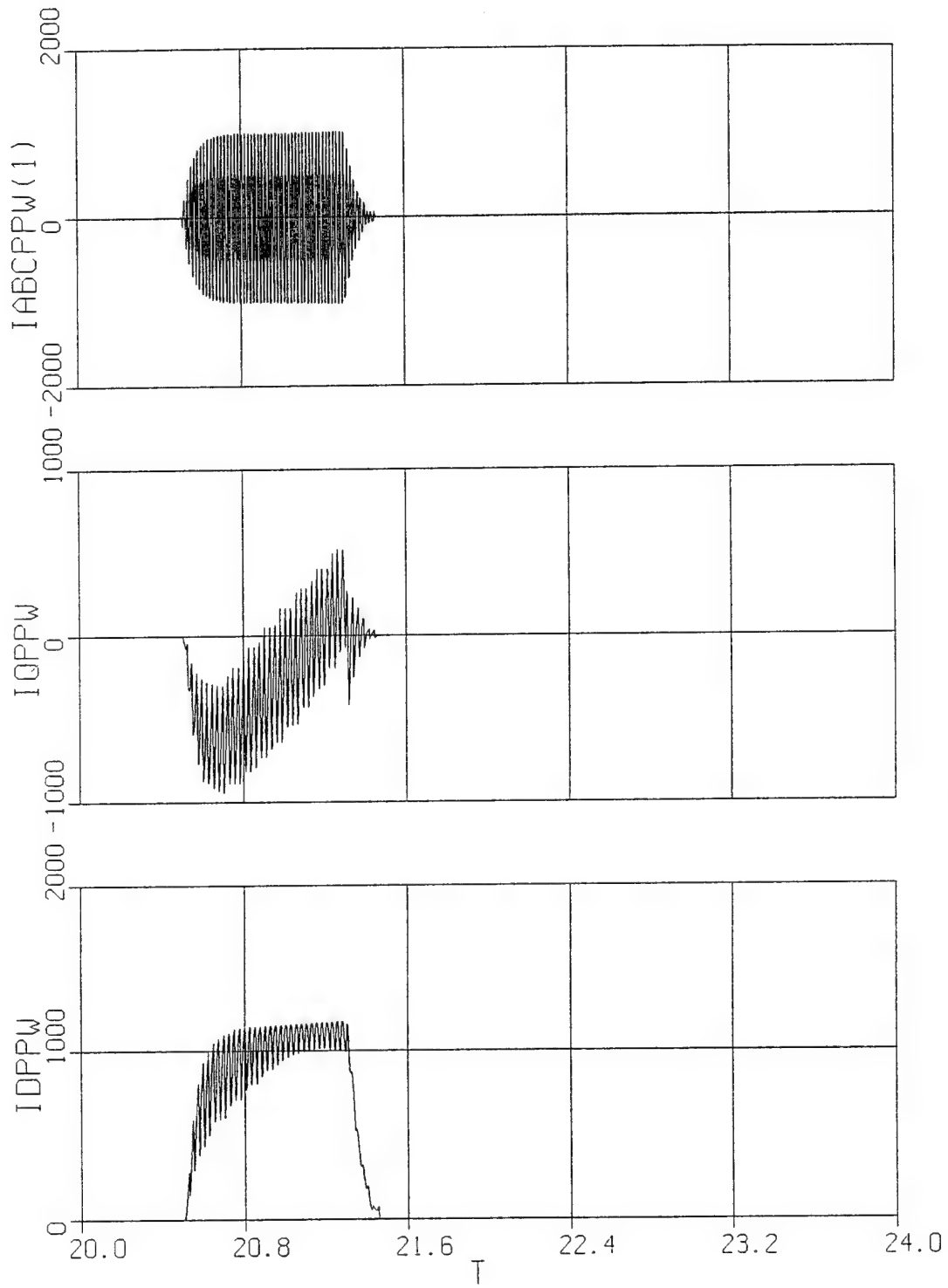
46 96/06/19 20:23:25



49 96/06/19 20:23:25

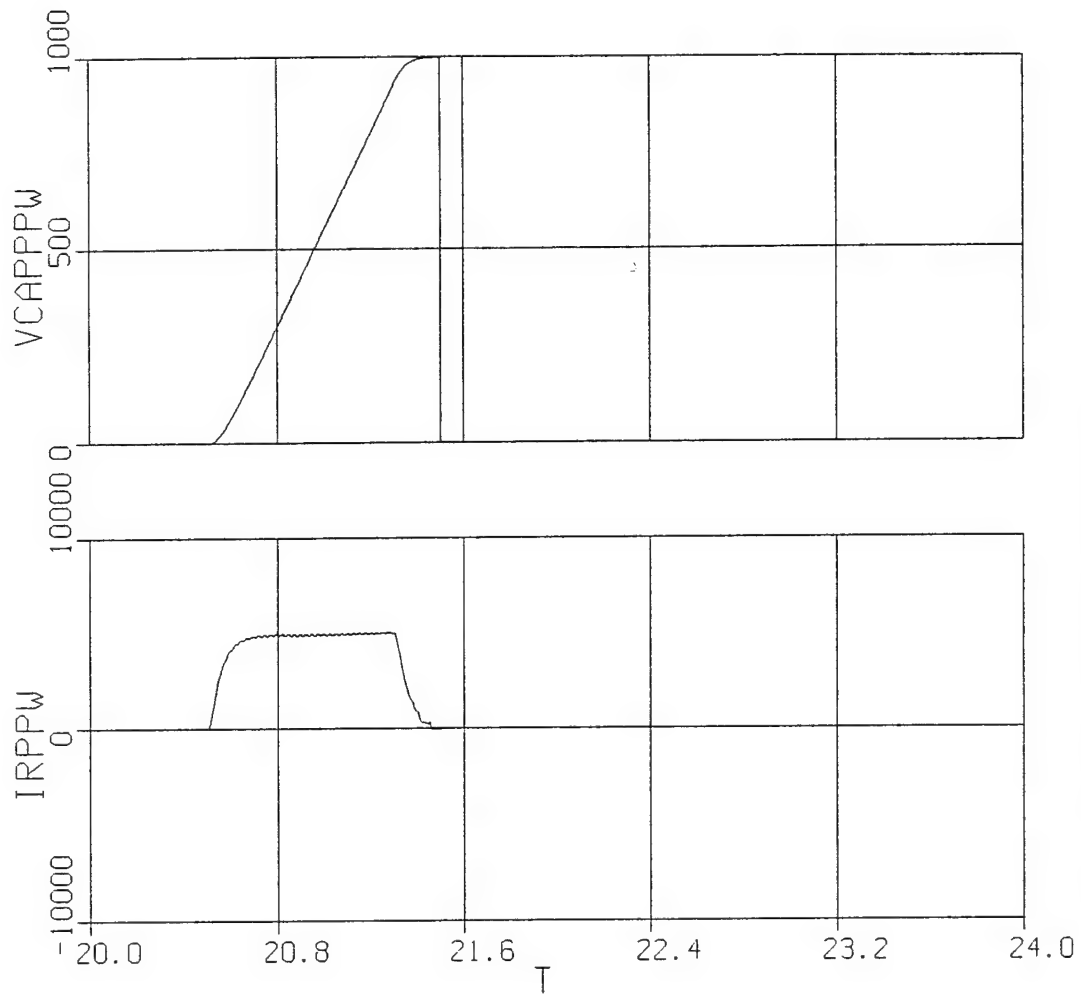


51 96/06/19 20:23:25



52 96/06/19 20:23:25



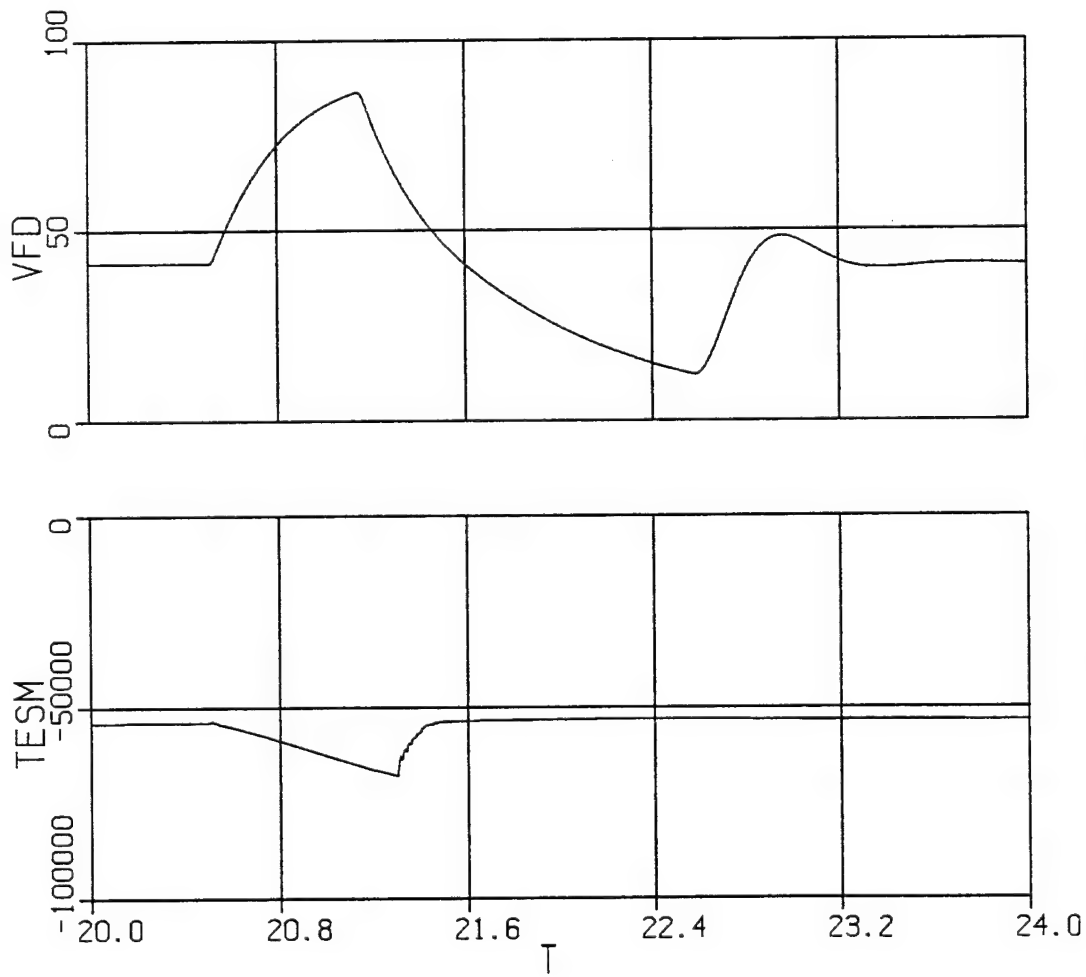


53 96/06/19 20:23:25

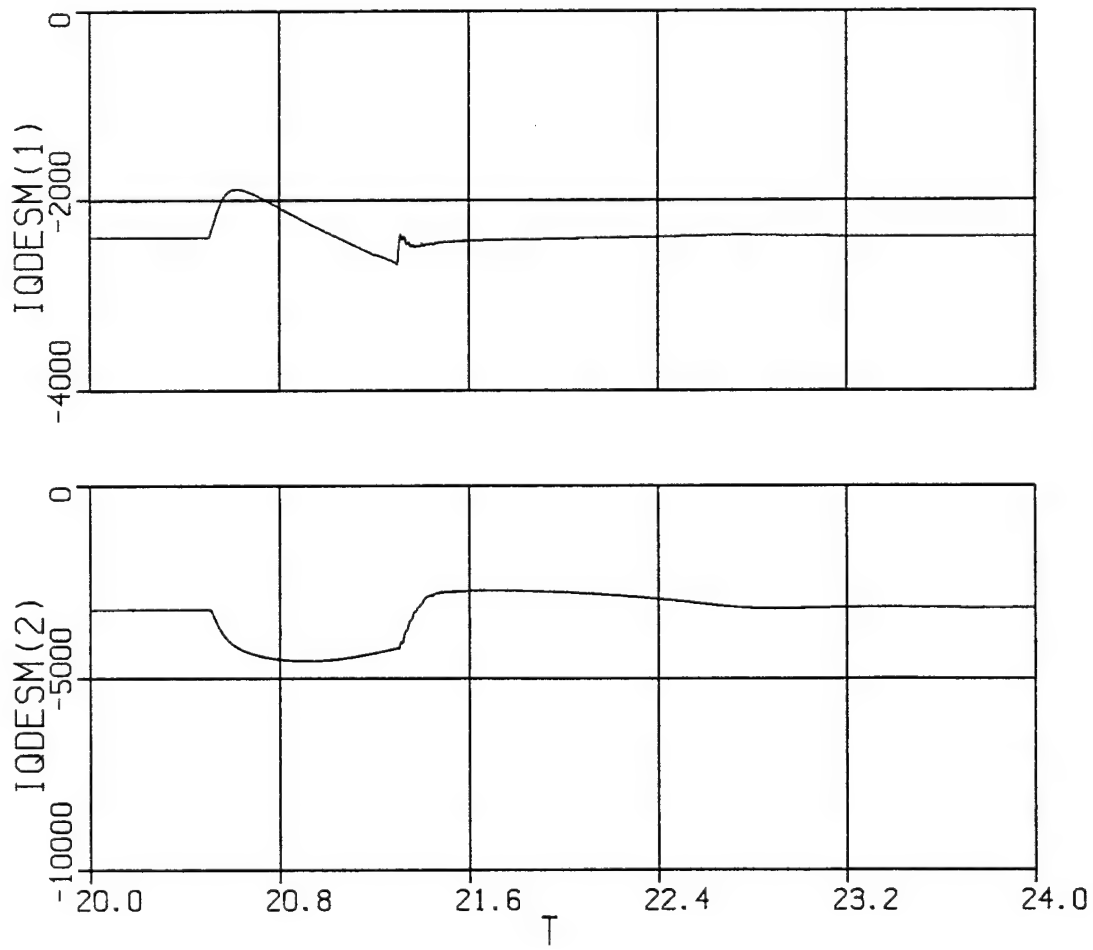
**Study 3b**

## Variable Description - Nonlinear Reduced-Order Model Simulation

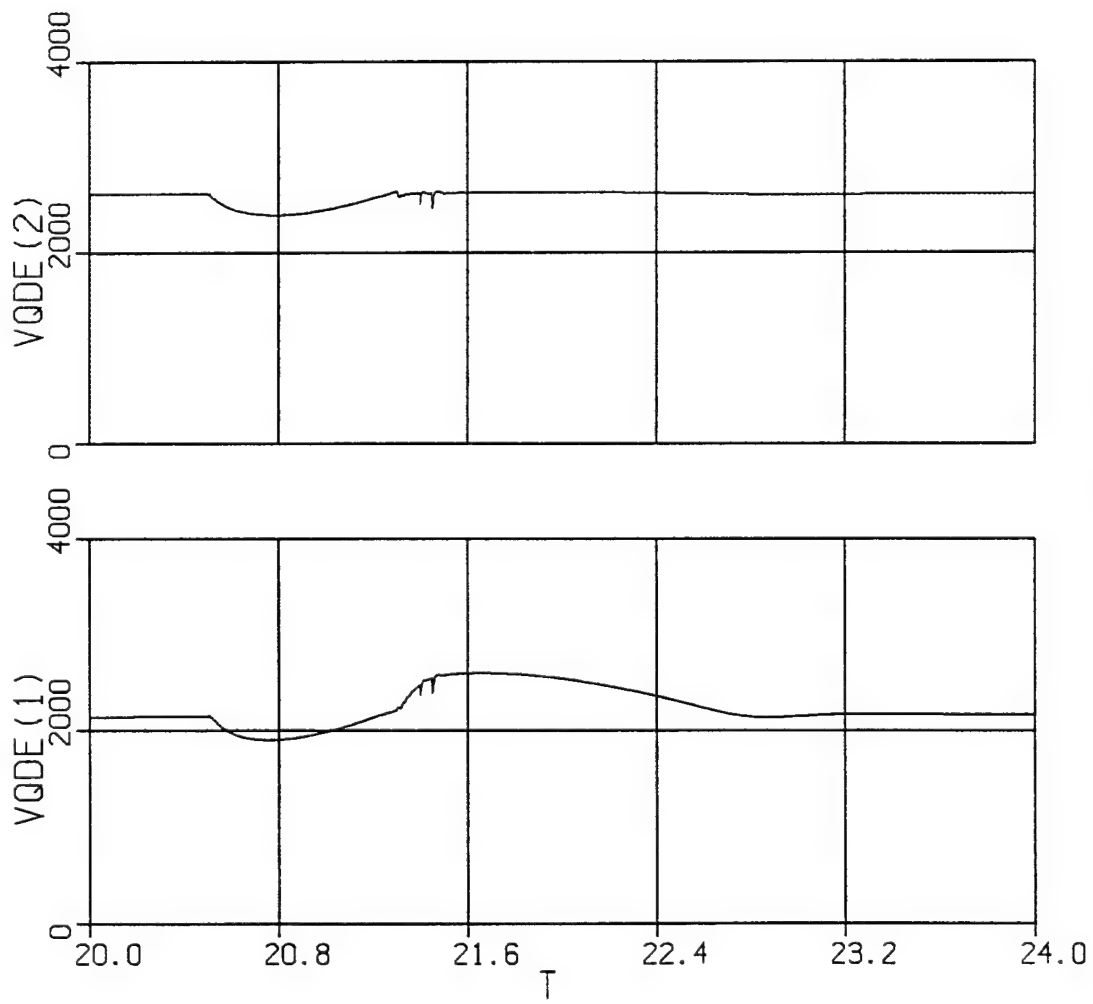
<u>ACSL Name</u>	<u>Description</u>
alphaspwsp	power supply rectifier phase delay (rad)
idcl1	inverter current into first set of five H-bridges (A)
iddepwsp(2)	d-axis current into pulse power device (A)
iqdeimc(1)	q-axis current into induction motor power converter (A)
iqdeimc(2)	d-axis current into induction motor power converter (A)
iqdepwsp(1)	q-axis current into pulse power device (A)
iqdepwsp(1)	q-axis current into power supply (A)
iqdepwsp(2)	d-axis current into power supply (A)
iqdesm(1)	q-axis synchronous machine current (positive in) (A)
iqdesm(2)	d-axis synchronous machine current (positive in) (A)
irectpwsp	dc link current in power supply (positive out of rectifier) (A)
irppw	inductor current in pulse power device (A)
teim1	induction motor electromagnetic torque (Nm)
tesm	synchronous machine torque (positive for motor operation) (Nm)
vcapppw	capacitor voltage of pulse power device (A)
vdc11	dc voltage at input of first 5 H-bridges (V)
vdcpwsp	power supply dc output voltage (V)
vfd	synchronous machine field voltage (unreferred) (V)
vqde(1)	q-axis bus voltage (V)
vqde(2)	d-axis bus voltage (V)
wrmim1	induction motor speed - mechanical (rad/s)



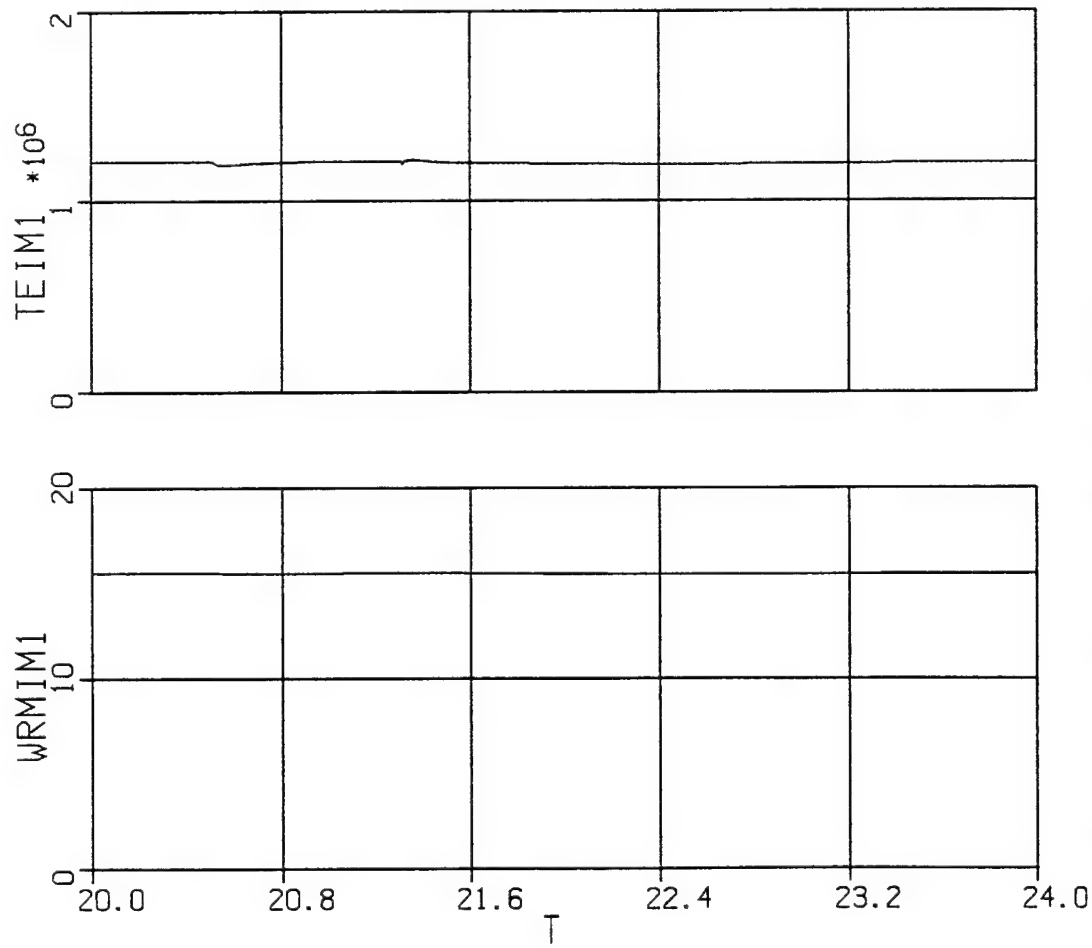
12 Jun 26 11:37:58 1996



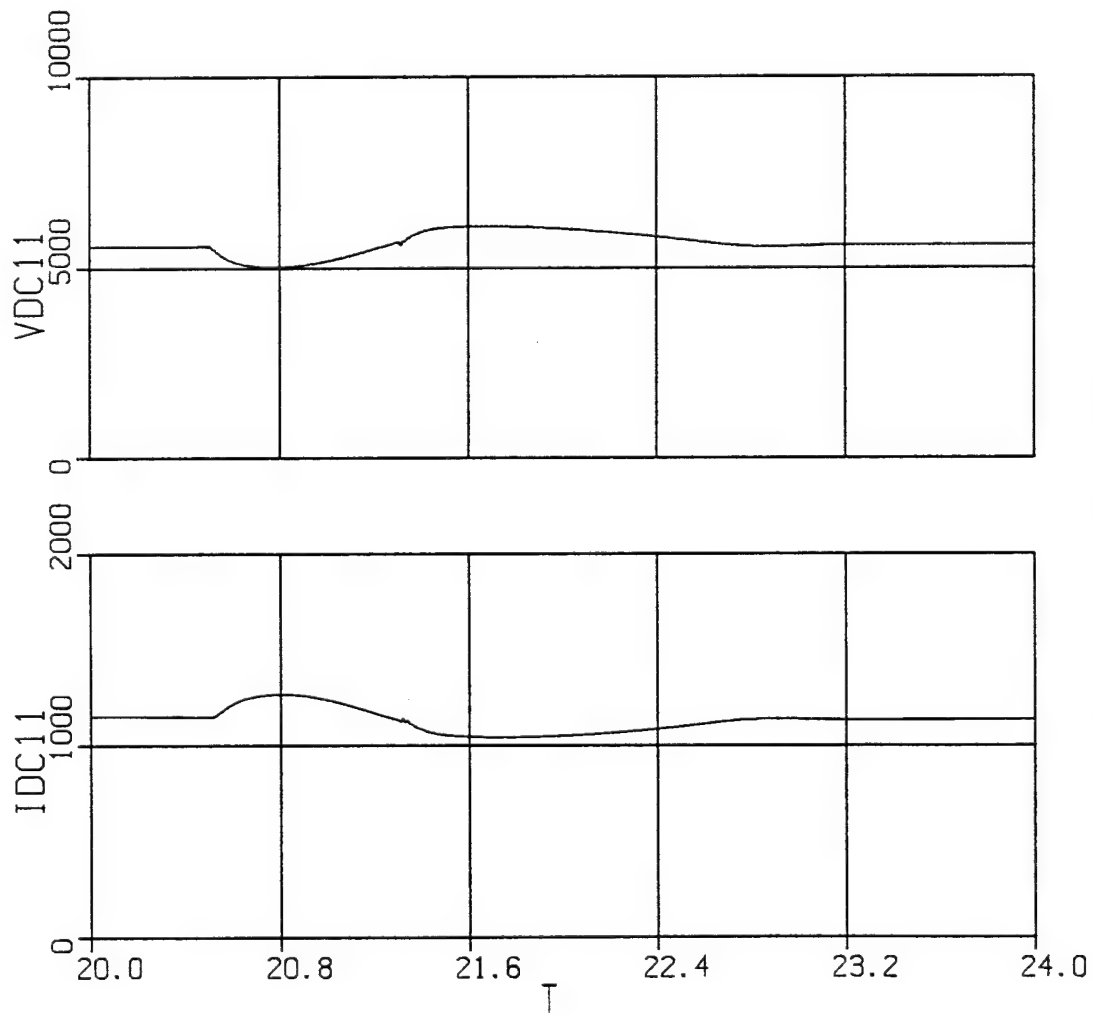
13 Jun 26 11:37:58 1996



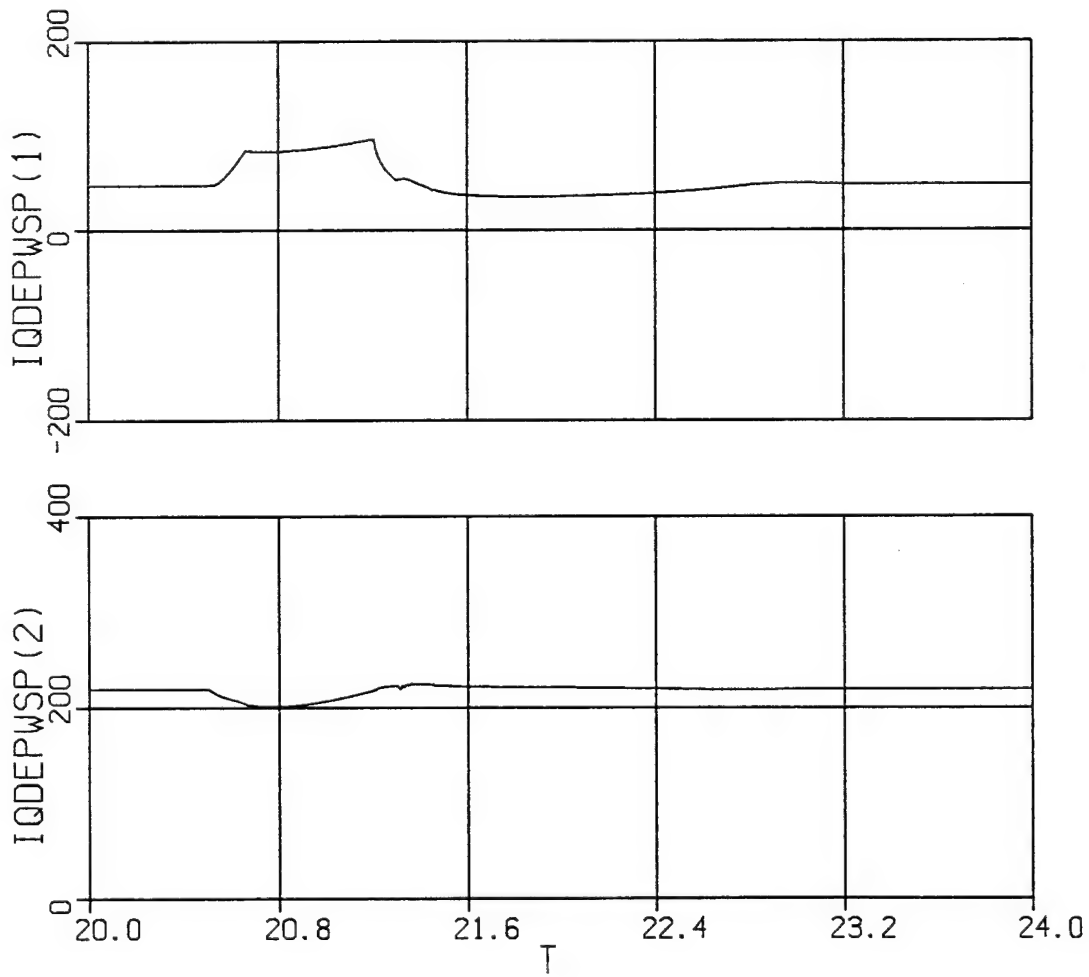
14 Jun 26 11:37:58 1996



15 Jun 26 11:37:58 1996

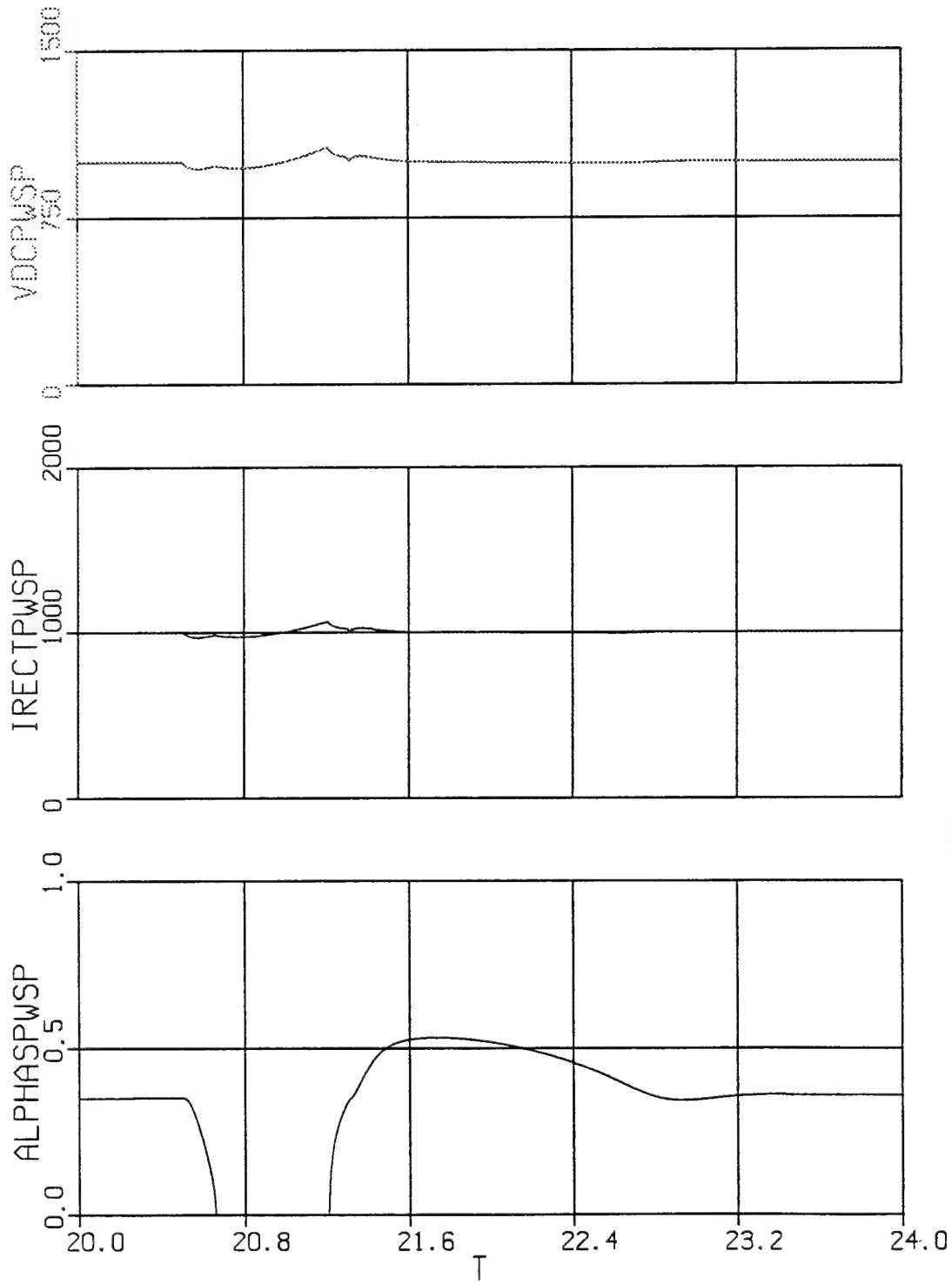


16 Jun 26 11:37:58 1996

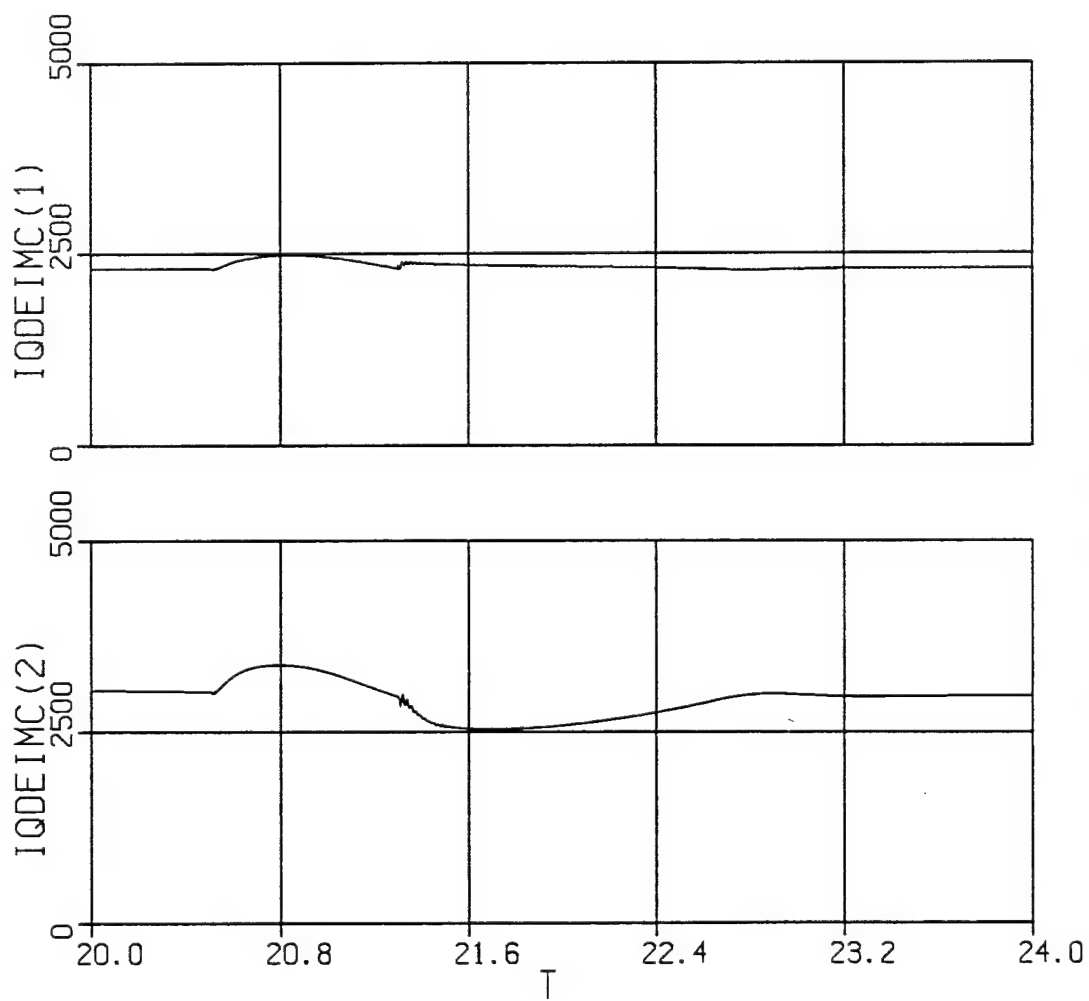


17 Jun 26 11:37:58 1996

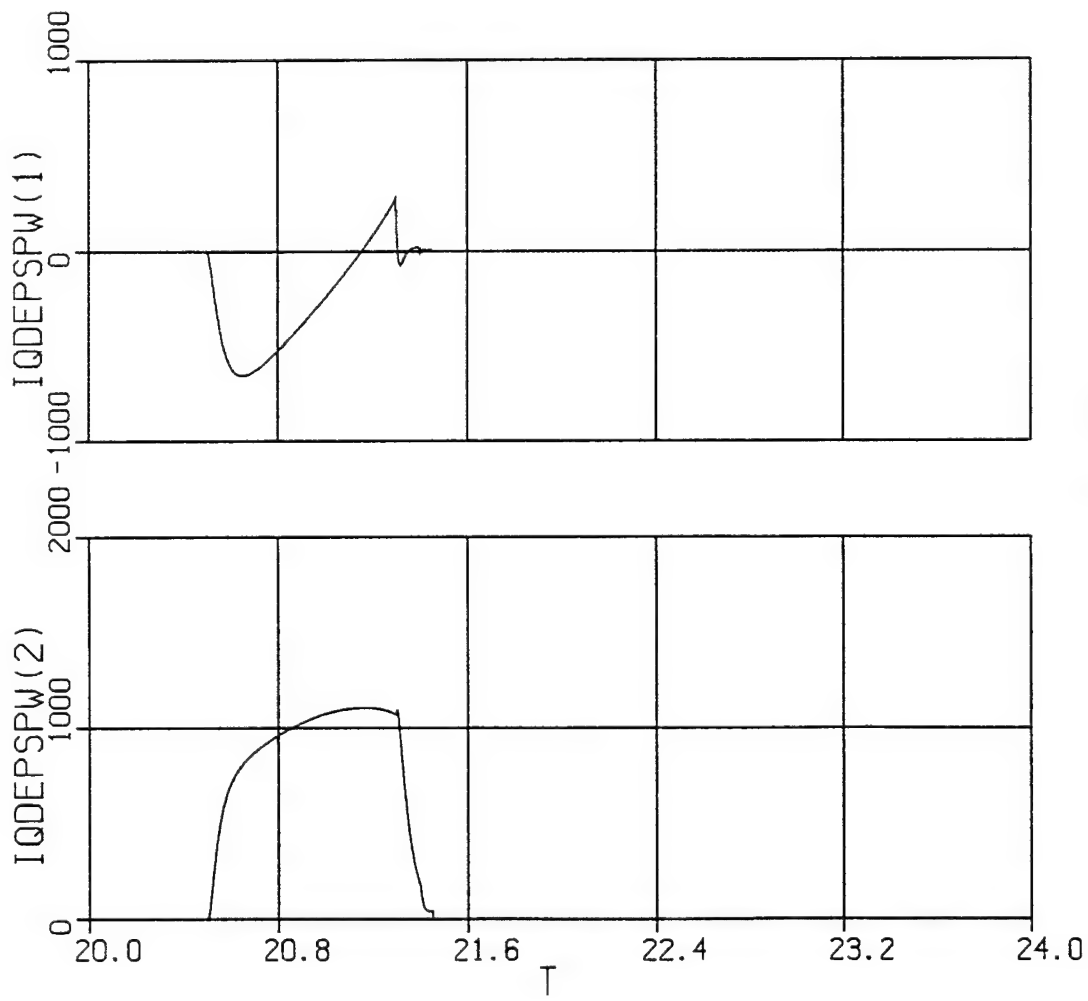




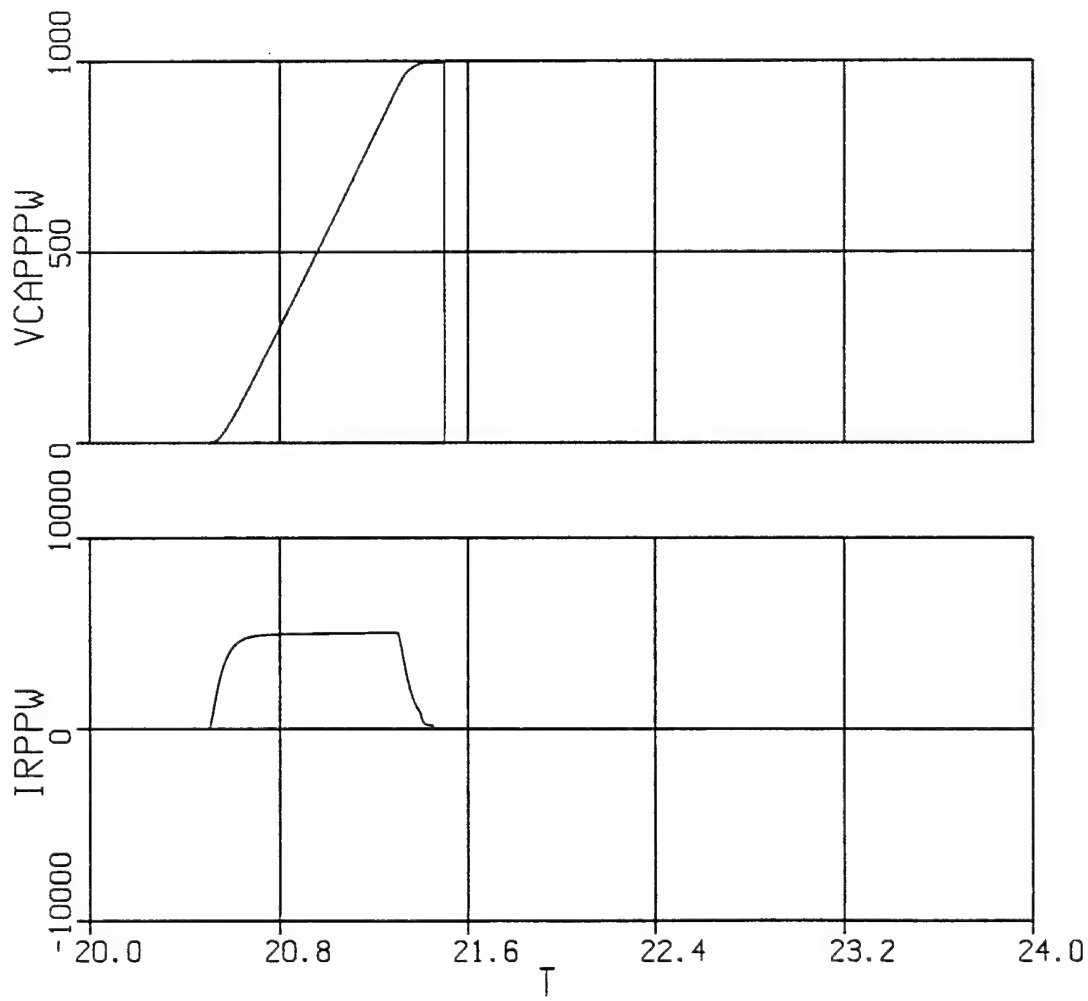
18 Jun 26 11:37:58 1996



19 Jun 26 11:37:58 1996



2 Jun 26 12:01:17 1996



4 Jun 26 11:52:40 1996

### Study 4

The system is initially operating with the propulsion system and ship service power supply operating at full load with the stabilizing control incorporated into the vector control of the propulsion induction motor. At  $t = 24.5$  the pulsed power weapon is fired and at the same time the stabilizing control is deactivated whereupon the propulsion induction motor is controlled by the "standard" vector control. During the operation of the weapon, the instability due to the standard vector control is noted in the waveforms. Compare TESM in Study 3 to TESM in Study 4. However, once the weapon has discharged the instability is more or less present only in the dc variables as illustrated by the plots of VDC11 and IDC11F. Note that with the stabilizer, before the firing, the variables are stable; however, after the firing, when the stabilizer is out-of-service, the variables demonstrate instability. In Study 3, wherein the stabilizer was in service, the variables return to the pre-firing stable waveforms.

In the case of the reduced-order simulation, the plots stop at approximately  $t = 25.4$ . This is due to the fact that the reduced-order model detects that a commutation failure occurred and subsequently stopped computing since thereafter the reduced-order model is no longer valid.

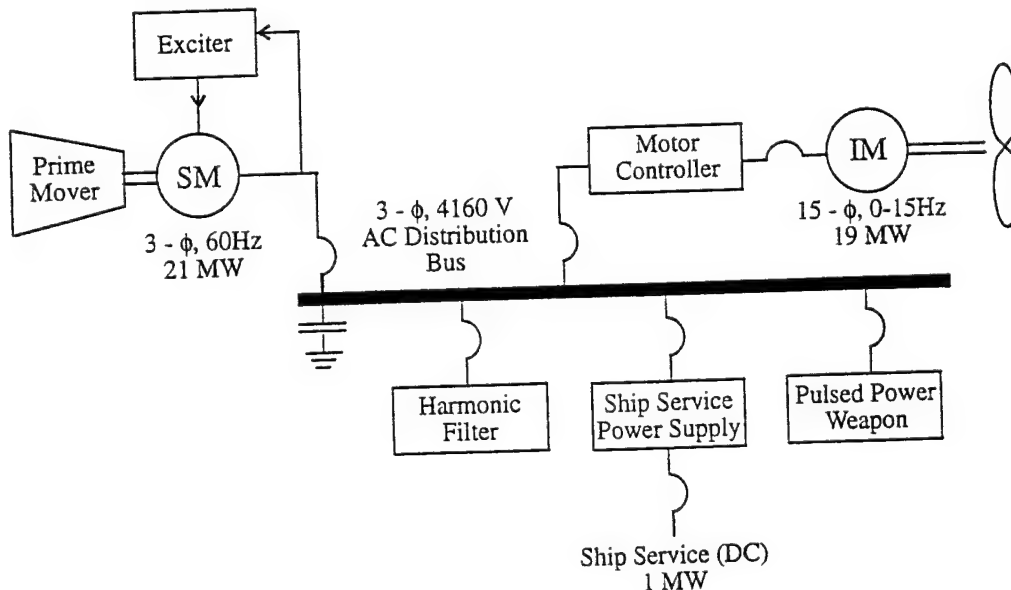
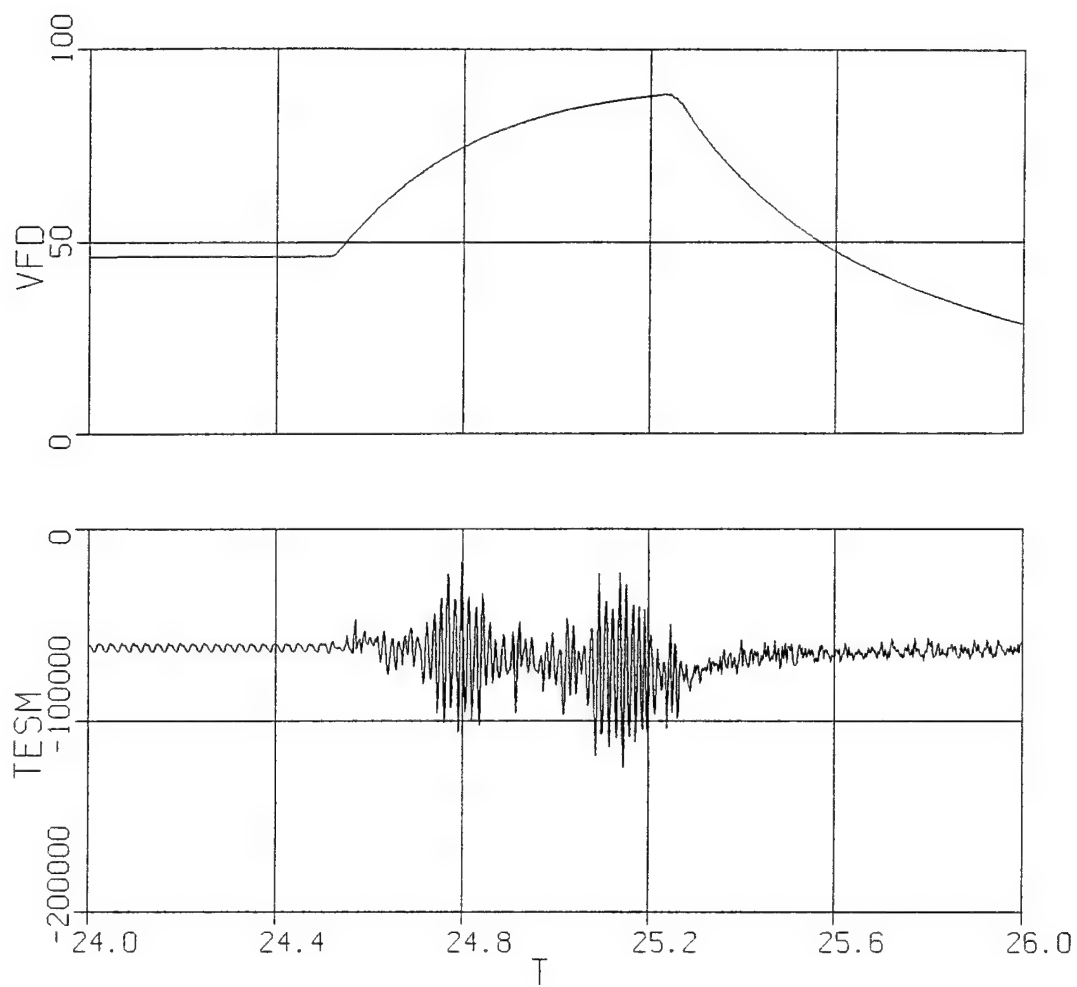


Figure 1. System studied.

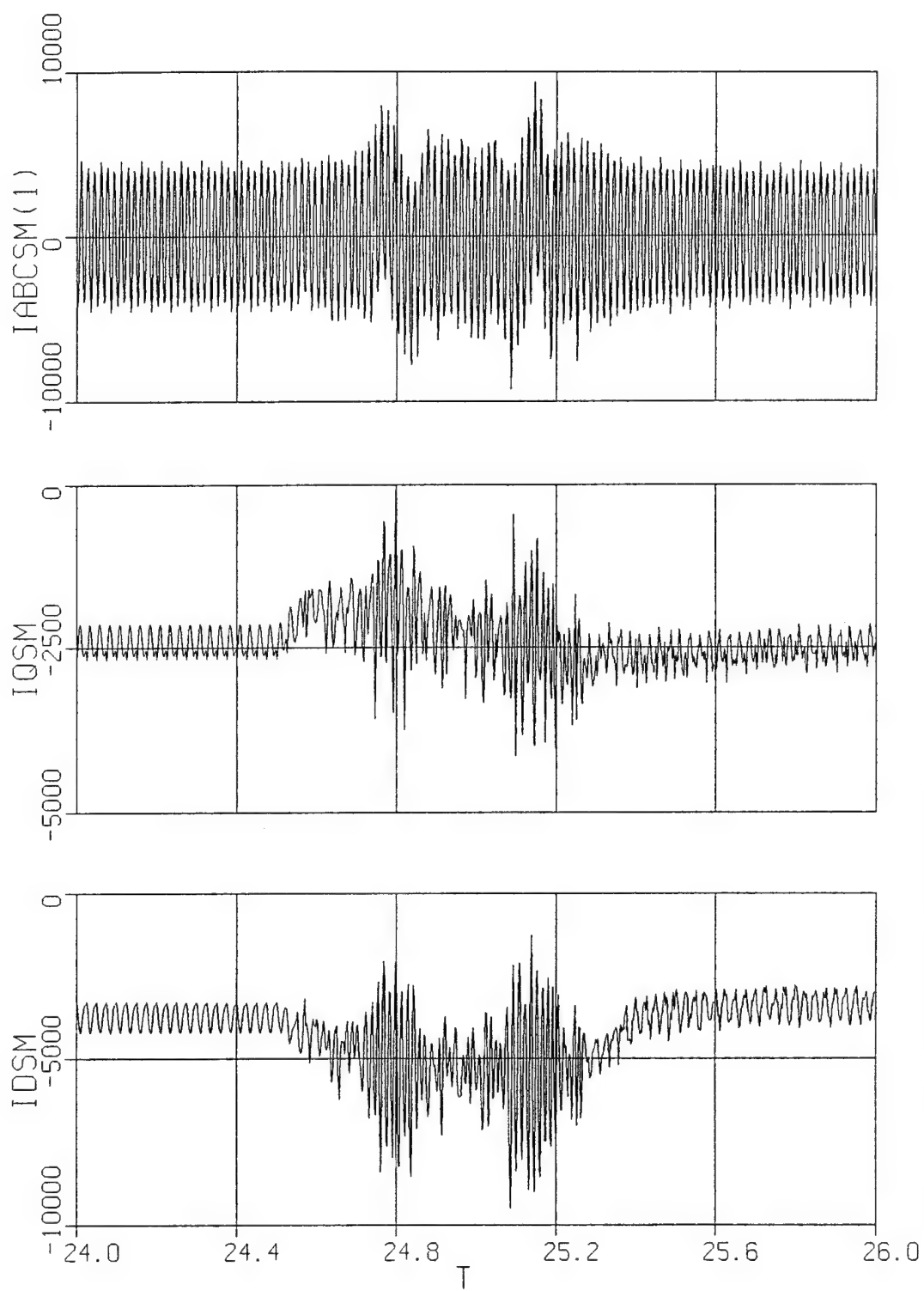
## Study 4a

## Variable Description - Detailed Simulation

<u>ACSL Name</u>	<u>Description</u>
alphapwsp	power supply rectifier phase delay (rad)
iabcimc(1)	a-phase current into induction motor power converter (A)
iabcppw(1)	a-phase current into pulse power device (A)
iabcpwsp(1)	a-phase current into power supply (A)
iabcs(1)	a-phase synchronous machine current (positive in) (A)
iaom1(1)	a-phase induction motor current (A)
idc11	dc current into first 5 H-bridge inverter (not filtered) (A)
idc11f	low pass filtered inverter current into first set of five H-bridges (filtered so it could be compared to average value model) (A)
iddrv	d-axis current into induction motor power converter (A)
idppw	d-axis current into pulse power device (A)
idpwsp	d-axis current into power supply (A)
idsm	d-axis synchronous machine current (positive in) (A)
iqdrv	q-axis current into induction motor power converter (A)
iqppw	q-axis current into pulse power device (A)
iqpwsp	q-axis current into power supply (A)
iqsm	q-axis synchronous machine current (positive in) (A)
irectpwsp	dc link current in power supply (positive out of rectifier) (A)
irppw	inductor current in pulse power device (A)
teim1	induction motor electromagnetic torque (Nm)
tesm	synchronous machine torque (positive for motor operation) (Nm)
vabc(1)	a-phase 4160 V bus voltage (V)
vaom1(1)	a-phase induction motor voltage (V)
vcappw	capacitor voltage of pulse power device (A)
vd	d-axis bus voltage (V)
vdc11	dc voltage at input of first 5 H-bridges (V)
vdcpwsp	power supply dc output voltage (V)
vfd	synchronous machine field voltage (unreferred) (V)
vq	q-axis bus voltage (V)
wrmim1	induction motor speed - mechanical (rad/s)

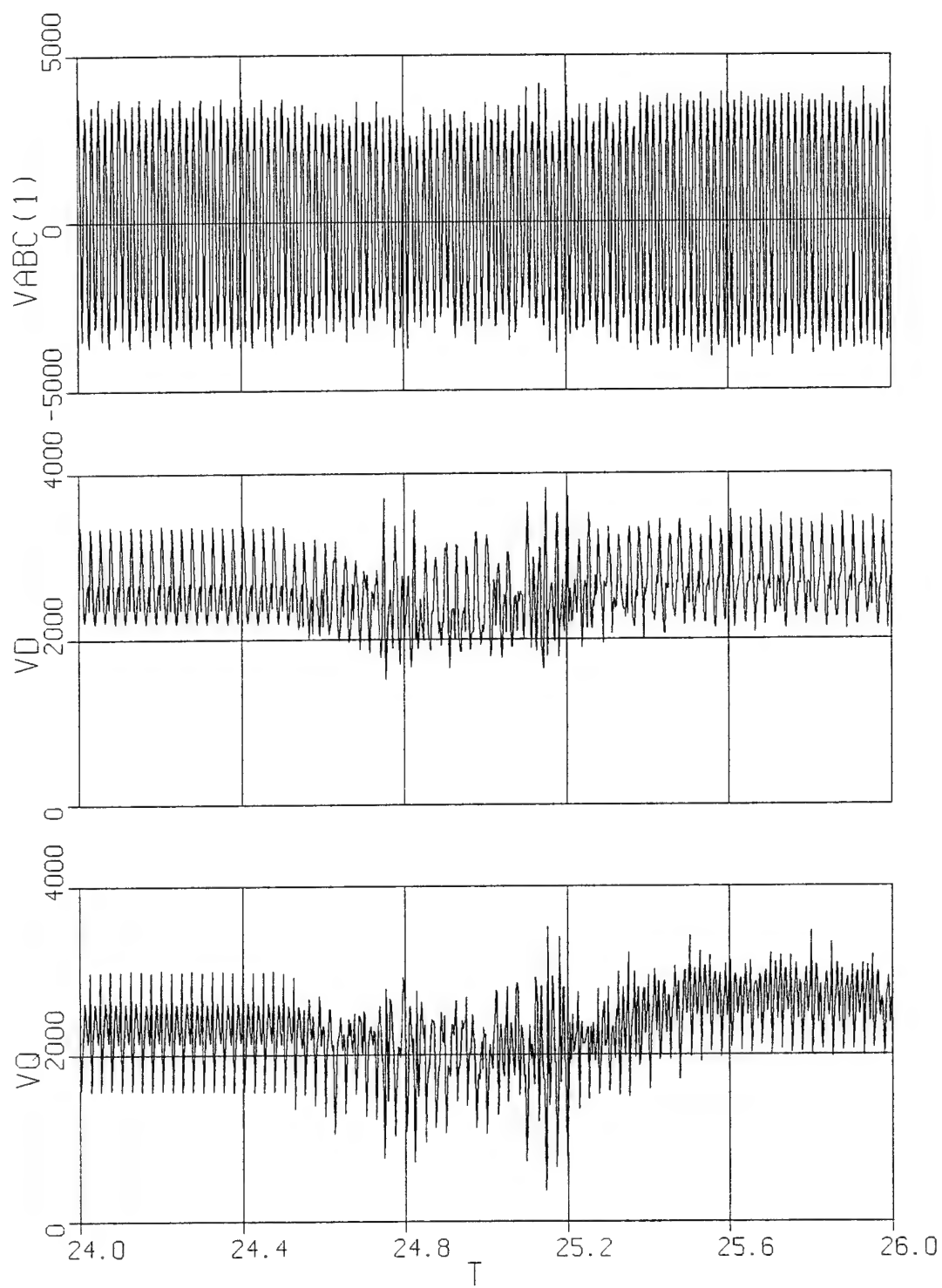


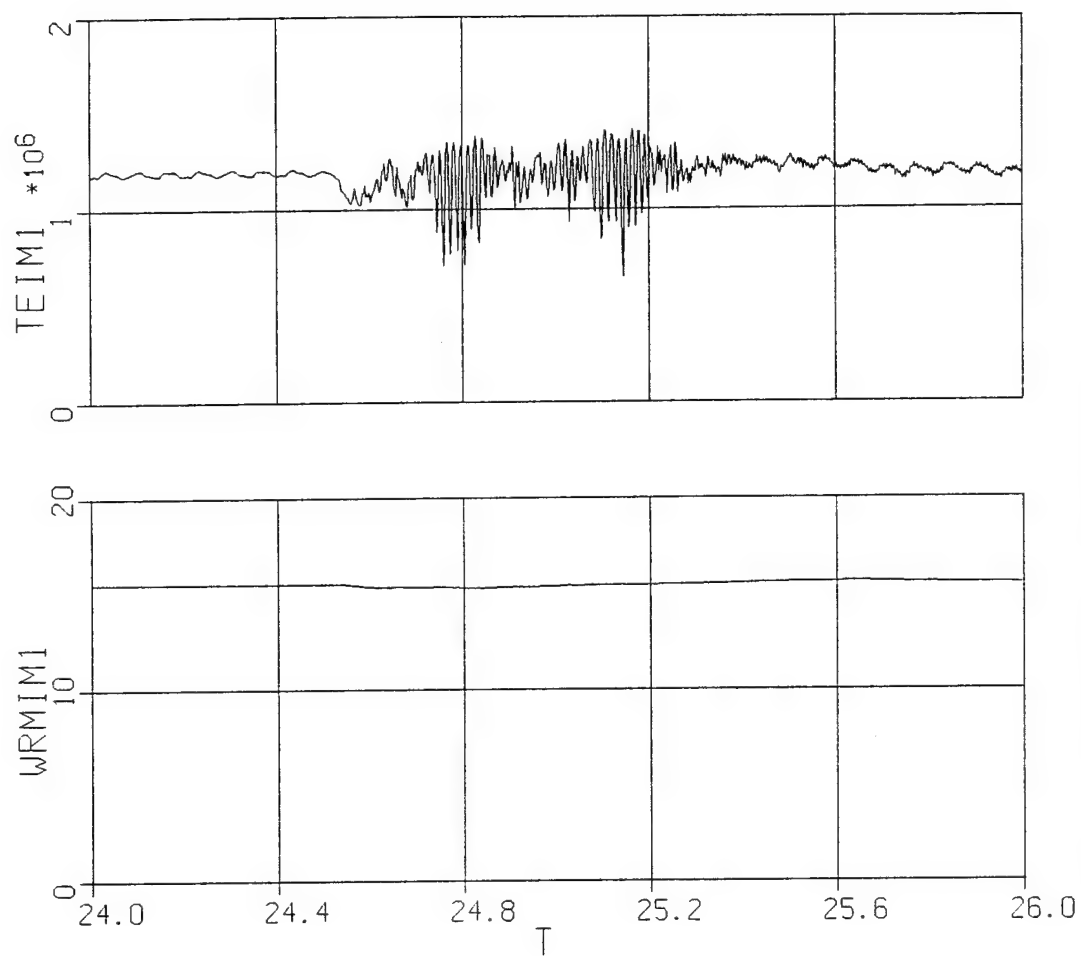
55 96/06/19 20:23:25



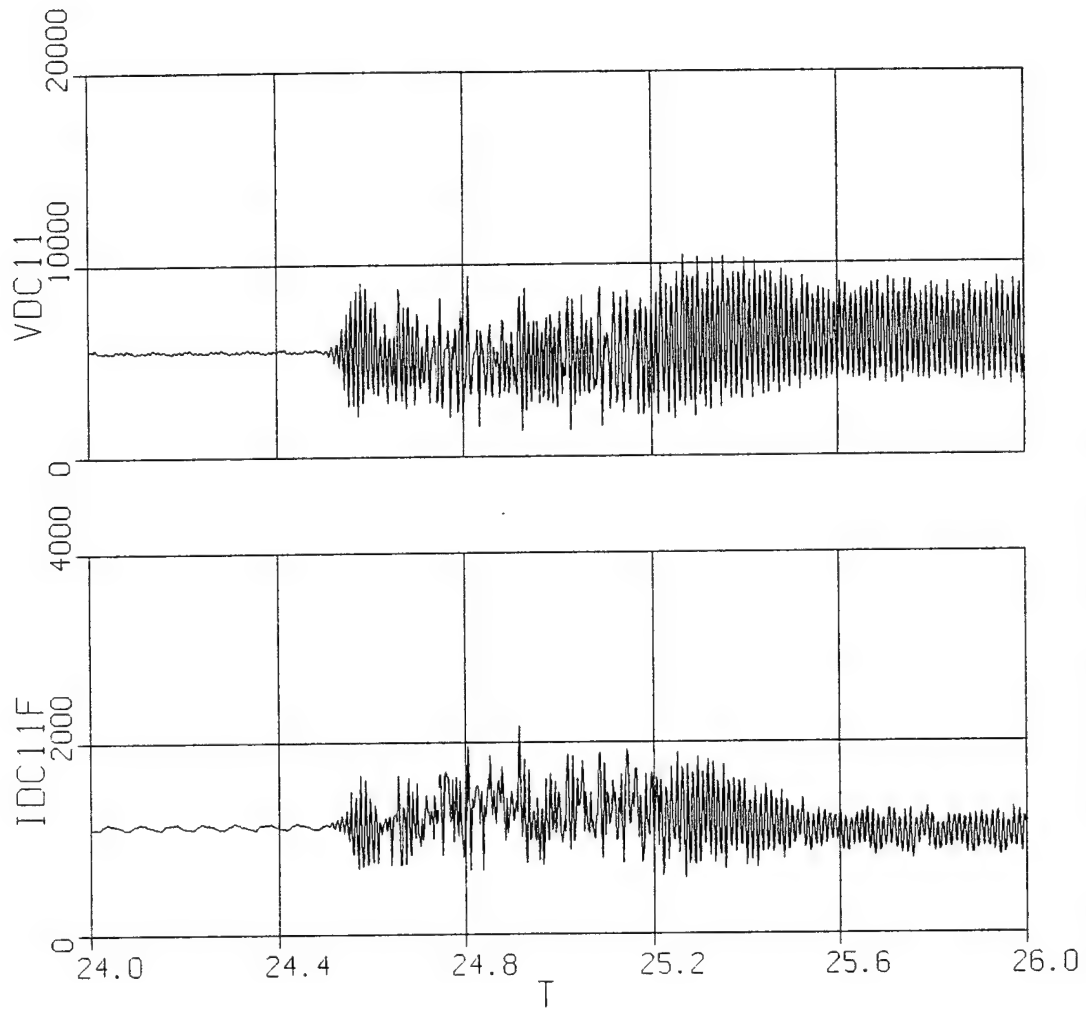
56 96/06/19 20:23:25



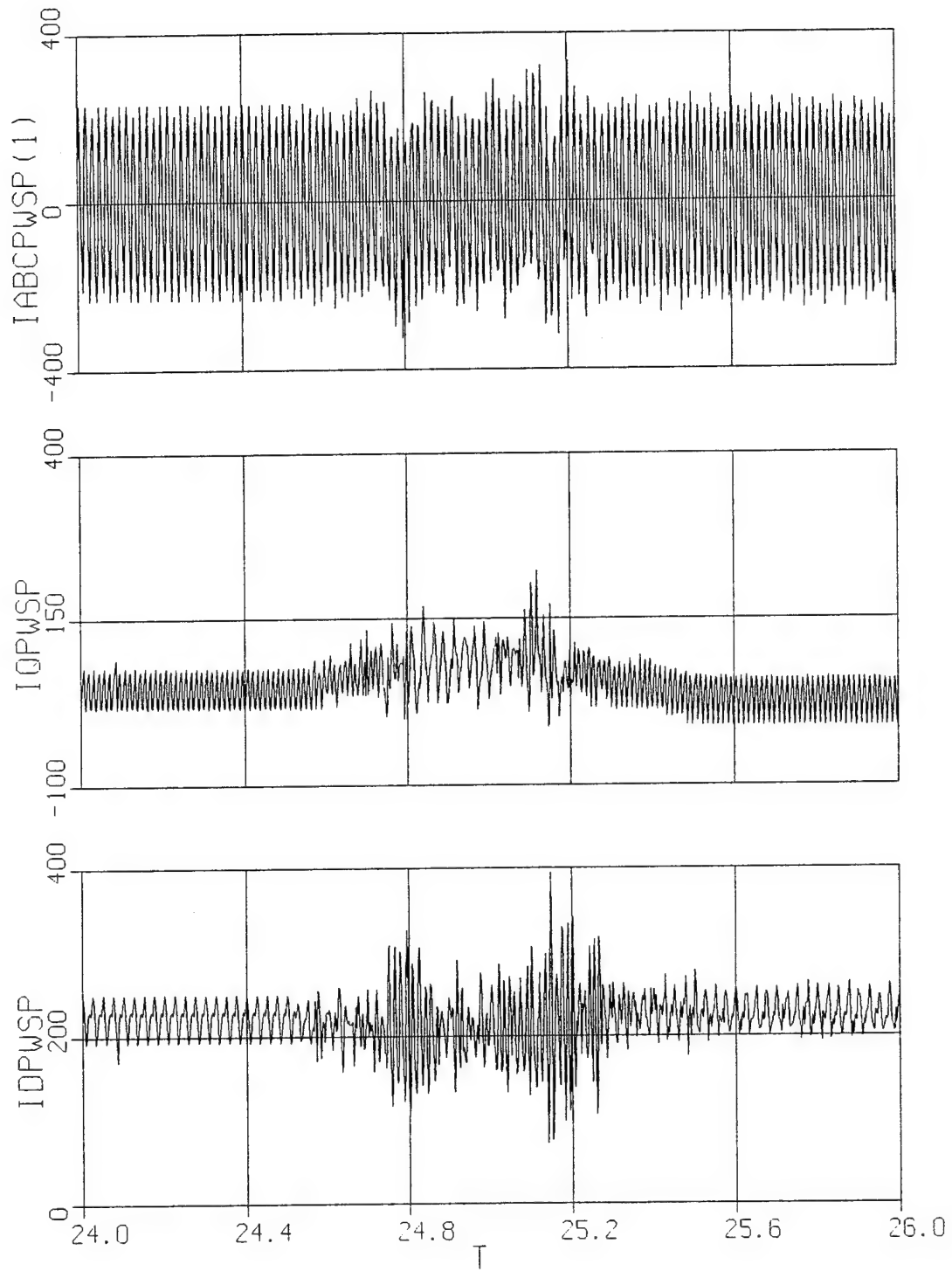




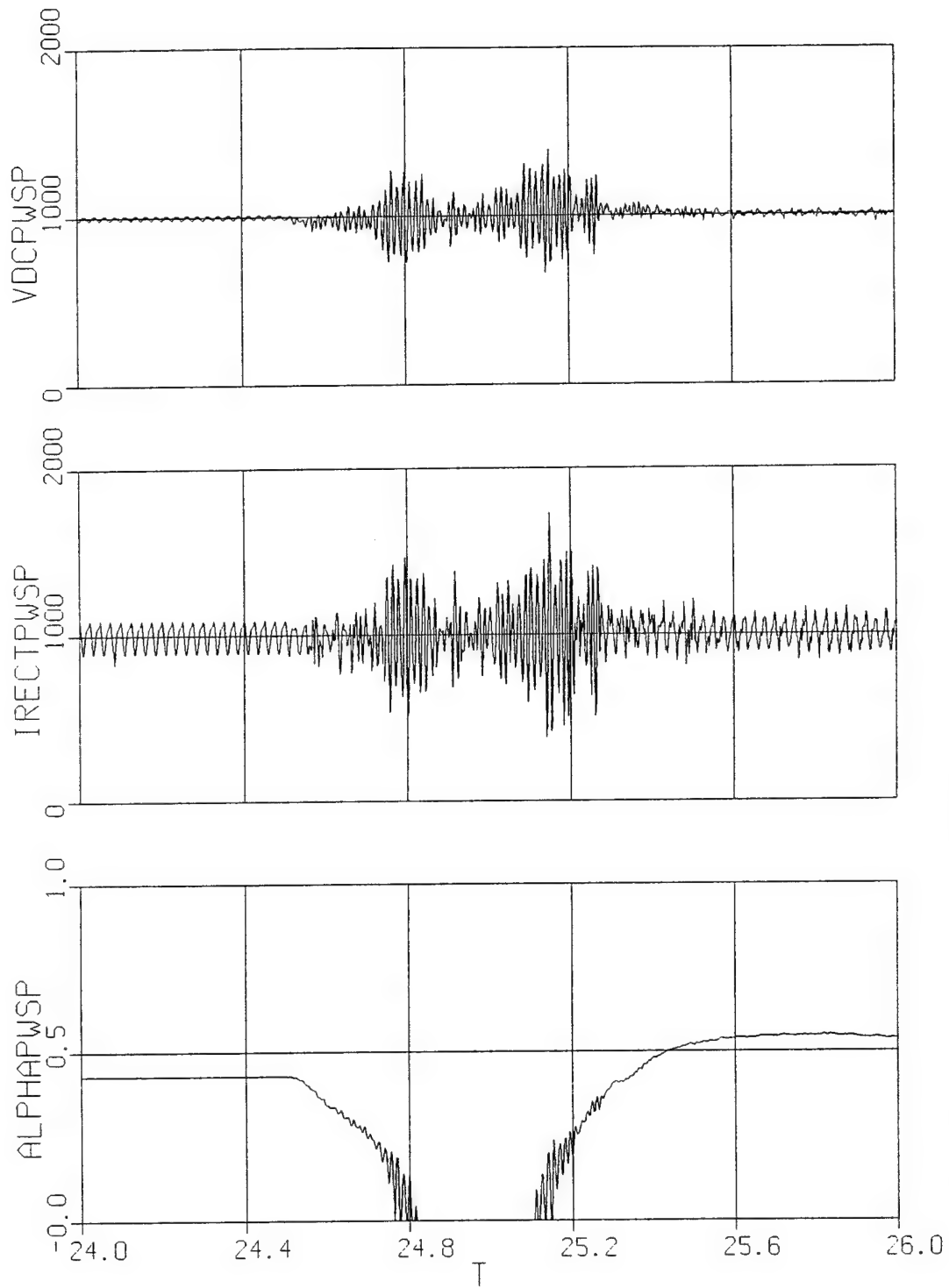
59 96/06/19 20:23:25



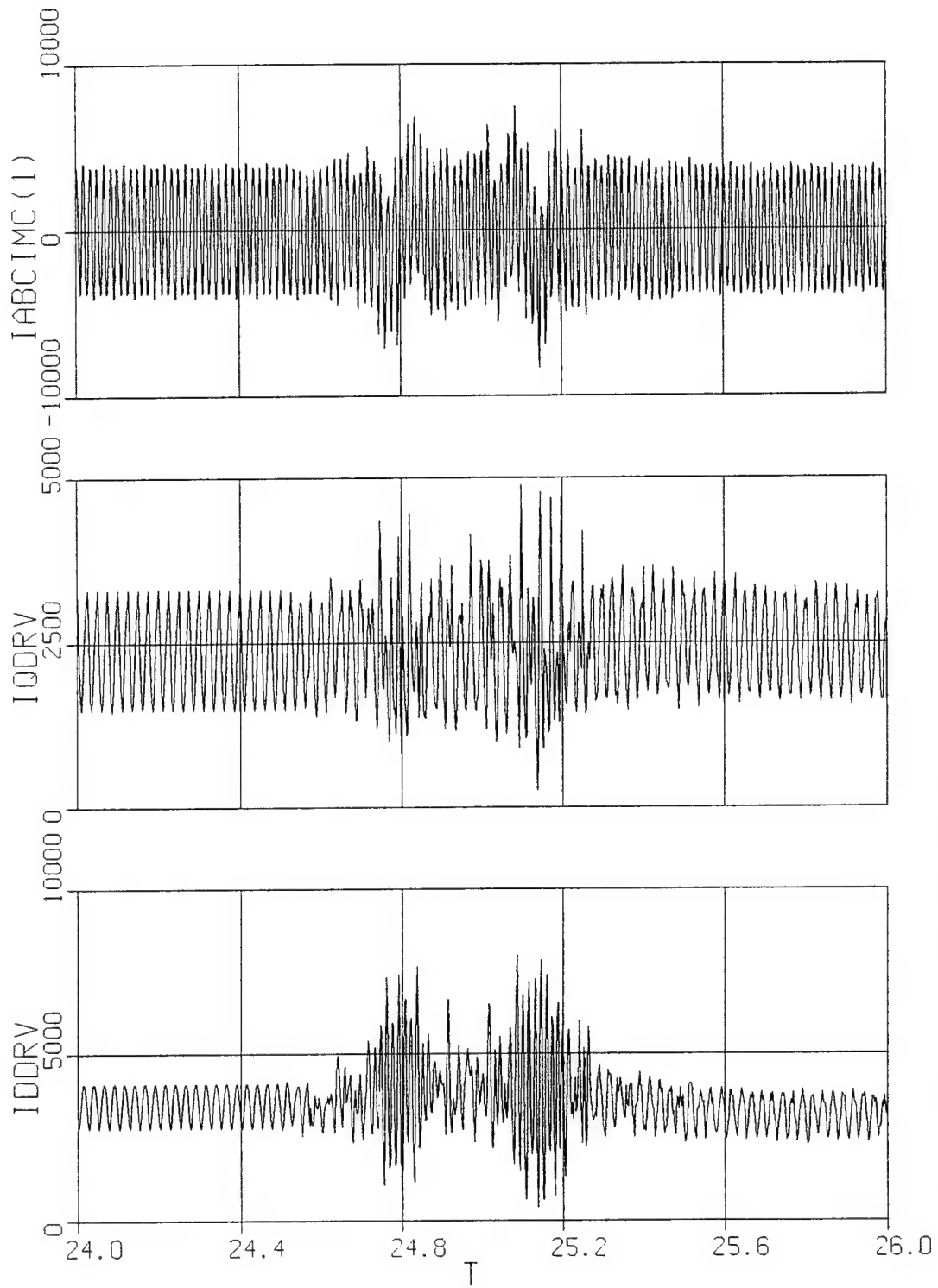
60 96/06/19 20:23:25



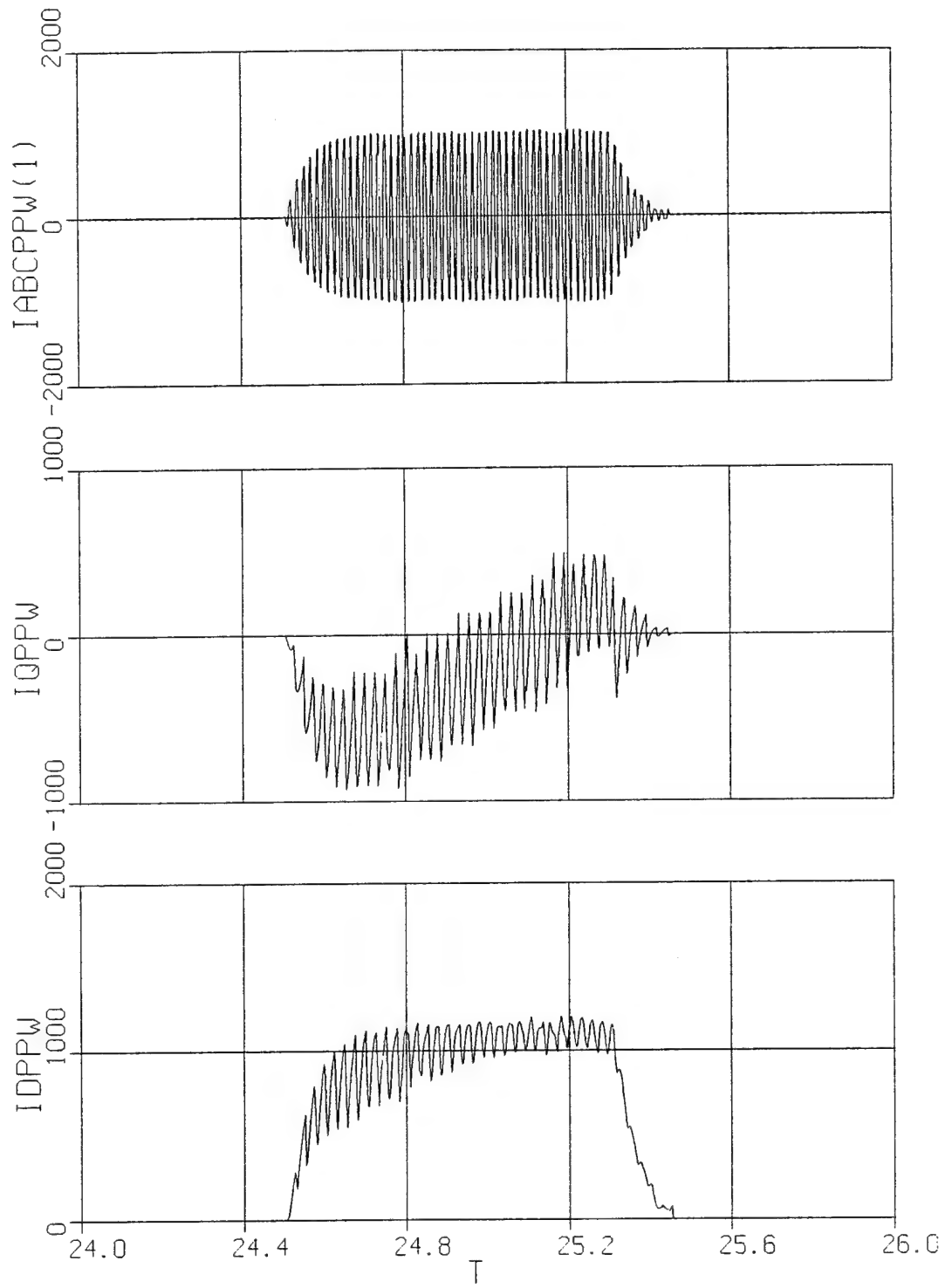
63 96/06/19 20:23:25



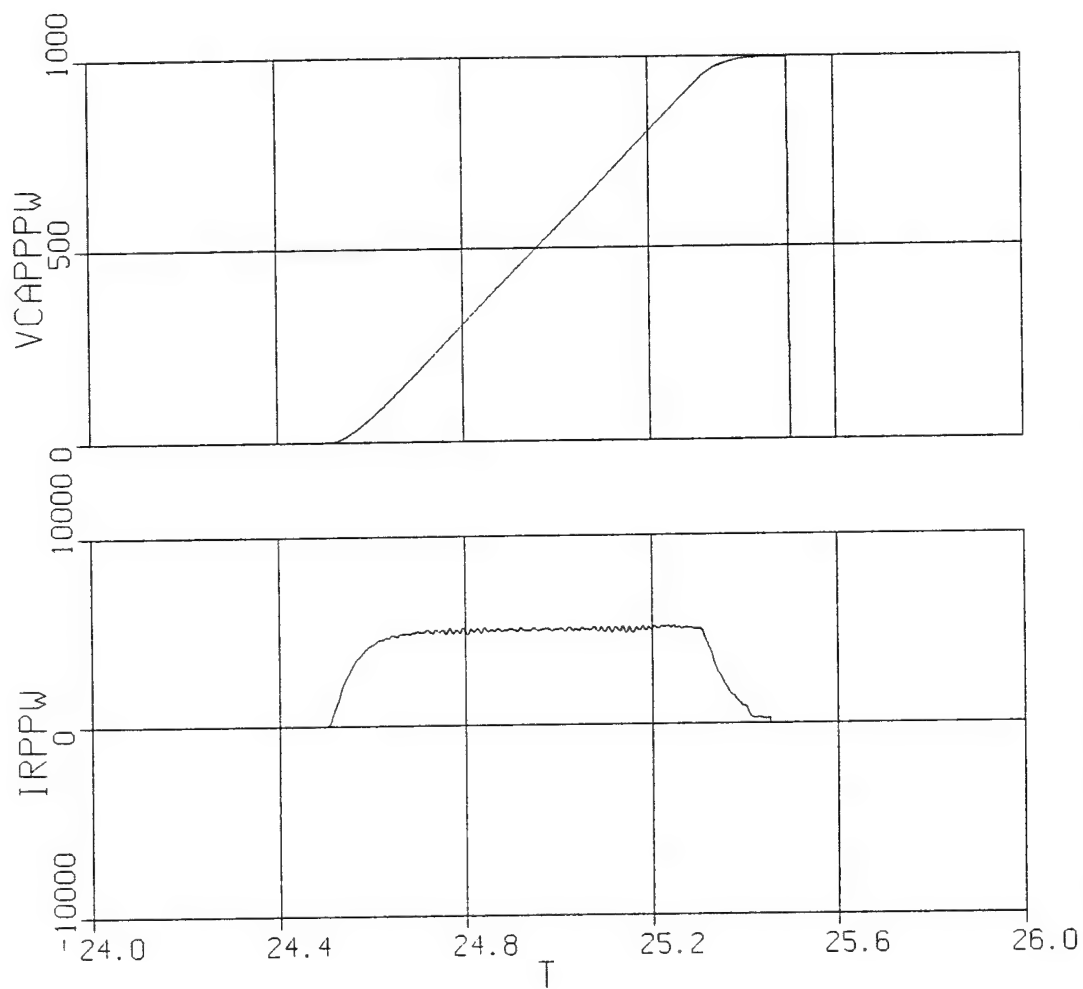
64 96/06/19 20:23:25



65 96/06/19 20:23:25



66 96/06/19 20:23:25



67 96/06/19 20:23:25

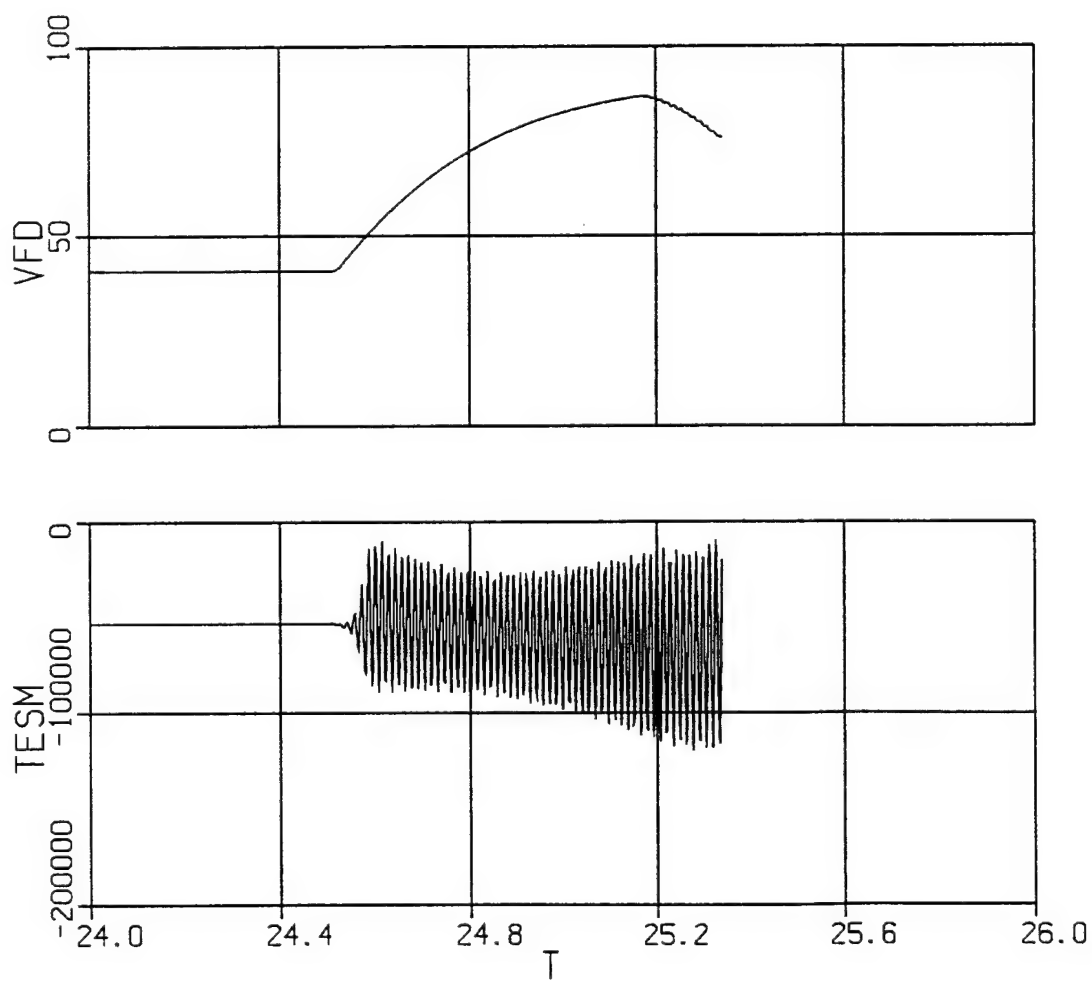
study 4  
plot 10



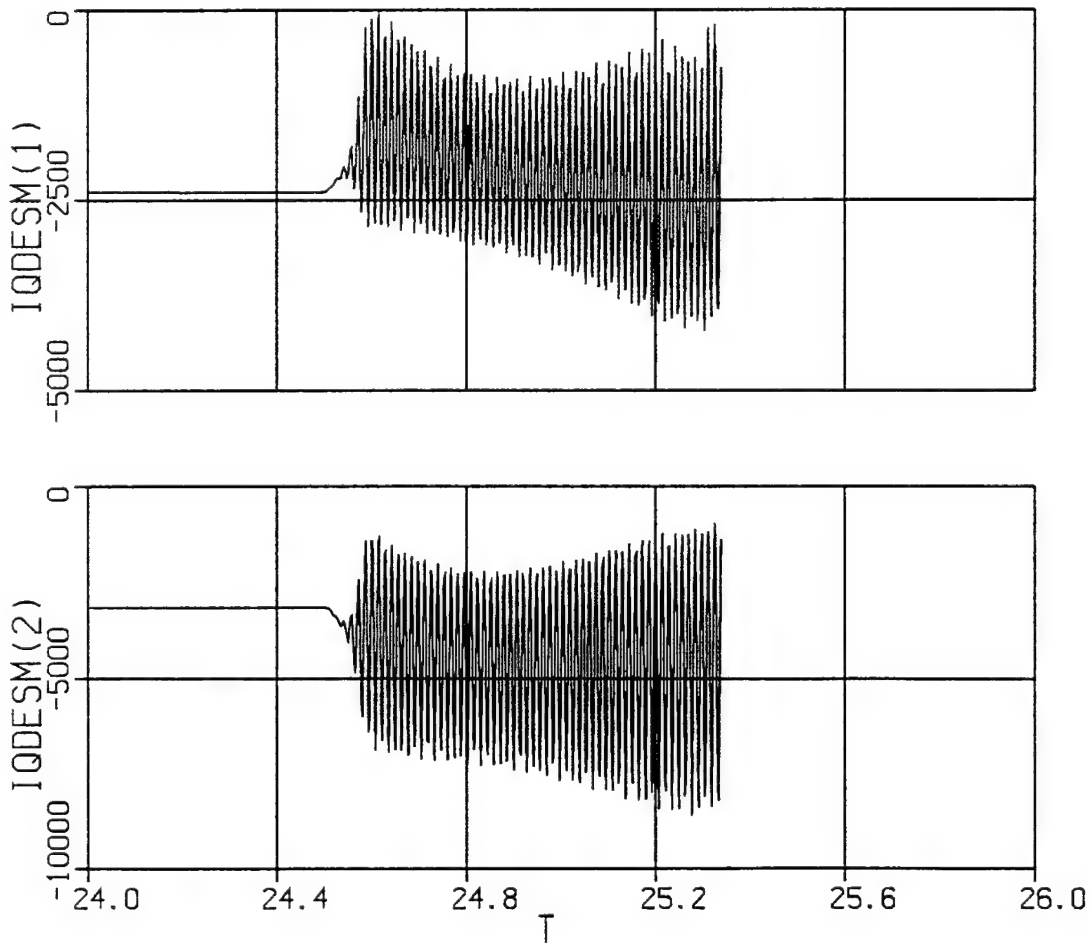
**Study 4b**

## Variable Description - Nonlinear Reduced-Order Model Simulation

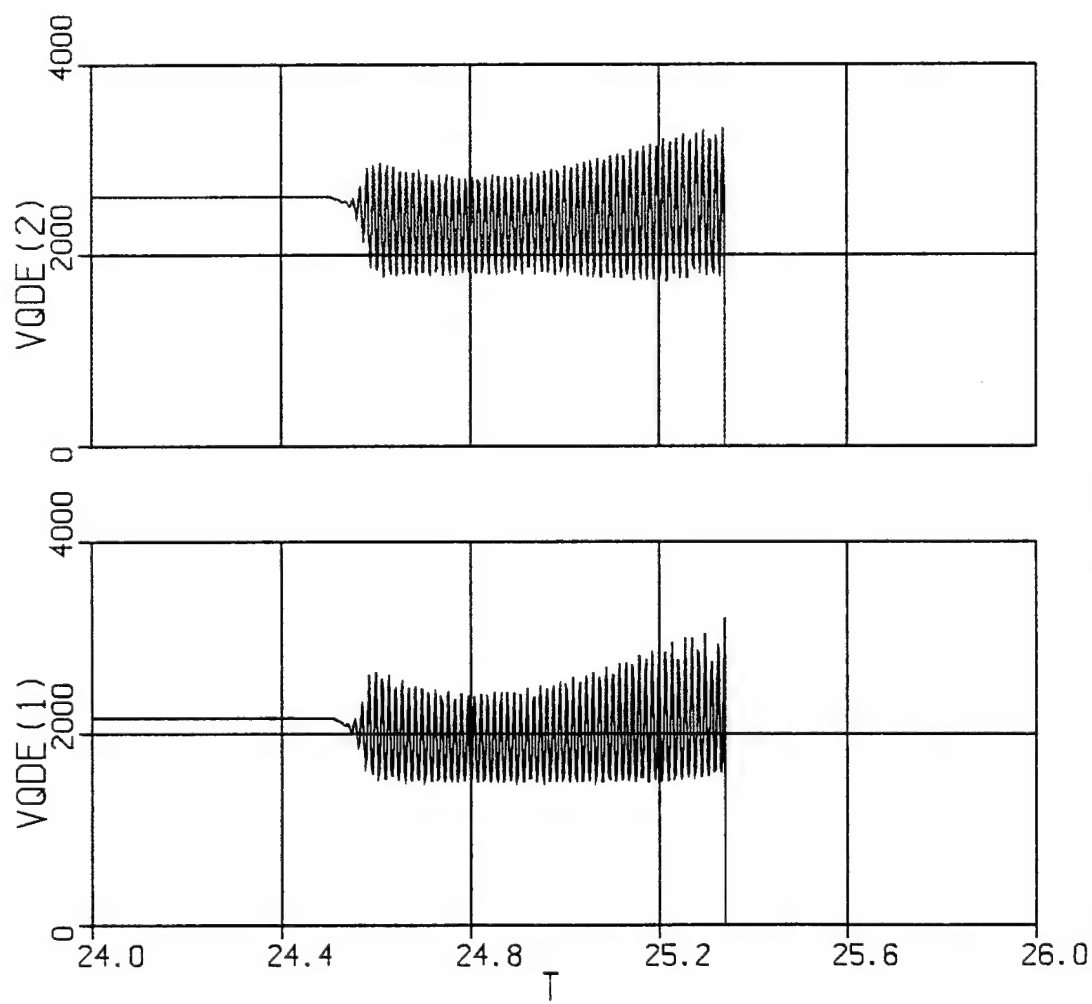
<u>ACSL Name</u>	<u>Description</u>
alphaspwsp	power supply rectifier phase delay (rad)
idcl1	inverter current into first set of five H-bridges (A)
iddepwsp(2)	d-axis current into pulse power device (A)
iqdeimc(1)	q-axis current into induction motor power converter (A)
iqdeimc(2)	d-axis current into induction motor power converter (A)
iqdepwsp(1)	q-axis current into pulse power device (A)
iqdepwsp(1)	q-axis current into power supply (A)
iqdepwsp(2)	d-axis current into power supply (A)
iqdesm(1)	q-axis synchronous machine current (positive in) (A)
iqdesm(2)	d-axis synchronous machine current (positive in) (A)
irectpwsp	dc link current in power supply (positive out of rectifier) (A)
irppw	inductor current in pulse power device (A)
teiml	induction motor electromagnetic torque (Nm)
tesm	synchronous machine torque (positive for motor operation) (Nm)
vcapppw	capacitor voltage of pulse power device (A)
vdc11	dc voltage at input of first 5 H-bridges (V)
vdcpwsp	power supply dc output voltage (V)
vfd	synchronous machine field voltage (unreferred) (V)
vqde(1)	q-axis bus voltage (V)
vqde(2)	d-axis bus voltage (V)
wrmiml	induction motor speed - mechanical (rad/s)



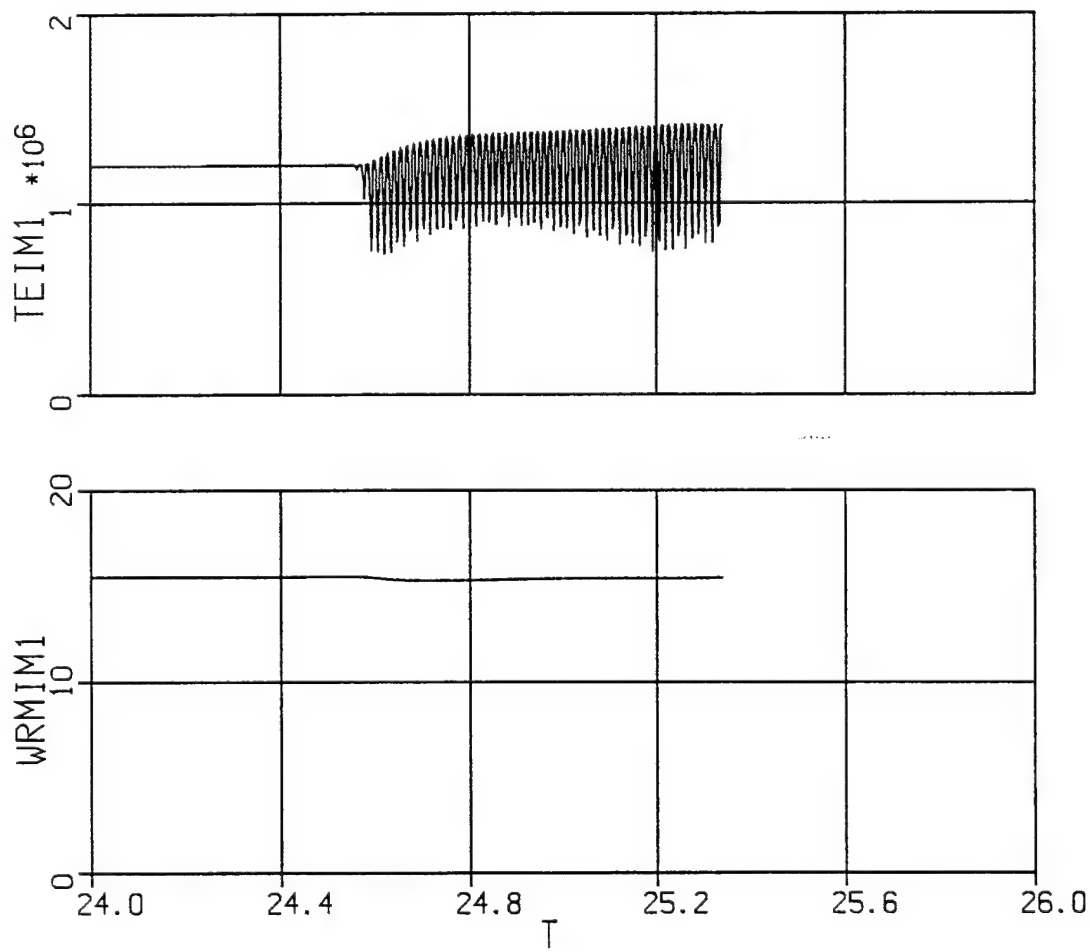
8 Jun 26 11:52:40 1996



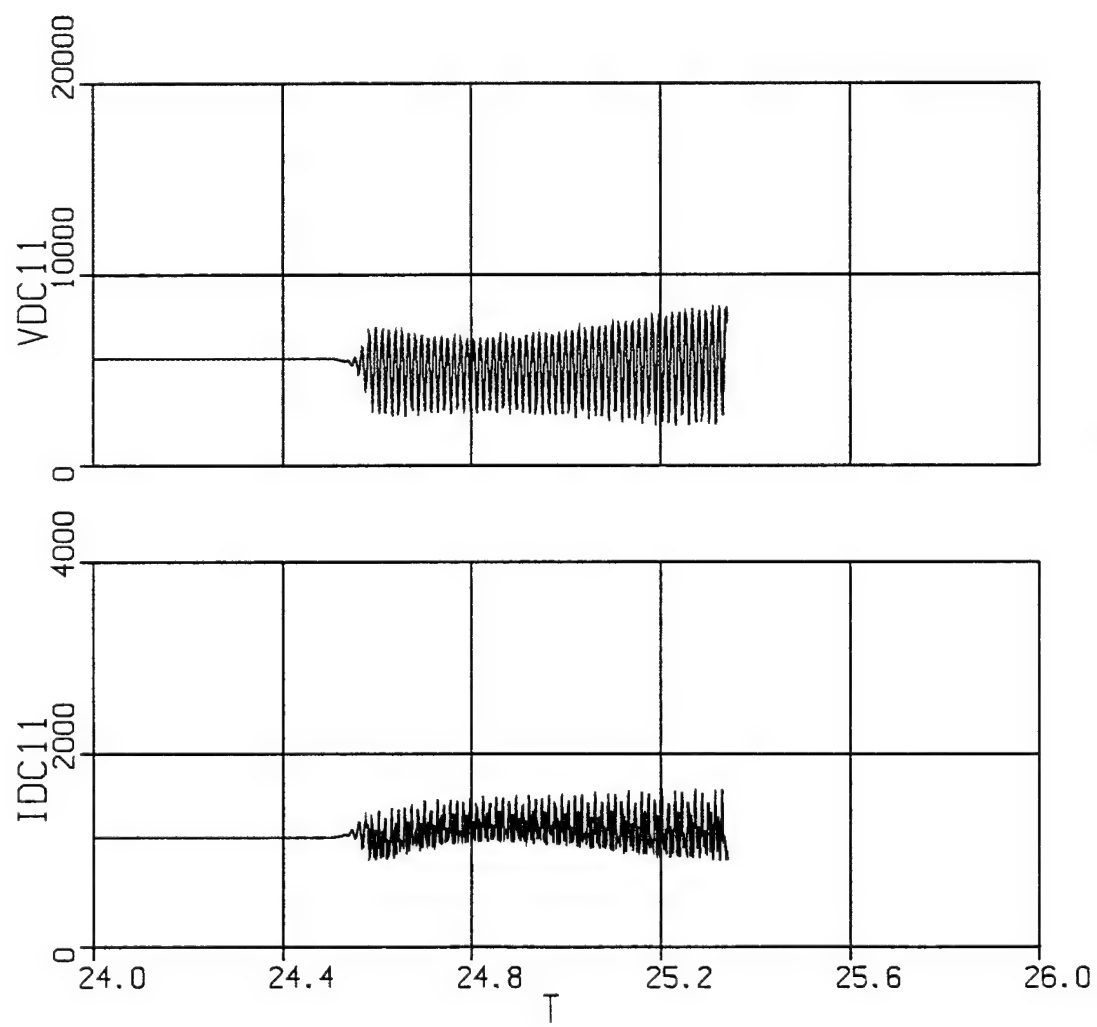
9 Jun 26 11:52:40 1996



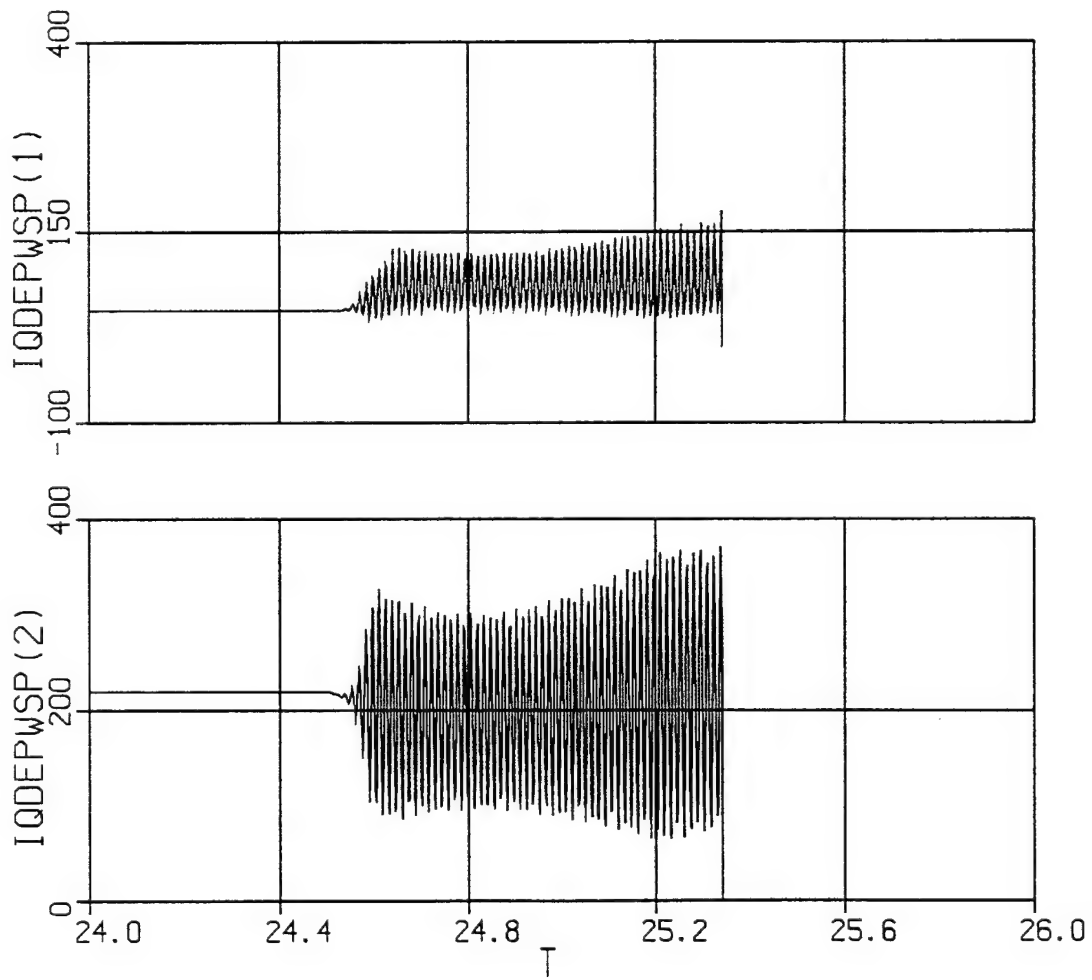
10 Jun 26 11:52:40 1996



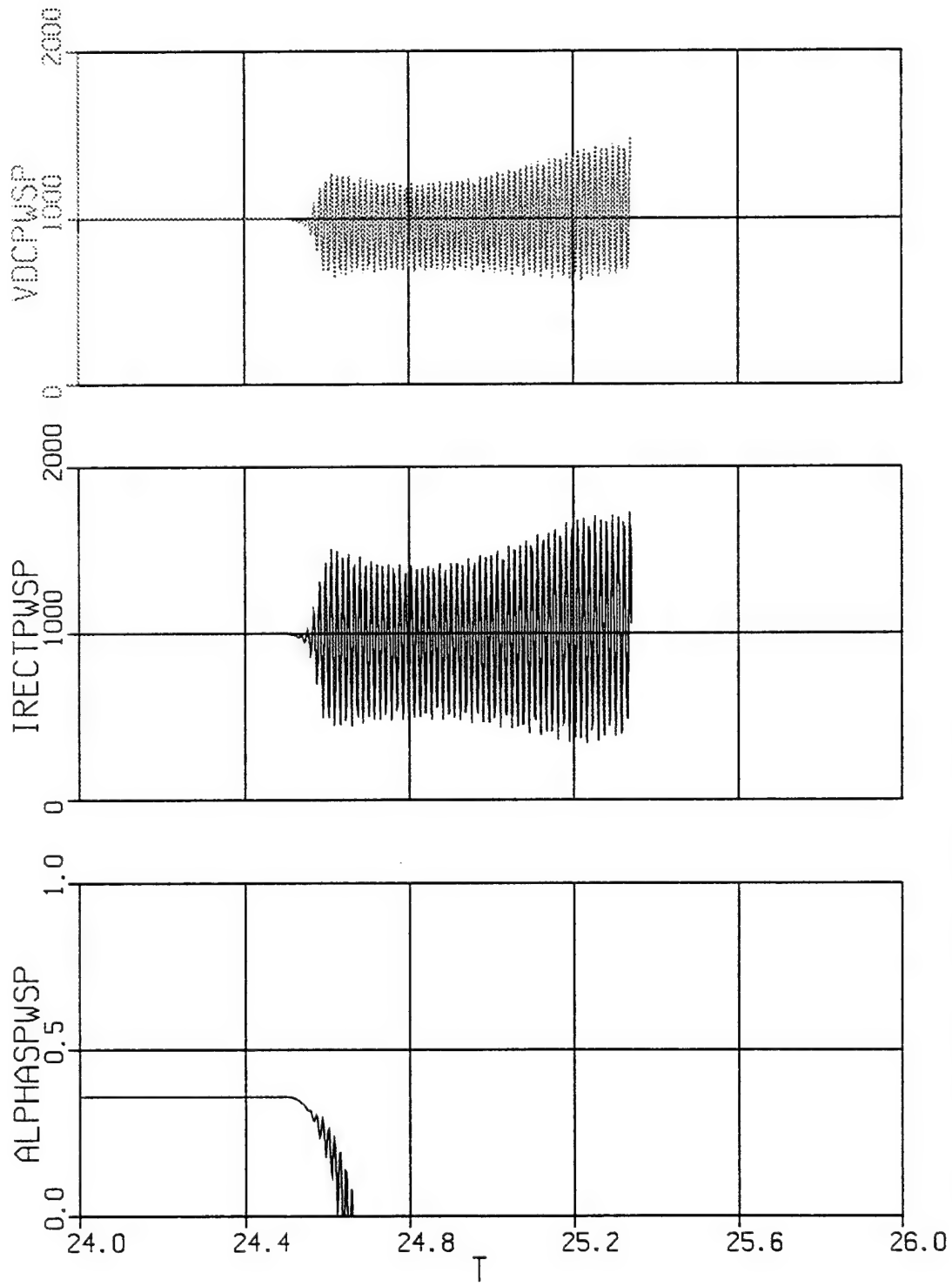
11 Jun 26 11:52:40 1996



12 Jun 26 11:52:40 1996

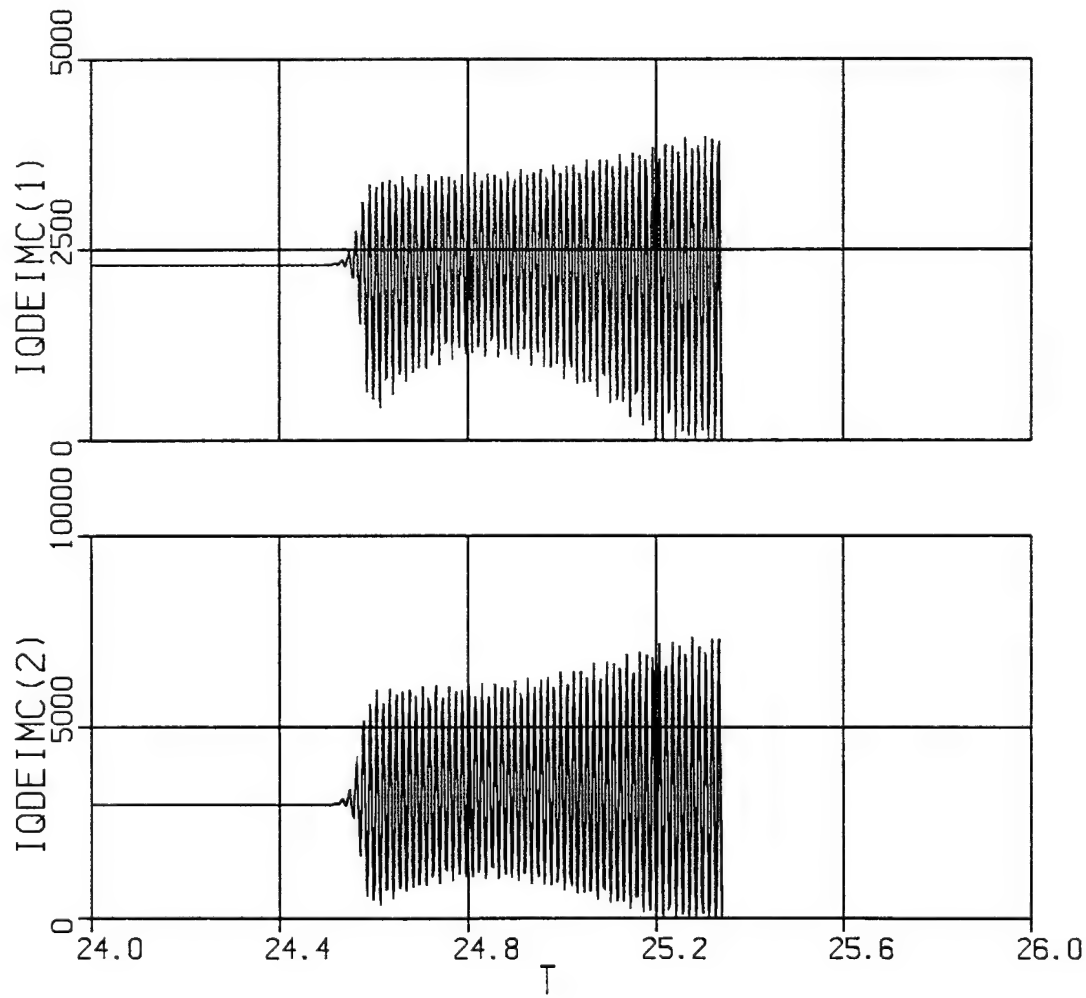


13 Jun 26 11:52:40 1996

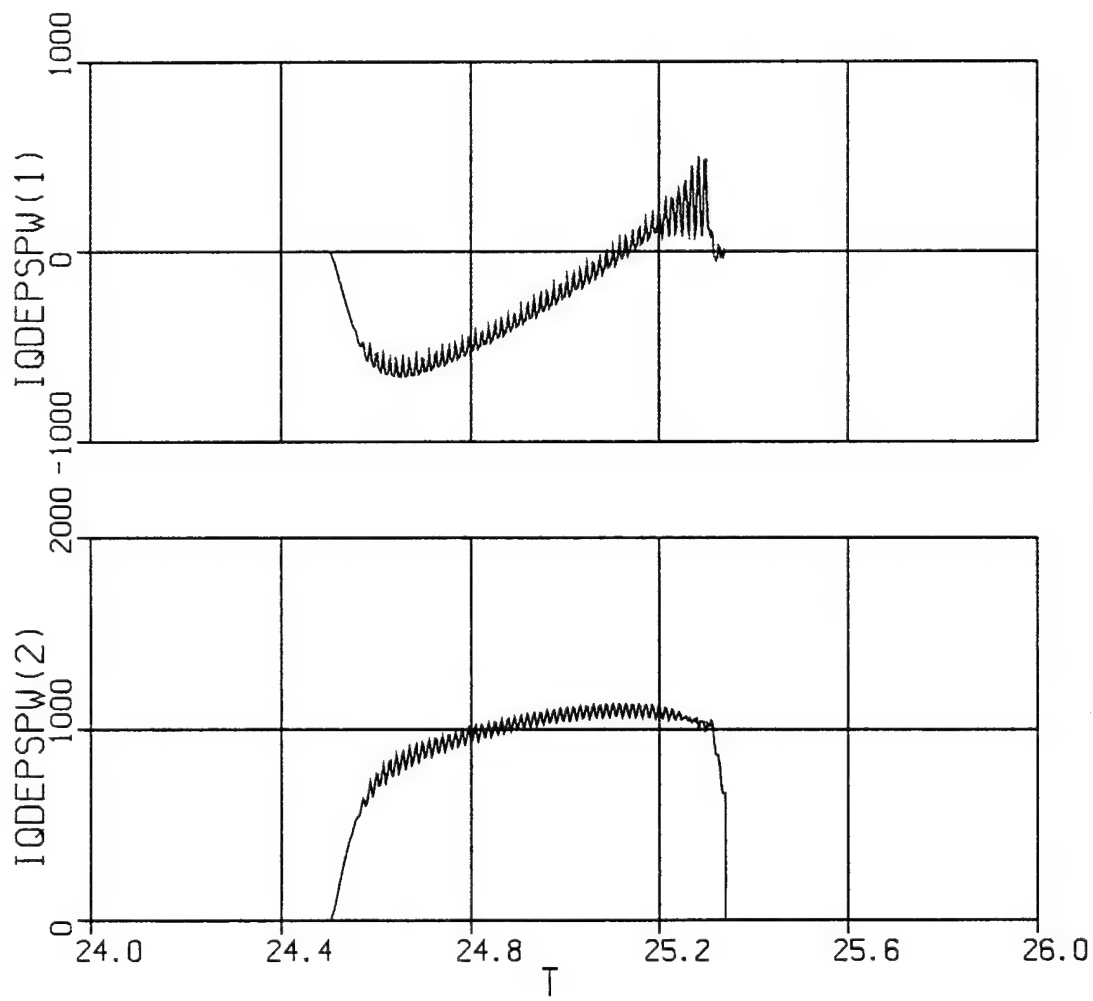


14 Jun 26 11:52:40 1996

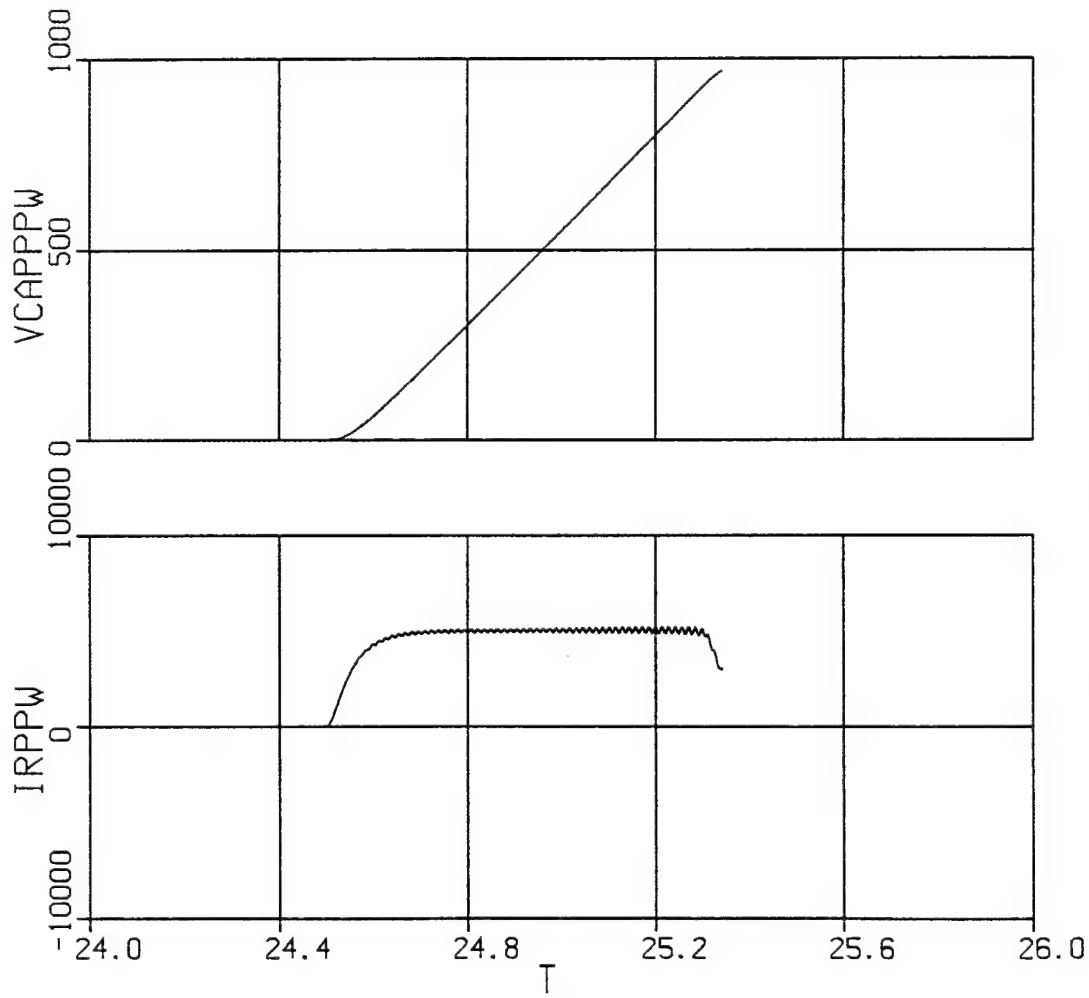




15 Jun 26 11:52:40 1996



16 Jun 26 11:52:40 1996



17 Jun 26 11:52:40 1996

## REFERENCES

- [1] "Automated State Model Generation Algorithm for Power Circuits and Systems," O. Wasynczuk and S. D. Sudhoff (to be published by IEEE)
- [2] "Integrated Power System Simulation Model Development - Modeling of an Induction Motor Based Integrated Propulsion System," PCKA, November 1995.
- [3] "Analysis of Electric Machines and Converters in Power and Drive Systems," P.C. Krause, O. Wasynczuk and S. D. Sudhoff, IEEE Press (being printed).
- [4] "Analysis and Average Value Modeling of Dual Line Commutated Converter Six Phase Synchronous Machine Systems," IEEE Transactions on Energy Conversion, September 1993, pp. 411-417.
- [5] "Modeling of Shipboard Electric Power Distribution System," PCKA, SBIR Phase II Final Report, September 1991, N615330-89-C-0062 for DTRC Annapolis, MD.

## APPENDICES

The following appendices would normally be included as sections of the report; however, each appendix is written in manuscript format for publication purposes. It was decided to include these manuscripts as part of the report and not to spend the time to rewrite this material in the format of the report.

Appendix A: DC Link Stabilized Field Oriented Control of Electric Propulsion Systems

Appendix B: Modeling Consideration in a 15-Phase Induction Motor Drive System

Appendix C: Control of a 15-Phase Induction Motor Drive System

## Appendix A

# DC Link Stabilized Field Oriented Control of Electric Propulsion Systems

**Abstract** - In the process of designing the controller for the induction motor drive included in this report, it was discovered that the system would exhibit negative impedance instability. Therefore, a simple though nonlinear control algorithm was created to mitigate this instability. As a first step in developing this control for the IPS system, the control was developed for a 3-phase induction motor based drive system. In particular, the 3-phase induction motor based version of the control was verified both through the use of computer simulation and by construction of a 3.7 kW prototype system using the laboratory facilities of the University of Missouri - Rolla. The design and performance of the 3-phase version of the control are set forth herein.

### I. INTRODUCTION

Electric propulsion systems consisting of a turbine driven synchronous machine feeding an induction motor drive through a rectifier - dc link - inverter frequency changer are important in a wide variety of applications including locomotives, hybrid electric vehicles, submarines, and ship propulsion systems, including the next generation warship, the Surface Combatant 21. The advantage of such a system over a mechanical transmission is that the turbine speed becomes fully decoupled from the load speed, allowing the turbine speed to be optimized with regard to fuel efficiency. In addition, the elimination of the mechanical linkage between the turbine or other prime mover and the mechanical load (drive train or propeller) allows a greater degree of architectural freedom in the locomotive / vehicle / ship layout. In many of these systems, the inverter is used to tightly regulate the motor current waveforms, which has the advantage of making the inverter / motor drive extremely robust with regard to overcurrents. However, at the same time, such regulation has the disadvantage that it makes the motor drive appear to have a negative impedance, since if the inverter voltage is reduced the dc link current will increase so as to maintain constant power (since the motor currents will remain undisturbed). This negative impedance can result in loss of dynamic stability of the propulsion system. In order to avoid instability, a classical method is to increase the dc link capacitance. However, in large drive systems, such as those used in naval applications, the capacitance required can become costly in terms of capital, space, and weight. In this paper, a nonlinear dc link stabilized field oriented control is demonstrated which is shown have performance characteristics similar to the classical field oriented control, but mitigates the negative impedance instability problem.

### II. SYSTEM OVERVIEW

Fig. 1 illustrates the type of electric propulsion system considered herein. The power source of this system is a diesel engine or turbine which serves as a prime mover for the 3-phase synchronous machine (SM). The 3-phase output of the machine is rectified using an uncontrolled rectifier. The rectifier output voltage is denoted  $v_r$ . An LC circuit serves as a filter, and the output of this filter is denoted  $v_{dcs}$ . A voltage regulator / exciter adjusts the field voltage of the synchronous machine in such a way that the source bus voltage  $v_{dcs}$  is equal to the commanded bus voltage  $v_{dcs}^*$ . The source bus is connected via a tie line to the load bus, the voltage at which is denoted  $v_{dci}$ . The load bus consists of a capacitive filter (which includes both electrolytic and polypropylene capacitance) as well as a 3-phase fully controlled inverter, which is in turn supplies an induction motor. The induction motor drives the mechanical load, which is rotating at a speed  $\omega_{m,im}$ . Based upon the mechanical rotor speed, and the desired electromagnetic torque  $T_{e,des}$  (which is determined by the controller governing the mechanical system), the induction motor controls specify the on/off status of each of the inverter semiconductors in such a way that the desired torque is obtained. Although this system is quite robust with regard to overcurrents, and simple to design from the viewpoint that the controller governing the mechanical system is decoupled from the control of the electrical system (since the torque can be controller nearly instantaneously), such systems are prone to be subject to a limit cycle behavior in the dc bus voltage known as negative impedance instability.

### III. CAUSE OF NEGATIVE IMPEDANCE INSTABILITY

In order to gain insight into the cause of negative impedance instability, it is appropriate to set forth a highly simplified model of the system depicted in Fig. 1. This model will focus on the dc bus dynamics and need only be valid in the tens to hundreds of hertz band. An appropriate model of the synchronous machine / rectifier and LC filter is illustrated in Fig. 2. Therein, the dynamics of both the prime mover and voltage regulator are neglected since these are subject to long time constants imposed by the prime mover inertia and synchronous machine field, respectively. The dc voltage behind inductance and resistance synchronous machine model is based on the work set forth in [1], which has been shown to have excellent bandwidth. In Fig. 2,

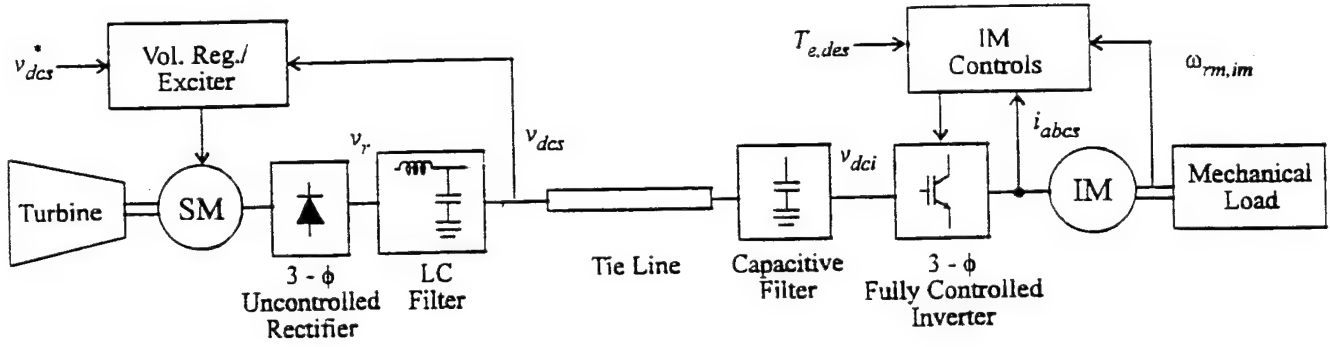


Figure 1. Electric propulsion system.

$$E = \omega_{r,sm} \sqrt{(\lambda_q'')^2 + (\lambda_d'')^2} \quad (1)$$

where  $\omega_{r,sm}$  is the electrical rotor speed of the synchronous machine and  $\lambda_q''$  and  $\lambda_d''$  are the q- and d-axis subtransient flux linkages,  $\alpha$  is the firing angle relative to the subtransient back emf,  $L_c(\beta)$  and  $L_t(\beta)$  are the commutating and transient commutating inductance's defined by

$$L_c(\beta) = \frac{1}{2}(L_q'' + L_d'') + (L_d'' - L_q'')\sin(2\beta + \frac{\pi}{6}) \quad (2)$$

and

$$L_t(\beta) = L_q'' + L_d'' + (L_d'' - L_q'')\sin(2\beta - \frac{\pi}{6}) \quad (3)$$

where  $\beta$  is the firing angle relative to rotor position and  $L_q''$  and  $L_d''$  are the synchronous machine q- and d-axis subtransient inductance's,  $r_{s,sm}$  is the synchronous machine stator resistance,  $L_f$  and  $r_f$  are the inductance and resistance of the LC filter inductor, and  $C_f$  is the capacitance of the LC filter capacitor.

A highly simplified model of the capacitive filter and induction motor is illustrated in Fig. 3. Therein, the drive is modeled as a dependent current source equal to the instantaneous power  $P$  divided by dc link voltage  $v_{dci}$  and

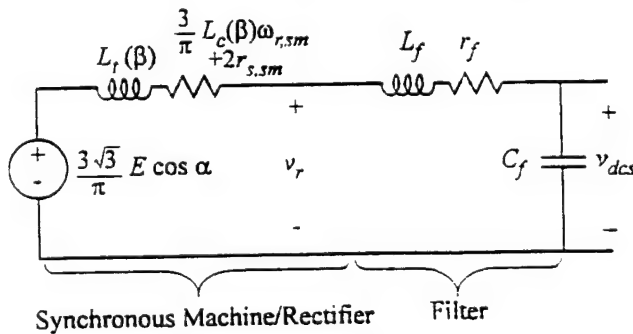


Figure 2. Simplified model of synchronous machine/rectifier and filter.

where it is assumed that the instantaneous power is equal to the instantaneous power command  $P^*$  defined as

$$P^* = \omega_{rm,im} T_e^* \quad (4)$$

In (4),  $T_e^*$  is an instantaneous torque command which is the input to the field oriented induction motor control. Typically, the instantaneous torque command  $T_e^*$  is set equal to the desired torque  $T_{e,des}$ . However, the control algorithm proposed in this paper will possess an alternate relationship.

Upon neglecting the tie line, which is generally short in an electrical sense for the frequency range of interest, the component models illustrated in Fig. 2. and Fig. 3. are combined as in Fig. 4. Therein,

$$L_e = L_t(\beta) + L_f \quad (5)$$

$$R_e = \frac{3}{\pi} L_c(\beta) \omega_{r,sm} + 2r_{s,sm} + r_f \quad (6)$$

$$C_e = C_f + C_i \quad (7)$$

$$v_{es} = \frac{3\sqrt{3}}{\pi} E \cos(\alpha) \quad (8)$$

In (5-8),  $\alpha$  and  $\beta$  can be found by steady-state analysis of the load commutated converter rectifier system as set forth in [2]. However, assuming the rectifier is uncontrolled the calculation may be made much simpler by neglecting subtransient saliency whereupon

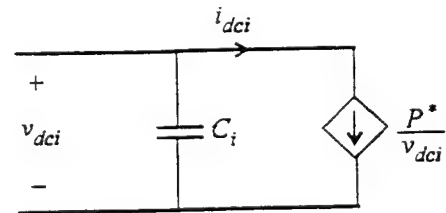


Figure 3. Simplified capacitive filter, induction motor drive model.

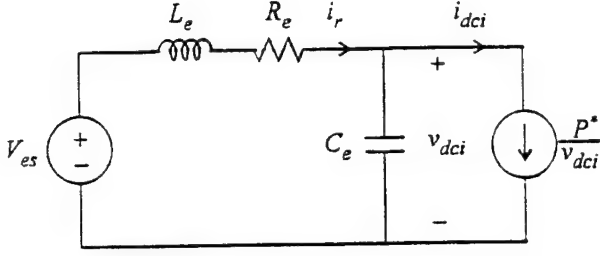


Figure 4. Highly simplified dc link model.

$$\alpha = 0 \quad (9)$$

and the commutating and transient commutating inductance's are no longer a function of  $\beta$ . Furthermore, due to the action of the voltage regulator, the subtransient inductance's will have a value such that

$$v_{es} = v_{es}^* \quad (10)$$

so that no subtransient information is actually needed. It should be cautioned that this model is intended for explanation purposes and for guidance in designing control algorithms, not for high-fidelity simulation or for the testing of control algorithms.

In order to utilize this equivalent circuit to predict negative impedance stability, note that linearizing the input current with respect to input voltage about an operating point wherein  $v_{dci}$  is equal to  $v_{dcs}$  yields

$$\Delta i_{dci} = -\frac{P^*}{v_{dcs}^2} \Delta v_{dci} \quad (11)$$

from which it is apparent that the inverter presents an input impedance of

$$Z_{inv} = -\frac{v_{dcs}^2}{P^*} \quad (12)$$

As can be seen, in a small signal sense the inverter appears to possess a negative impedance which, from an intuitive point of view, would seem to be destabilizing.

In order to verify this conclusion, replacing the dependent source representing the inverter with its small signal equivalent impedance, yields the following small signal model of the equivalent circuit

$$\frac{d}{dt} \begin{bmatrix} \Delta i_r \\ \Delta v_{dci} \end{bmatrix} = \begin{bmatrix} \frac{R_e}{L_e} & \frac{1}{L_e} \\ \frac{1}{C_e} & \frac{P^*}{v_{dcs}^2 C_e} \end{bmatrix} \begin{bmatrix} \Delta i_r \\ \Delta v_{dci} \end{bmatrix} + \begin{bmatrix} \frac{1}{L_e} \\ 0 \end{bmatrix} \Delta v_{es} \quad (13)$$

which has a characteristic equation of

$$\lambda^2 + \left( \frac{R_e}{L_e} - \frac{P^*}{C_e v_{dcs}^2} \right) \lambda + \left( \frac{1}{L_e C_e} - \frac{P^* R_e}{C_e L_e} \right) = 0 \quad (14)$$

From (14) it follows that necessary conditions for stability are that

$$\frac{v_{dcs}^2}{P^*} > R_e \quad (15)$$

and that

$$\frac{R_e}{L_e} > \frac{P^*}{C_e v_{dcs}^2} \quad (16)$$

Physically (15) is a steady state limit on the amount of power which can be transferred and is normally satisfied in practice. In the case of (16), it can be seen that a given system will eventually go unstable as the power command is increased. To avoid instability, one method is to simply increase  $C_e$  until the system is stable to the maximum possible power command. However, this has the disadvantage in that for very large drive systems the physical space, weight, and cost of this capacitance become issues, especially considering the fact that the applications are largely mobile in nature.

#### IV. LINK STABILIZING FIELD - ORIENTED CONTROL

In this section, an algorithm which improves the damping of the dc link by eliminating the negative impedance effect over a prescribed bandwidth is set forth. This algorithm is based upon the fact that torque control in a field oriented drive is nearly instantaneous. As mentioned previously, typically the instantaneous torque command  $T_e^*$  is set equal to the desired torque  $T_{e,des}$  as determined by the control algorithm governing the mechanical system. However, herein it is proposed to determine the instantaneous torque command as

$$T_e^* = \left( \frac{v_{dci}}{\tilde{v}_{dci}} \right)^n T_{e,des} \quad (16)$$

where  $v_{dci}$  is the filtered dc inverter voltage, i.e.,

$$\frac{d\tilde{v}_{dci}}{dt} = \frac{v_{dci} - \tilde{v}_{dci}}{\tau} \quad (17)$$

and the parameters  $n$  and  $\tau$  are considered to be constants herein but could also be made to be a function of operation point.

The advantage of this simple though nonlinear control algorithm is that it is extremely straightforward to implement yet highly effective in mitigating negative impedance instabilities. In order to illustrate the effect of the algorithm on the system note that using the control law input power into the inverter is given by

$$P = \left( \frac{v_{dci}}{\tilde{v}_{dci}} \right)^n P_{des} \quad (18)$$



where

$$P_{des} = T_{e,des} \omega_{rm} \quad (19)$$

From (18) the input current may be expressed

$$i_{dci} = \frac{v_{dci}^{n-1}}{\tilde{v}_{dci}^n} P_{des} \quad (20)$$

Linearizing (20) about the desired operating point ( $v_{dci} = v_{dcs}^*$ ) yields

$$Z_{inv} = \frac{1}{n-1} \frac{v_{dcs}^{*2}}{P_{des}} \quad (21)$$

If  $\tau$  so great as to not interact with the dc link dynamics and  $n$  is selected to be unity then the input impedance presented by the inverter is infinite over the frequency range over which negative impedance instabilities occur, thus avoiding this type of instability.

Although the explanation of the previous paragraph illustrates the basic philosophy of the control, the possibilities of the control are much richer than is indicated therein. In particular, by suitable selection of  $\tau$  and  $n$  a large variety of behaviors can be obtained. In order to see this it is helpful to first set forth the nonlinear differential equation governing the dc link dynamics in the presence of the new control. In particular,

$$\frac{d}{dt} \begin{bmatrix} i_r \\ v_{dci} \\ \tilde{v}_{dci} \end{bmatrix} = \begin{bmatrix} -\frac{R_e}{L_e} & -\frac{1}{L_e} & 0 \\ \frac{1}{C_e} & 0 & 0 \\ 0 & \frac{1}{\tau} & -\frac{1}{\tau} \end{bmatrix} \begin{bmatrix} i_r \\ v_{dci} \\ \tilde{v}_{dci} \end{bmatrix} + \begin{bmatrix} 0 \\ \frac{P_{des}}{v_{dci}} \left( \frac{v_{dci}}{\tilde{v}_{dci}} \right)^n \\ 0 \end{bmatrix} + \frac{1}{L_e} \begin{bmatrix} 1 & 0 & 0 \end{bmatrix}^T v_{es} \quad (22)$$

Linearization of (22) yields

$$\frac{d}{dt} \begin{bmatrix} \Delta i_r \\ \Delta v_{dci} \\ \Delta \tilde{v}_{dci} \end{bmatrix} = \begin{bmatrix} -\frac{R_e}{L_e} & -\frac{1}{L_e} & 0 \\ \frac{1}{C_e} & (n-1) \frac{P_{des}}{v_{dci}^{n+1}} & -n \frac{P_{des}}{v_{dci}^{n+1}} \\ 0 & \frac{1}{\tau} & -\frac{1}{\tau} \end{bmatrix} \begin{bmatrix} \Delta i_r \\ \Delta v_{dci} \\ \Delta \tilde{v}_{dci} \end{bmatrix} + \frac{1}{L_e} \begin{bmatrix} 1 & 0 & 0 \end{bmatrix}^T \Delta v_{es} \quad (23)$$

In order to illustrate the effects of varying  $n$  and  $\tau$ , consider the case of a system in which  $v_{es}^* = 400$  V,  $R_e = 4.58 \Omega$ ,  $L_e = 13.9$  mH, and  $C_e = 51.4 \mu\text{F}$ . These parameters correspond to a test system which was used for laboratory demonstration. Fig. 5 illustrates the root loci of the characteristic equation as  $\tau$  is varied from 0.1 ms to 1 s (24) for  $n=1, 3, 5$ , and 7 (It should be noted that  $n$  does not have to be an integer). As can be seen, in each case the root locus contains an unstable complex pole (denoted A and A\*) for small values of  $\tau$  which becomes stable as  $\tau$  is increased. For all  $n$  shown in Fig. 5 the real part of the eigenvalues

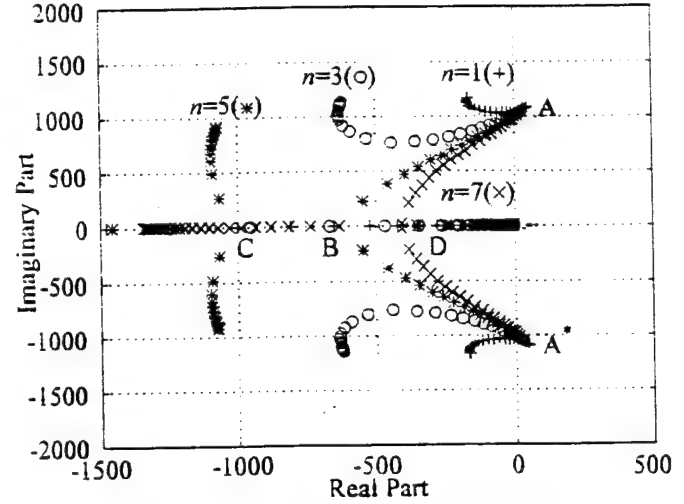


Figure 5. Root Locus as  $\tau$  and  $n$  are varied.

becomes more negative as  $\tau$  is increased. In addition, initially the complex part also decreases. In the case of  $n=5$  eventually the complex pair becomes real (point B) and then one of these real roots meets the root corresponding to the filter at point C, at which this pair of eigenvalues becomes complex. In the case of  $n=7$  the two complex poles eventually become real at point D; after which the pair moves away from each other on the real axis.

Fig. 6 illustrates the damping of the complex pole pair as  $n$  and  $\tau$  are varied. Note that for each value of  $n$  there is a value of  $\tau$  which maximizes the damping. It is also apparent that, generally speaking, as  $n$  is increased the damping can be increased.

Since the control law is nonlinear, it will of course be a function of operating point, and so it is important to investigate the performance of the control as the operating

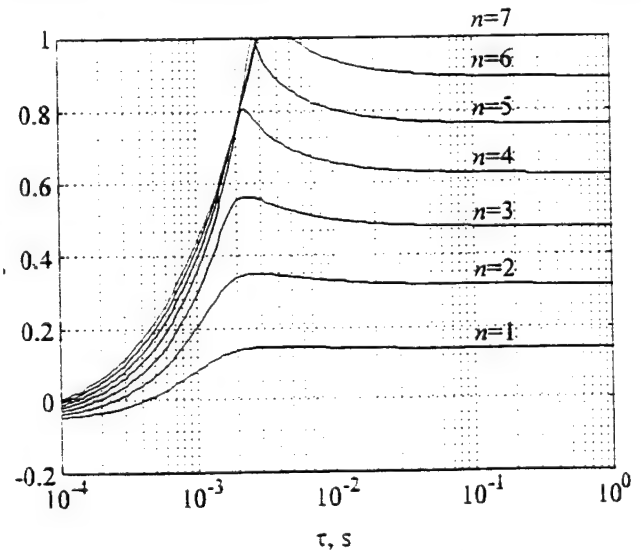


Figure 6. Damping factor versus  $\tau$  and  $n$ .

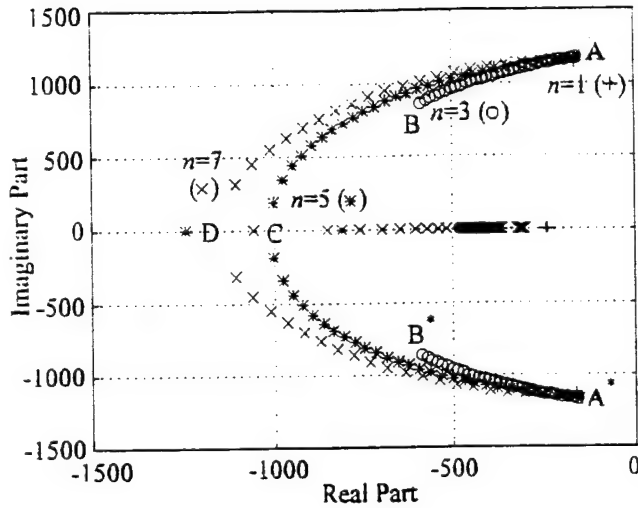


Figure 7. Root locus versus  $P^*$  and  $n$ .

point (primarily through power command) is varied. Fig. 7 illustrates the root locus of the system as power command is varied with  $(n=1, \tau=4 \text{ ms})$ ,  $(n=3, \tau=2.4 \text{ ms})$ ,  $(n=5, \tau=2.7 \text{ ms})$ , and  $(n=7, \tau=3.1 \text{ ms})$ . In each case  $\tau$  was selected so as to maximize the damping factor of the complex pole pair. As can be seen from Fig. 7, at low power the complex eigenvalue of the system is at point  $(A, A^*)$  regardless of  $n$ . In the case of  $(n=1)$ , the location of the roots is power level independent. However, in the case of  $n=3$  the complex pair moves to  $(B, B^*)$ . Finally, in the case of  $n=5$ , and  $n=7$ , the complex eigenvalues become real at point C and D, respectively. This illustrates an important feature of the proposed control law which is that although with the standard control  $(n=0)$  the system becomes less stable as power level increases with the proposed control law the system actually becomes more stable as power level increases, with the exception of  $(n=1)$  in which case the eigenvalues associated with the dc link become largely operating point invariant.

## V. IMPLEMENTATION

Before setting forth the implantation of the proposed controller, it is appropriate to first consider a standard field oriented control such as the rotor flux indirect field oriented control illustrated in Fig. 8 (note that the control proposed in this paper, is, however, independent of whether or not the field oriented control is direct or indirect). Therein, an instantaneous torque command  $T_e^*$  is the input to the controller. This torque command is equal to the torque desired by the controller governing the mechanical dynamics,  $T_{e,des}$ . As can be seen, based on the torque command  $T_e^*$  and desired d-axis rotor flux level  $\lambda_{dr}^{e*}$ , the desired q- and d- axis stator currents,  $i_{qs}^{e*}$  and  $i_{ds}^{e*}$ , are determined. This calculation is a function of the induction

motor rotor magnetizing inductance  $L_m$ , the induction motor rotor inductance (rotor leakage plus magnetizing)  $L_r'$ , the rotor resistance  $r_r'$ , and the number of poles,  $N_{p,im}$ . Based on the q- and d- axis stator currents the electrical radian slip frequency,  $\omega_{s,im}$ , is determined, which is then added to the electrical rotor speed  $\omega_{r,im}$  in order to determine the electrical speed of the synchronous reference frame  $\omega_{e,im}$ , which is integrated in order to determine the position of the synchronous reference frame  $\theta_{e,im}$ . In addition to the algorithm illustrated in Fig. 8, especially in large drives, the field oriented control will often include on line parameter identification algorithm to compensate for variations of the rotor time constant.

Once the q- and d-axis current commands and the position of the synchronous reference frame are established, these currents may be synthesized in a variety of ways. Herein, the q- and d-axis current command was transformed back into a abc variable current command which is an input to a hysteresis type current control.

Incorporating the link stabilizing control into the field oriented control is quite straightforward. In particular, the only difference in the control is the instantaneous torque command is generated using (16) rather than being set equal to the desired torque, as is illustrated in Fig. 9.

## VI. EXPERIMENTAL SETUP

In order to illustrate the experimental set up a system such as the one depicted in Fig. 1 was constructed at a low (3.7 kW) power level. The prime mover was a dynamometer in speed control mode. The parameters of the 3.7 kW synchronous machine are listed in Table 1. Therein, all rotor parameters have been referred to the stator by the appropriate turns ratio. A solid state exciter voltage regulator was used to control the dc link voltage; a block diagram of

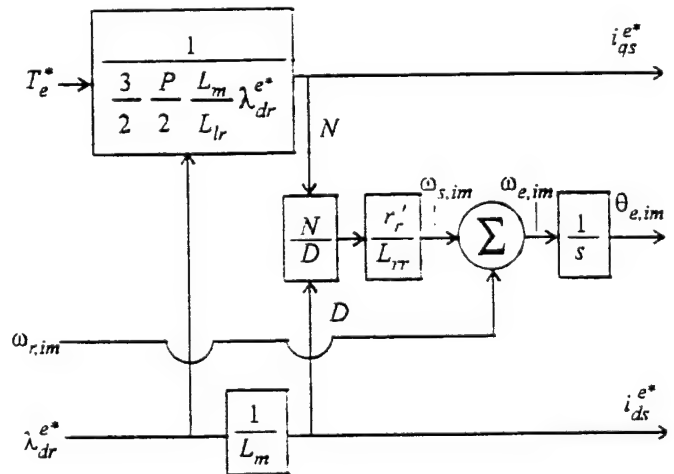


Figure 8. Rotor Flux Oriented Indirect Field Oriented Control.

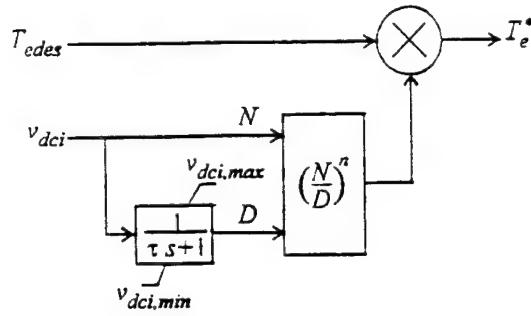


Figure 9. DC link stabilizing control.

this control appears in Fig. 10. The LC filter, transmission line, and inverter capacitance parameters are listed in Table 2. Finally, a 3.7 kW induction motor was used as a load. Induction motor parameters are listed in Table 3. The induction motor control was implemented based on the indirect rotor flux strategy, and the current command was synthesized using hysteresis current control with a hysteresis band of 0.95 A. The link stabilizing controller parameters were  $n = 1$ ,  $\tau = 4$  ms,  $v_{dcmin} = 200$  V, and  $v_{dcmax} = 600$  V.

Table 1. Synchronous machine parameters		
$r_{s,sm} = 382$ mW	$L_{ls} = 0.83$ mH	$P = 4$
$L_{mq} = 13.5$ mH	$L_{md} = 39.7$ mH	$n_{rfd} = 0.0271$
$r_{kd1} = 31.8$ $\Omega$	$L_{lkd1} = 6.13$ mH	$r_{fd} = 122$ mW
$r_{kd2} = 0.923$ $\Omega$	$L_{lkd2} = 3.4$ mH	$L_{lfd} = 2.54$ mH
$r_{kd1} = 40.47$ $\Omega$	$L_{lkd1} = 4.73$ mH	
$r_{kd2} = 1.31$ $\Omega$	$L_{lkd2} = 3.68$ mH	

## VII. VALIDATION

The performance of the link stabilizing field oriented control was validated using both a detailed (as opposed to average value / reduced order) computer simulation and in hardware. For the purposes of computer simulation, the synchronous machine and induction motor models used were those set forth in [3]. In the case of the salient pole synchronous machine, magnetic saturation was represented

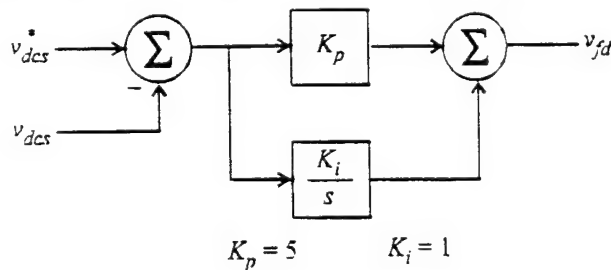


Figure 10. Voltage regulator/exciter.

Table 2. Passive component parameters.		
$L_f = 4.69$ mH	$r_f = 1.54$ $\Omega$	$C_f = 10.1$ $\mu$ F
$L_{line} = 28.8$ $\mu$ H	$r_{line} = 273$ m $\Omega$	$C_i = 41.3$ $\mu$ F

Table 3. Induction motor parameters.		
$r_s = 400$ m $\Omega$	$L_{ls} = 5.73$ mH	$L_m = 64.3$ mH
$r_r' = 227$ m $\Omega$	$L_{lr}' = 4.94$ mH	$P = 4$

in the d-axis. The simulation included the switching of each power electronics device. Semiconductor conduction losses were included, however switching losses were neglected.

Figure 11 illustrates the simulated performance of the system as the desired torque is changed from 2 to 19 Nm over a period of 100 ms. Variables depicted included the commanded a-phase current  $i_{as}^*$ , the actual a-phase current  $i_{as}$ , the dc inverter voltage  $v_{dci}$ , and the electromagnetic torque  $T_e$ . Although the actual torque closely tracks the desired torque, it can be seen that as the power command increases the dc bus voltage becomes unstable, stressing both the semi-conductors and the capacitors. In a typical system, such behavior could easily result in the semiconductor and/or capacitor failure. The experimental system has been constructed so as to be able to survive the overvoltages. Fig. 12 depicts the same study as measured in the laboratory. In Fig. 12, the instantaneous electromagnetic torque is not shown because suitable instrumentation was not available. As can be seen there is a reasonable correspondence between Fig. 11 and Fig. 12 with the exception that the actual system appears to be less stable than is predicted by the simulation. This is because the power requirements of the actual drive system are greater than the simulated system because of switching losses (It should be noted that the magnitude of the voltage swing increases very rapidly with power level). In addition, once a system becomes unstable it tends to be very sensitive to parameter variations.

Fig. 13 depicts the performance of the same system with the link stabilizing field oriented control as calculated using the computer simulation. As can be seen, according to the simulation the torque still closely tracks the commanded torque, however in this case there is no evidence of instability. Fig. 14 illustrates the system performance as measured in the laboratory. As predicted, the dc bus voltage is well behaved and the dc link bus voltage is stable.

One concern which may arise is a possible reduction in torque bandwidth since a drop in inverter voltage will result in a transient dip in torque. The detailed computer simulation was used to investigate this effect since the primary variable of interest was the electromagnetic torque. Fig. 15 depicts the predicted change of performance of the standard field oriented control as the torque command is stepped from 2 to 19 Nm. As can be seen, the electromagnetic torque reaches the commanded value in

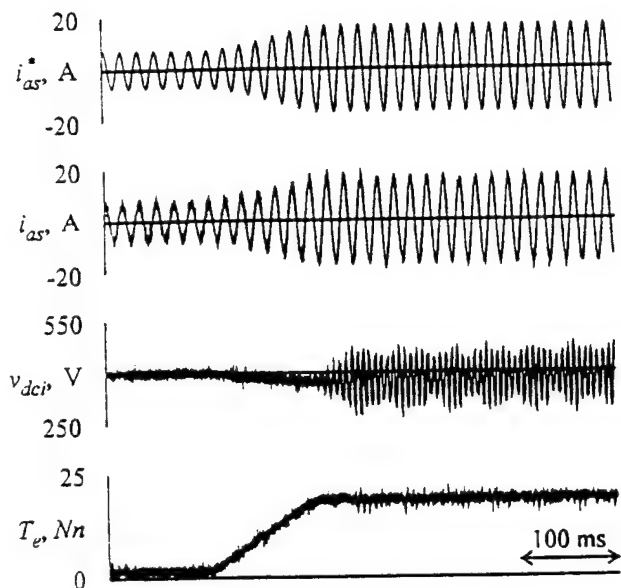


Figure 11. Simulated performance of standard field oriented control during ramp increase in desired torque.

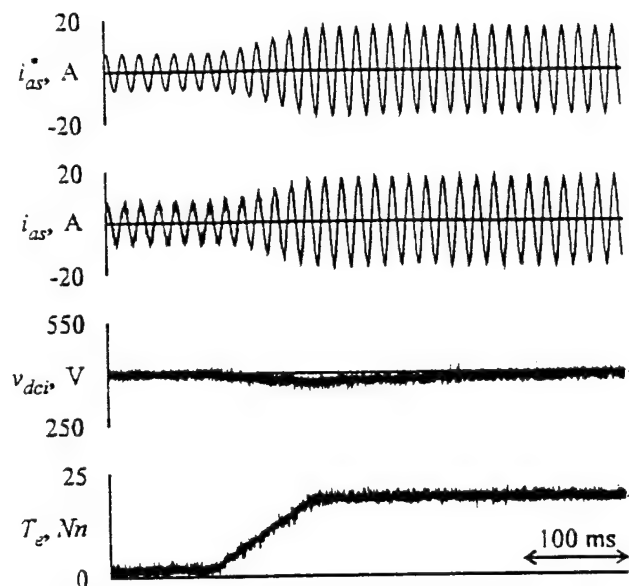


Figure 13. Simulated performance of link stabilized field oriented control during ramp increase in desired torque.

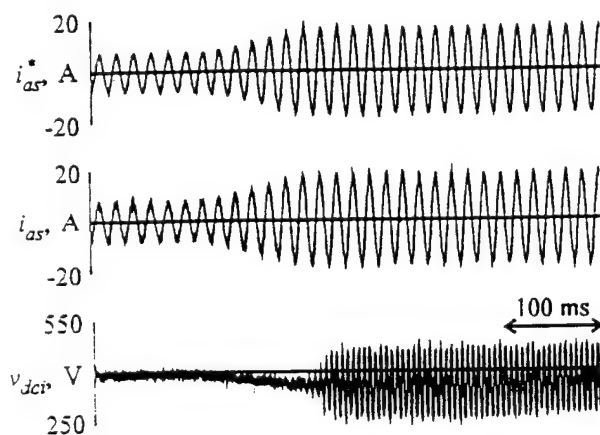


Figure 12. Measured performance of standard field oriented control during ramp increase in desired torque.

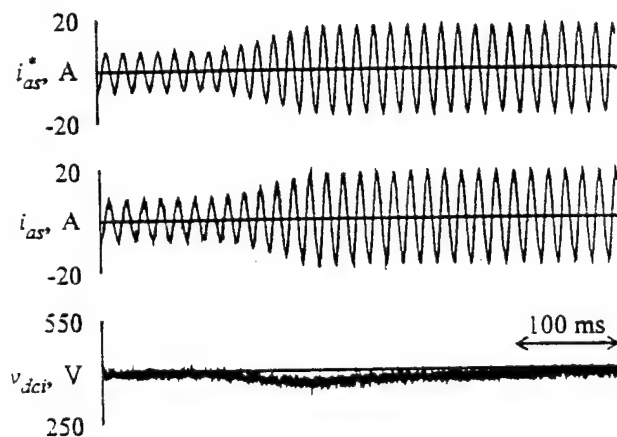


Figure 14. Measured performance of link stabilized field oriented control during ramp increase in desired torque.

approximately 5 ms. The torque response is not instantaneous due to the fact that a step change in current cannot be achieved in practice and because the dip in link voltage causes a temporary loss of current tracking in the hysteresis current control. Fig. 16 depicts the response of the link stabilized field oriented control. In this case, the electromagnetic torque reaches the commanded value in the order of 8 ms. Although the link stabilized control is somewhat slower than the standard field oriented control, this slight reduction in bandwidth is not a significant disadvantage in view of the improved dc bus voltage. This is particularly true in the fact that most propulsion systems

have mechanical inertia such that in either case the torque response may be considered to be instantaneous.

## VIII. CONCLUSIONS

A straightforward but nonlinear control algorithm has been set forth which can be used to mitigate negative impedance instabilities. The effectiveness of the control has been demonstrated both through the use of computer simulation and in the laboratory, and found to be highly effective in eliminating negative impedance instability. The primary disadvantage of the control is a slightly slower torque response. In addition to being applicable to induction

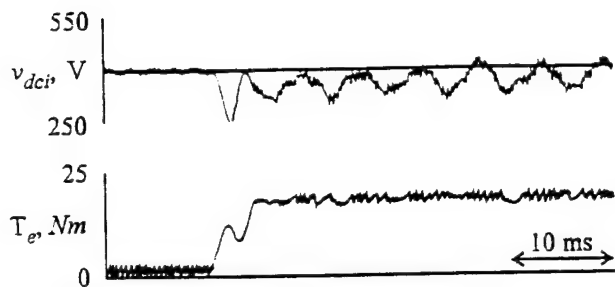


Figure 15. Simulated performance of standard field oriented control during step change in desired torque.

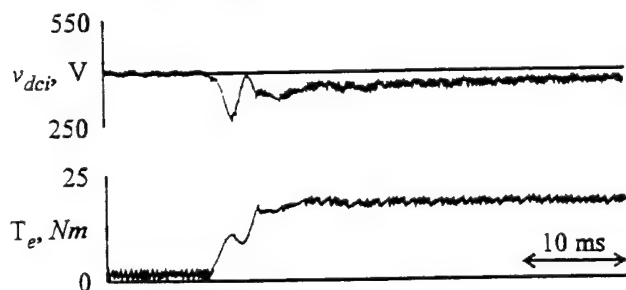


Figure 16. Simulated performance of link stabilized field oriented control during step change in desired torque.

motor drives, the control algorithm could also be used with other types of machines in which rapid torque control is possible, most notably permanent magnet synchronous machines.

#### IX. REFERENCES

- [1] S.D. Sudhoff, K.A. Corzine, H.J. Hegner, D.E. Delisle, "Transient and Dynamic Average-Value Modeling of Synchronous Machine Fed Load-Commutated Converters," accepted for *IEEE Trans. on EC*.
- [2] S.D. Sudhoff, O. Wasynczuk, "Analysis and Average-Value Modeling of Line-Commutated Converter - Synchronous Machine Systems," *IEEE Trans. on EC*, Vol. 8, No. 1, March 1993, pp. 92-99.
- [3] P.C. Krause, *Analysis of Electric Machinery*, McGraw Hill, 1986.

## Appendix B

### Modeling Consideration in a 15-Phase Induction Motor Drive System

#### I. INTRODUCTION

This analytical work set forth herein is the basis of both the detailed and average value models used in this SBIR Phase I effort. The work has been documented in journal format so that it may be published in the technical literature at a future date.

#### II. SYSTEM DESCRIPTION

Fig. 1 illustrates the inverter topology of the 15-phase induction motor drive system which is the subject of this analysis. As can be seen, the inverter is comprised of three dc rails, each of which is connected to five H-bridge inverters. These inverters are designated  $H_i$  where the  $i$ 'th H-bridge supplies the  $i$ 'th phase of the machine. The phases of the machine are in turn labeled such that the fundamental component of the  $i$ 'th phase is displaced  $(i-1)24^\circ$  (electrical) from the 1st phase.

The voltage vector  $v_{dc}$  will be used to designate the individual rail voltages, i.e.,

$$v_{dc} = [v_{dc1} \ v_{dc2} \ v_{dc3}]^T \quad (1)$$

and similarly the current vector  $i_{dc}$  will be used to designate the dc link currents

$$i_{dc} = [i_{dc1} \ i_{dc2} \ i_{dc3}]^T \quad (2)$$

The configuration of each H-bridge is illustrated in Fig. 2. Therein each semiconductor actually represents a number of devices in series, as necessary to achieve the required voltage blocking capability, and  $D_1$  through  $D_4$  designate the on/off status of each of the active semiconductors of the  $i$ 'th bridge, and  $v_{s_i}$ ,  $i_{s_i}$ , and  $i_{dch_i}$  denote the  $i$ 'th phase voltage, the  $i$ 'th phase current (defined positive into the machine), and the dc link current into the  $i$ 'th H-bridge, respectively. The switching state of the  $i$ 'th H-bridge is defined as

$$s_i = \begin{cases} 1 & D_1, \text{ and } D_4, \text{ on} \\ 0 & (D_1, \text{ on and } D_2, \text{ on}) \text{ or } (D_2, \text{ on and } D_4, \text{ on}) \\ -1 & D_2, \text{ and } D_3, \text{ on} \end{cases} \quad (3)$$

and  $s$  will denote the vector of switching states.

The drive system under consideration will be controlled using the field-oriented principal. The current command will be achieved using a current control algorithm that

regulates the current through a voltage command rather than by a direct method such as hysteresis current control. The focus of this work is on the basic model of the machine and inverter. Therefore, the discussion will concentrate on the representation of only the innermost control loop, which is based on the sine-triangle modulation strategy in which a sinusoidal duty cycle reference is compared to a triangle modulation waveform, as illustrated in Fig. 3. The switching signal for the  $i$ 'th phase is then synthesized as

$$s_i = \begin{cases} 1 & \text{if } s_i^* > d_i \\ -1 & \text{if } s_i^* \leq d_i \end{cases} \quad (4)$$

The zero state is not being used in order to reduce common mode link currents.

#### III. MACHINE VARIABLE INDUCTION MACHINE MODEL

The machine variable induction motor consists of the stator and rotor voltage equations, the flux linkage equations, and the torque equation. The stator and rotor voltage equations of a symmetrical N-phase induction machine may be expressed as

$$v_s = r_s i_s + \frac{d\lambda_s}{dt} \quad (5)$$

and

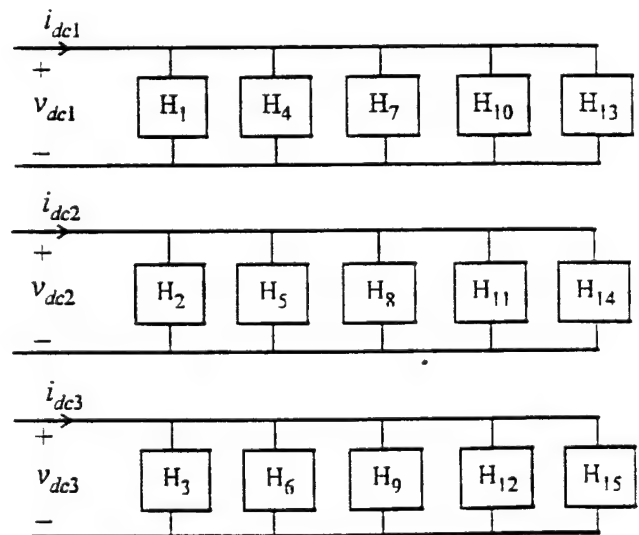


Figure 1. Drive topology.

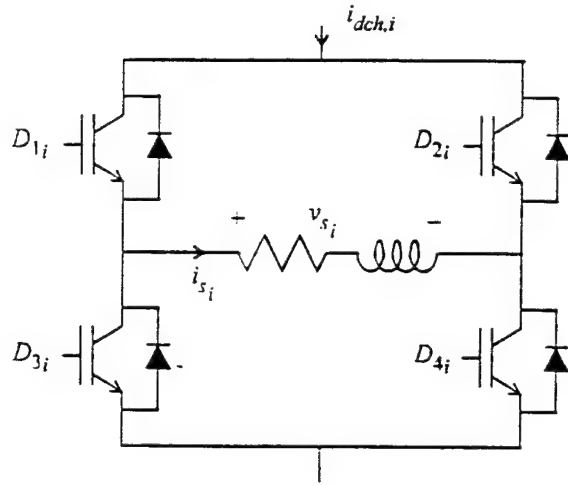


Figure 2. H-bridge.

$$v_r = r_r i_r + \frac{d\Lambda_r}{dt} \quad (6)$$

respectively, wherein

$$f_s = [f_{1s} \ f_{2s} \ \dots \ f_{Ns}]^T \quad (7)$$

and

$$f_r = [f_{ar} \ f_{br}]^T \quad (8)$$

where  $f$  can be a voltage  $v$ , flux linkage  $\Lambda$ , or current  $i$ . As can be seen, the distributed rotor circuits (which are physically implemented with a squirrel cage type construction) are represented on a 2-phase basis regardless of the number of stator phases.

Upon neglecting the effects of magnetic saturation and space harmonics, the stator and rotor flux linkage equation may be expressed

$$\Lambda_s = L_{ss} i_s + L_{sr} i_r \quad (9)$$

$$\Lambda_r = L_{sr}^T i_s + L_{rr} i_r \quad (10)$$

In (9), the stator self-inductance matrix is given by

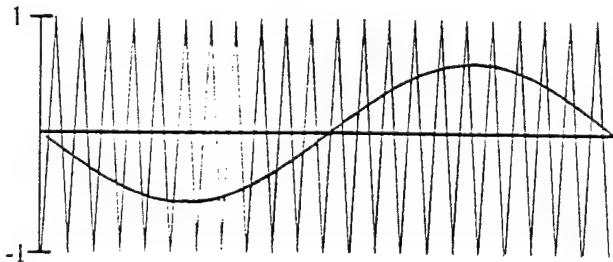


Figure 3. Sine-triangle modulation signals  $d_i$  and  $t_i$ .

$$L_{ss} = L_{ls} I_N + L_{ms} C_{ss} \quad (11)$$

where  $L_{ls}$  is the stator leakage inductance,  $I_N$  is an  $N$  by  $N$  identity matrix,  $L_{ms}$  is the stator magnetizing inductance, and  $C_{ss}$  is a  $N$  by  $N$  matrix whose elements are given by

$$C_{ss,j} = \cos((j-i)\frac{2\pi}{N}) \quad (12)$$

The stator-to-rotor self inductance matrix  $L_{sr}$  may be expressed

$$L_{sr} = L_{sr} \begin{bmatrix} C_{sr} & -S_{sr} \end{bmatrix} \quad (13)$$

In (13), the elements of  $C_{sr}$  and  $S_{sr}$  are defined by

$$C_{sr,i} = \cos(\theta_r - (i-1)\frac{2\pi}{N}) \quad (14)$$

and

$$S_{sr,i} = \sin(\theta_r - (i-1)\frac{2\pi}{N}) \quad (15)$$

respectively,  $L_{sr}$  denotes the maximum mutual inductance between any stator and any effective rotor winding, and  $\theta_r$  is the electrical rotor position, defined as  $P/2$  times the mechanical rotor position,  $\theta_{rm}$ , where  $P$  is the number of poles.

In (10), the rotor self inductance is of the form

$$L_{rr} = (L_{lr} + L_{mr}) I_2 \quad (16)$$

where  $L_{lr}$  and  $L_{mr}$  are the rotor leakage and magnetizing inductances, respectively.

From the flux linkage equations, the expression for electromagnetic torque is readily established using coenergy techniques. In particular, in terms of machine variables

$$T_e = \frac{P}{2} L_{sr} i_s^T \begin{bmatrix} -S_{sr}^T & -C_{sr} \end{bmatrix} i_r \quad (17)$$

It should be noted that  $L_{ms}$ ,  $L_{mr}$ , and  $L_{sr}$  are not independent because they share the same magnetizing path. In particular,

$$L_{ms} = \frac{n_s^2}{R_m} \quad (18)$$

$$L_{mr} = \frac{n_r^2}{R_m} \quad (19)$$

$$L_{sr} = \frac{n_s n_r}{R_m} \quad (20)$$

where  $n_s$  and  $n_r$  are the effective number of turns of the stator and rotor windings, respectively, and  $R_m$  denotes the reluctance of the magnetizing path.



#### IV. REFERRED MACHINE VARIABLE MODEL

The next step in deriving the qd model for the induction motor is to refer the rotor variables to the stator by the appropriate turns ratio. In particular, it is convenient to define the referred rotor voltage and flux linkage as

$$v_r' = \frac{n_s}{n_r} v_r \quad (21)$$

$$\Lambda_r' = \frac{n_s}{n_r} \Lambda_r \quad (22)$$

The referred rotor current is defined as

$$i_r' = \frac{2}{m} \frac{n_r}{n_s} i_r \quad (23)$$

where  $m$  is an integer which is dependent upon the construction the qd transformation (this will be discussed in a following section).

In terms of referred variables, the voltage equations become

$$v_s = r_s i_s + \frac{d\Lambda_s}{dt} \quad (24)$$

$$v_r' = r_r' i_r' + \frac{d\Lambda_r'}{dt} \quad (25)$$

where the referred rotor resistance given by

$$r_r' = \frac{m}{2} \left( \frac{n_s}{n_r} \right)^2 r_r \quad (26)$$

The referred flux linkage equations are given by

$$\Lambda_s = L_{ss} i_s + L_{sr}' i_r' \quad (27)$$

$$\Lambda_r' = L_{sr}^T i_s + L_{rr}' i_r' \quad (28)$$

In (25)

$$L_{sr}' = \frac{m}{2} L_{ms} \begin{bmatrix} C_{sr} & -S_{sr} \end{bmatrix} \quad (29)$$

and

$$L_{rr}' = (L_{lr}' + \frac{m}{2} L_{ms}) I_2 \quad (30)$$

where

$$L_{lr}' = \frac{m}{2} \left( \frac{n_s}{n_r} \right)^2 L_{lr} \quad (31)$$

#### V. QD TRANSFORMATIONS

The transformation of the referred machine variable model to a qd model has several advantages. First of all, in the case of detailed computer simulation, such a transformation eliminates rotor position dependence in the flux linkage equations so that the inverse inductance matrix only has to be computed once in the event that flux linkages are used as state variables. By choosing the stationary reference frame, the reference frame transformation and its

inverse are also constant matrices which further promotes computationally efficiency. In the case of average-value modeling, selection of a synchronous reference frame is most convenient, as such a formulation will result in state variables which are constant in the steady-state. Such a description is readily linearized. Furthermore, if the dynamics of the system in which the drive is placed are stiff, a model in which the state-variables are constant in the steady-state may be very efficiently solved using Gear's method.

However, beyond the choice of reference frame for detailed and average-value model, in the case of drive systems with a large number of phases the construction of the qd transformation, which is not unique, becomes an issue. For example, for the 15-phase system considered herein, the transformation could be made with a single q- and d-axis and 13 zero sequence variables, two q- and d-axis with 11 zero sequence variables, etc. As it turns out, two particularly interesting choices are the use of five sets of q- and d-axis with five zero sequence variables, and three sets of q- and d-axis with nine zero sequence variables, which correspond to the partitioning the machine into five 3-phase sets and three 5-phase sets, respectively.

The construction of a qd transformation based on five 3-phase sets is straightforward to construct because on a 3-phase set basis it is identical to the classical 3-phase qd transformation. In this case the transformation is constructed by dividing the fifteen phases into five 3-phase sets and arranging the elements of the conventional 3-phase qd transformation accordingly. In particular, the stator and rotor transformations may be expressed as

$$f_{qds} = K_s f_s \quad (32)$$

and

$$f_{qdr} = K_r f_r' \quad (33)$$

respectively. In (32)

$$f_{qds} = \begin{bmatrix} f_{qds1} & f_{qds2} & f_{qds3} & f_{qds4} & f_{qds5} \end{bmatrix}^T \quad (34)$$

where

$$f_{qds1} = \begin{bmatrix} f_{qs1} & f_{ds1} & f_{0s1} \end{bmatrix}^T \quad (35)$$

In (33)

$$f_{qdr} = \begin{bmatrix} f_{qr} & f_{dr} \end{bmatrix}^T \quad (36)$$

The stator transformation matrix is given by

$$K_s = \begin{bmatrix} K_{s11} & \cdots & K_{s13} \\ \vdots & & \vdots \\ K_{s51} & \cdots & K_{s53} \end{bmatrix} \quad (37)$$



where all the elements of  $\mathbf{K}_{sij}$  are zero except for the for the following:

$$(\mathbf{K}_{sij})_{1,i} = \frac{2}{3} \cos(\theta - (5(j-1) + i - 1) \frac{2\pi}{15}) \quad (38)$$

$$(\mathbf{K}_{sij})_{2,i} = \frac{2}{3} \sin(\theta - (5(j-1) + i - 1) \frac{2\pi}{15}) \quad (39)$$

$$(\mathbf{K}_{sij})_{3,j} = \frac{1}{3} \quad (40)$$

where  $\theta$  is the position of the arbitrary reference frame. The rotor transformation matrix is given by

$$\mathbf{K}_r = \begin{bmatrix} \cos(\theta - \theta_r) & \sin(\theta - \theta_r) \\ \sin(\theta - \theta_r) & -\cos(\theta - \theta_r) \end{bmatrix} \quad (41)$$

Transformation of the stator and referred rotor voltage equations (with  $m=3$ ) yields

$$v_{qs1} = r_s i_{qs1} + \omega \lambda_{ds1} + \frac{d\lambda_{qs1}}{dt} \quad (42)$$

$$v_{ds1} = r_s i_{ds1} + \omega \lambda_{qs1} + \frac{d\lambda_{ds1}}{dt} \quad (43)$$

$$v_{0s1} = r_s i_{0s1} + \frac{d\lambda_{0s1}}{dt} \quad (44)$$

and

$$v_{qr} = r'_r i_{qr} + (\omega - \omega_r) \lambda_{dr} + \frac{d\lambda_{qr}}{dt} \quad (45)$$

$$v_{dr} = r'_r i_{dr} - (\omega - \omega_r) \lambda_{qr} + \frac{d\lambda_{dr}}{dt} \quad (46)$$

respectively, where  $i \in 1, 5$ . Transformation of the referred stator and rotor flux linkage equations (again, with  $m=3$ ) yields

$$\lambda_{qs1} = L_{ls} i_{qs1} + \lambda_{qm} \quad (47)$$

$$\lambda_{ds1} = L_{ls} i_{ds1} + \lambda_{dm} \quad (48)$$

and

$$\lambda_{qr} = L'_{lr} i_{qr} + \lambda_{qm} \quad (49)$$

$$\lambda_{dr} = L'_{lr} i_{dr} + \lambda_{dm} \quad (50)$$

where

$$\lambda_{qm} = L_m \left( \sum_{i=1}^5 i_{qs1} + i_{qr} \right) \quad (51)$$

$$\lambda_{dm} = L_m \left( \sum_{i=1}^5 i_{ds1} + i_{dr} \right) \quad (52)$$

and

$$L_m = \frac{3}{2} L_{ms} \quad (53)$$

Finally, the electromagnetic torque may be expressed

$$T_e = \frac{3P}{2} \sum_{i=1}^5 (\lambda_{dm} i_{qs1} - \lambda_{qm} i_{ds1}) \quad (54)$$

The qd equivalent circuit corresponding to (42-52) is illustrated in Fig. 4. As can be seen the equivalent circuit is comprised of a q-axis circuit, d-axis circuit, and five identical and non-coupled zero-sequence circuits.

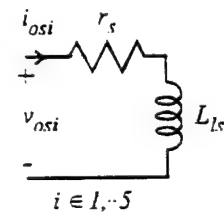
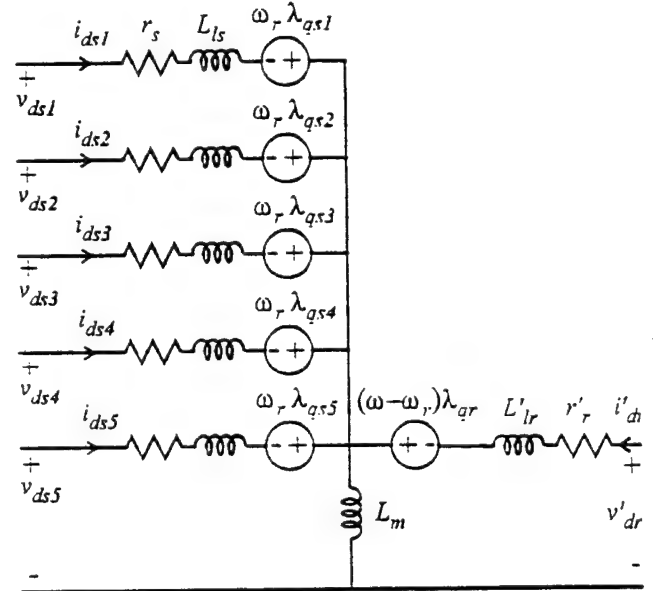
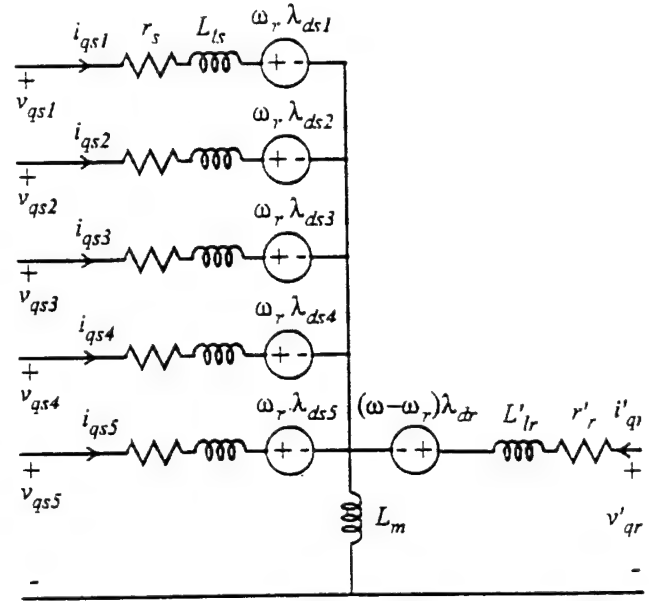


Figure 4. Five 3-phase set QD equivalent circuit of 15-phase induction machine.

The 3-phase set based equivalent circuit has several attractive characteristics. First, the transformation is essentially identical to the standard 3-phase transformation, at least on a per set basis. Second, the zero sequence circuits are identical and decoupled. In addition, the equivalent circuit is very suggestive from a control point of view to handle the situation in which one H-bridge is disabled. For example, suppose that the drive is used in the context of a field-oriented control system and a fault is detected on one H-bridge corresponding to one phase of the  $i$ 'th 3-phase stator set. Then the  $i$ 'th q- and d-axis current command would be set equal to zero, and the other two H-bridges associated with the 3-phase set would also be disabled. Next, the total d-axis stator current command would be maintained by increasing the d-axis current command in the other for sets, so as to maintain constant rotor flux. Depending upon the torque command the q-axis current commands in the other phases could be increased so as to maintain constant torque, unless the current command has reached its limit in which case the torque output would be forced to decrease. Even so, this strategy has advantages in that machine operation would be balanced which would avoid unexpected thermal losses and torque harmonics.

Another useful choice of reference frames is based on a 5-phase set based approach with three q- and d-axis and nine zero sequence variables. This choice is particularly convenient because such a construction associates groups all the phases connected to a given dc link into a set. Before considering the full 15 by 15 transformation, it is appropriate to set forth the transformation of a 5-phase set to q- and d-axis variables. Such a transformation may be expressed as

$$f_{qd5s} = K_{5s} f_{5s} \quad (55)$$

where

$$f_{5s} = [f_{1s} \cdots f_{5s}]^T \quad (56)$$

and

$$f_{qd5s} = [f_{qs} \ f_{ds} \ f_{0s} \ f_{\alpha s} \ f_{\beta s}]^T \quad (57)$$

In order to derive the construction of  $K_{5s}$ , it is convenient to express it in terms of rows as

$$K_{5s} = \begin{bmatrix} q_1 \\ \vdots \\ q_5 \end{bmatrix} \quad (58)$$

where  $q_i$  denotes the  $i$ 'th row of  $K_{5s}$ . The first and second rows of  $K_{5s}$  formulate the q- and d-axis. From geometrical arguments, the first two rows may be expressed as

$$q_1 = \frac{2}{5} \begin{bmatrix} \cos(\theta) & \cos(\theta - \frac{2\pi}{5}) & \cos(\theta - \frac{4\pi}{5}) & \cos(\theta - \frac{6\pi}{5}) & \cos(\theta - \frac{8\pi}{5}) \end{bmatrix} \quad (59)$$

$$q_2 = \frac{2}{5} \begin{bmatrix} \sin(\theta) & \sin(\theta - \frac{2\pi}{5}) & \sin(\theta - \frac{4\pi}{5}) & \sin(\theta - \frac{6\pi}{5}) & \sin(\theta - \frac{8\pi}{5}) \end{bmatrix} \quad (60)$$

It is convenient to define the third row of the transformation as

$$q_3 = \begin{bmatrix} \frac{1}{5} & \frac{1}{5} & \frac{1}{5} & \frac{1}{5} & \frac{1}{5} \end{bmatrix} \quad (61)$$

With this definition,  $f_{0s}$  is the instantaneous average phase current in the 5-phase set. Furthermore (61) is clearly orthogonal to both (59) and (60). Definition of the other sequence variables,  $f_{\alpha s}$  and  $f_{\beta s}$ , is somewhat more difficult because it is not clear what the physical interpretation, if any, should be. Herein, the row vectors  $q_4$  and  $q_5$  will be obtained using the Gram-Schmidt algorithm, in which a non-orthogonal set of basis vectors is transformed to a orthogonal one. The non-orthogonal set is assumed to consist of  $q_1, q_2, q_3, a_4$ , and  $a_5$ , where, as previously noted,  $q_1$  through  $q_3$  are already mutually orthogonal and

$$a_4 = \begin{bmatrix} 1 & 0 & 0 & 0 & 0 \end{bmatrix} \quad (62)$$

$$a_5 = \begin{bmatrix} 0 & 1 & 0 & 0 & 0 \end{bmatrix} \quad (63)$$

which yields

$$q_4 = \frac{1}{5\sqrt{2}} \begin{bmatrix} 2 & -1 - 2\cos\frac{2\pi}{5} & -1 - 2\cos\frac{4\pi}{5} & -1 - 2\cos\frac{6\pi}{5} & -1 - 2\cos\frac{8\pi}{5} \end{bmatrix} \quad (64)$$

and

$$q_5 = \frac{2}{5\sqrt{150 + 100\cos\frac{4\pi}{5}}} \begin{bmatrix} 0 & 2 - 2\cos\frac{2\pi}{5} & -1 - 4\cos\frac{2\pi}{5} & -1 - 4\cos\frac{4\pi}{5} & -3 - 2\cos\frac{4\pi}{5} \end{bmatrix} \quad (65)$$

Thus the 5-phase based transformation is given by

$$K_{5s} = \frac{2}{5} \begin{bmatrix} \cos(\theta) & \cos(\theta - \frac{2\pi}{5}) \\ \sin(\theta) & \sin(\theta - \frac{2\pi}{5}) \\ \frac{1}{2} & \frac{1}{2} \\ \frac{1}{\sqrt{2}} & \frac{-1 - 2\cos\frac{2\pi}{5}}{2\sqrt{2}} \\ 0 & \frac{2 - 2\cos\frac{2\pi}{5}}{\sqrt{150 + 100\cos\frac{4\pi}{5}}} \end{bmatrix}$$

$$\begin{bmatrix} \cos(\theta - \frac{4\pi}{5}) & \cos(\theta - \frac{6\pi}{5}) & \cos(\theta - \frac{8\pi}{5}) \\ \sin(\theta - \frac{4\pi}{5}) & \sin(\theta - \frac{6\pi}{5}) & \sin(\theta - \frac{8\pi}{5}) \\ \frac{1}{2} & \frac{1}{2} & \frac{1}{2} \\ \frac{-1-2\cos\frac{4\pi}{5}}{2\sqrt{2}} & \frac{-1-2\cos\frac{4\pi}{5}}{2\sqrt{2}} & \frac{-1-2\cos\frac{4\pi}{5}}{2\sqrt{2}} \\ \frac{-1-4\cos\frac{2\pi}{5}}{\sqrt{150+100\cos\frac{4\pi}{5}}} & \frac{-1-4\cos\frac{4\pi}{5}}{\sqrt{150+100\cos\frac{4\pi}{5}}} & \frac{-3-2\cos\frac{4\pi}{5}}{\sqrt{150+100\cos\frac{4\pi}{5}}} \end{bmatrix} \quad (66)$$

The extension of the 5-phase transformation to the 15-phase case begins with the definition of the full 15-phase stator transformation. In particular,

$$\mathbf{f}_{qds} = \mathbf{K}_s \mathbf{f}_s \quad (67)$$

where

$$\mathbf{f}_{qds} = \begin{bmatrix} \mathbf{f}_{qds1} & \mathbf{f}_{qds2} & \mathbf{f}_{qds3} \end{bmatrix}^T \quad (68)$$

and

$$\mathbf{f}_{qds} = \begin{bmatrix} f_{qs1} & f_{ds1} & f_{0s1} & f_{\alpha s1} & f_{\beta s1} \end{bmatrix}^T \quad (69)$$

It should be noted that the same symbolism is being used as in the previous 15-phase transformation. However, this should not arise because the two transformations are never used at the same time. In this case, the transformation  $\mathbf{K}_s$  is formed so as to apply  $\mathbf{K}_{s_i}$  to three independent 5-phase sets (this will require adjusting the phase of the reference frame position dependent terms). This yields

$$\mathbf{K}_s = \begin{bmatrix} \mathbf{K}_{s1} \\ \mathbf{K}_{s2} \\ \mathbf{K}_{s3} \end{bmatrix} \quad (70)$$

where all elements of  $\mathbf{K}_{s_i}$  are zero except those in the  $i$ 'th,  $3+i$ 'th,  $6+i$ 'th,  $9+i$ 'th, and  $12+i$ 'th columns. In particular, the  $j$ 'th column of  $\mathbf{K}_{s_i}$  is given by

$$j' \text{th column}(\mathbf{K}_{s_i}) = \begin{bmatrix} \frac{2}{5} \cos(\theta - (j-1)\frac{\pi}{15}) \\ \frac{2}{5} \sin(\theta - (j-1)\frac{\pi}{15}) \\ [\mathbf{K}_{s_i}]_{3, \frac{j+i-3}{5}} \\ [\mathbf{K}_{s_i}]_{4, \frac{j+i-3}{5}} \\ [\mathbf{K}_{s_i}]_{5, \frac{j+i-3}{5}} \end{bmatrix} \quad (71)$$

where

$$j \in i, 3+i, 6+i, 9+i, 12+i \quad (72)$$

The rotor transformation is identical to that given by (33) and (41).

The next step is to actually transform the referred variable machine model (with  $m=5$ ) using the transformation

set forth in (67). The stator and rotor voltage equations become

$$v_{qs1} = r_s i_{qs1} + \omega \lambda_{ds1} + \frac{d\lambda_{qs1}}{dt} \quad (73)$$

$$v_{ds1} = r_s i_{ds1} - \omega \lambda_{qs1} + \frac{d\lambda_{ds1}}{dt} \quad (74)$$

$$v_{0s1} = r_s i_{0s1} + \frac{d\lambda_{0s1}}{dt} \quad (75)$$

$$v_{\alpha s1} = r_s i_{\alpha s1} + \frac{d\lambda_{\alpha s1}}{dt} \quad (76)$$

$$v_{\beta s1} = r_s i_{\beta s1} + \frac{d\lambda_{\beta s1}}{dt} \quad (77)$$

and

$$v_{qr} = r_r' i_{qr} + (\omega - \omega_r) \lambda_{dr} + \frac{d\lambda_{qr}}{dt} \quad (78)$$

$$v_{dr} = r_r' i_{dr} - (\omega - \omega_r) \lambda_{qr} + \frac{d\lambda_{dr}}{dt} \quad (79)$$

where  $i \in 1, 2, 3$ . The flux stator linkage equations may be expressed as

$$\lambda_{qs1} = L_{ls} i_{qs1} + \lambda_{qm} \quad (80)$$

$$\lambda_{ds1} = L_{ls} i_{ds1} + \lambda_{dm} \quad (81)$$

$$\lambda_{0s1} = L_{ls} i_{0s1} \quad (82)$$

$$\lambda_{\alpha s1} = L_{ls} i_{\alpha s1} \quad (83)$$

$$\lambda_{\beta s1} = L_{ls} i_{\beta s1} \quad (84)$$

and the rotor flux linkage equations as

$$\lambda_{qr} = L_{lr} i_{qr} + \lambda_{qm} \quad (85)$$

$$\lambda_{dr} = L_{lr} i_{dr} + \lambda_{dm} \quad (86)$$

where

$$\lambda_{qm} = L_m \left( \sum_{i=1}^3 i_{qs1} + i_{qr} \right) \quad (87)$$

$$\lambda_{dm} = L_m \left( \sum_{i=1}^3 i_{ds1} + i_{dr} \right) \quad (88)$$

and

$$L_m = \frac{5}{2} L_{ms} \quad (89)$$

Finally, electromagnetic torque may be expressed

$$T_e = \frac{5P}{2} \left( \lambda_{dm} \sum_{i=1}^3 i_{qs1} - \lambda_{qm} \sum_{i=1}^3 i_{ds1} \right) \quad (90)$$

The three 5-phase set based qd equivalent circuit of the induction machine is illustrated in Fig. 5.

## VI. DETAILED INVERTER MODEL AND DRIVE SIMULATION

The detailed simulation of the inverter drive makes use of a machine variable inverter model and the 3-phase set based qd model in the stationary reference frame. The state variables of the electrical system will be the stator and rotor flux linkages. The simulation structure is illustrated in Fig.

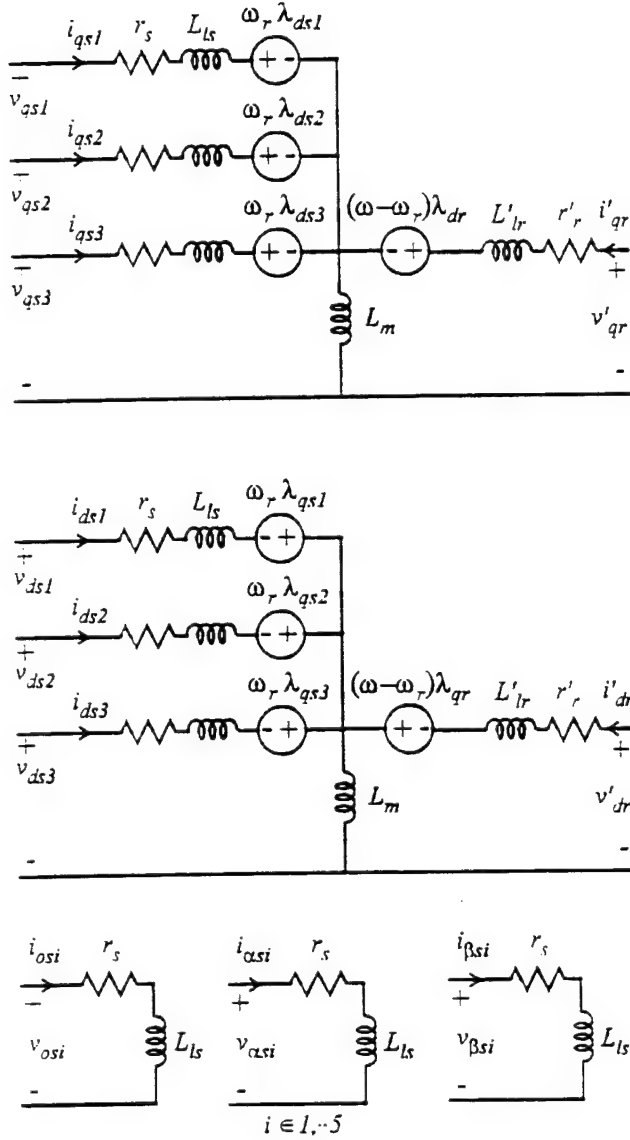


Figure 5. Three 5-phase set QD equivalent circuit of 15-phase induction machine.

6. The algorithm used to calculate the derivative of the flux linkages based on the input and state variables is as follows. First, given the flux linkages, the qd currents are found by solving (47-52). From the qd current vector the machine currents are found using the inverse transformation (which is constant if the stationary reference frame is selected, and sparse). Next the switching state vector is found in accordance with (3). Based on the switching vector  $s$  and the machine current  $i$ , the voltage vector can be found. In particular,

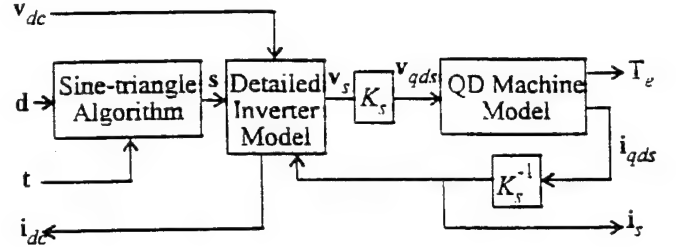


Figure 6. Detailed simulation structure.

$$v_{s_i} = \begin{cases} v_{dcj} - 2v_t & \text{if } s_i = 1 \text{ and } i_{s_i} \geq 0 \\ v_{dcj} + 2v_d & \text{if } s_i = 1 \text{ and } i_{s_i} < 0 \\ -v_{dcj} + 2v_t & \text{if } s_i = -1 \text{ and } i_{s_i} \leq 0 \\ -v_{dcj} - 2v_d & \text{if } s_i = -1 \text{ and } i_{s_i} > 0 \end{cases} \quad (91)$$

where  $j$  corresponds to the dc link of the  $i$ 'th phase. The dc current into the  $i$ 'th H-bridge is given by

$$i_{dch_i} = \begin{cases} i_{s_i} & \text{if } s_i = 1 \\ -i_{s_i} & \text{if } s_i = -1 \end{cases} \quad (92)$$

Finally, the dc link current may be expressed

$$i_{dcj} = \sum_{i=1}^5 i_{dch_{3(n-1)+j}} \quad (93)$$

where  $j \in 1, 2, 3$ . Based on the machine variable voltage vector determined by (91) the qd variables whereupon (42-46) may be used to calculate the time derivative of the flux linkages.

## VII. AVERAGE-VALUE INVERTER MODEL AND DRIVE SIMULATION

The average-value model presented herein is based upon the 5-phase set based qd model using a synchronous reference frame. The first step necessary in order to formulate the complete model is to determine the input voltage vector  $\bar{v}_{qds}$  (the line indicates fast average value) based upon the dc voltage vector  $\bar{v}_{dc}$  and the qd duty cycle vector  $d_{dq}$ . (obtained by transforming  $d$  to qd variables). For the normal situation in which the sine triangle algorithm is not overmodulated  $d_{dq}$  is such that

$$|d_i| < 1 \quad i \in 1 \dots 15 \quad (94)$$

it can be readily shown (since the fast average of the output voltage is directly proportional to the input voltage) that

$$\bar{v}_{qds_j} = v_{dcj} d_{dq_j} \quad j \in 1 \dots 3 \quad (95)$$

In the overmodulated case, which is to say that

$$|d_i| > 1 \quad (96)$$

for some  $i$ , then assuming the instantaneous overmodulation is due to the q- and d-axis components rather than the zero sequence components (which is normally the case since the zero sequence components are normally zero) then using Fourier analysis to extract the fundamental component it can be shown that

$$\bar{v}_{qdj} = v_{dcj} \frac{d_{dqj}}{|d_{dqj}|} f(|d_{dqj}|) \quad j \in 1 \dots 3 \quad (97)$$

where

$$|d_{dqj}| = \sqrt{d_{qj}^2 + d_{dj}^2} \quad (98)$$

and

$$f(x) = \frac{2}{\pi} \left( x \arcsin(1/x) + \sqrt{1 - \left(\frac{1}{x}\right)^2} \right) \quad (99)$$

Once the qd input voltage has been established, the qd machine model may be used to determine the qd current vector and calculate the derivative of flux linkages. It can also be used to calculate the electromagnetic torque, as is necessary to compute the mechanical dynamics. In order to interface the drive simulation to the rest of the electrical system (the dc supplies) one further calculation is necessary: that is the calculation of the dc link currents. This is based on power balance.

In the case of the five-phase transformation (66), it can be shown that the power into a five-phase set is given by

$$P = \frac{5}{2} (v_{qs} i_{qs} + v_{ds} i_{ds} + 2(v_{0s} i_{0s} + v_{\alpha s} i_{\alpha s} + v_{\beta s} i_{\beta s})) \quad (100)$$

Therefore the power into the  $j$ 'th dc link is given by

$$P_j = \frac{5}{2} (v_{qs_j} i_{qs_j} + v_{ds_j} i_{ds_j} + 2(v_{0s_j} i_{0s_j} + v_{\alpha s_j} i_{\alpha s_j} + v_{\beta s_j} i_{\beta s_j})) \quad (101)$$

The power into the  $j$ 'th link may also be expressed as

$$P_j = v_{dcj} i_{dcj} \quad (102)$$

Equating the two results and incorporating (95) yields

$$i_{dcj} = \frac{5}{2} (d_{qs} i_{qs} + d_{ds} i_{ds} + 2(d_{0s} i_{0s} + d_{\alpha s} i_{\alpha s} + d_{\beta s} i_{\beta s})) \quad (103)$$

or, in the case of overmodulated operation

$$i_{dcj} = \frac{5}{2} (d_{qs} i_{qs} + d_{ds} i_{ds} + 2(d_{0s} i_{0s} + d_{\alpha s} i_{\alpha s} + d_{\beta s} i_{\beta s})) \frac{f(|d_{dqj}|)}{|d_{dqj}|} \quad (104)$$

The structure of the average value is illustrated in Fig. 7. Therein, all qd variables and electromagnetic torque should be interpreted on a fast average basis, and the qd machine model is the three 5-phase set based model in the synchronous reference frame.

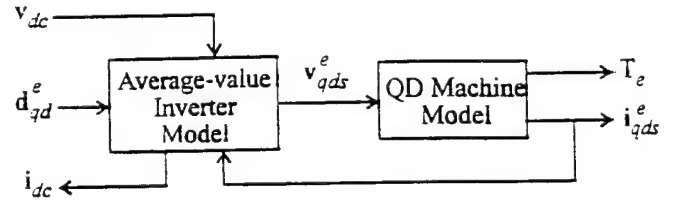


Figure 7. Average-value simulation structure..

## Appendix C

### Control of a 15-Phase Induction Motor Drive System

#### I. INTRODUCTION

The work set forth herein has been conducted for the SBIR Phase I. In particular, in order to include the IPS drive system load a substantial effort had to be placed into the control design. The work has been formatted in journal format so that it may be published in the technical literature at a future date.

#### II. SYSTEM DESCRIPTION

The application of the drive system under consideration is a Naval propulsion system illustrated in Fig. 1. Therein, a turbine is the prime mover for a 3-phase, 60-Hz, 20 MW, 4160 V 1-l rms synchronous machine, whose output voltage is controlled by an IEEE Type 2 excitation system. The principal load on the bus is a 19 MW induction motor drive system, although the synchronous machine also provides ship service power. Parameters of the synchronous machine and exciter are listed in Table 1.

Table 1. Synchronous Machine / Exciter Parameters

$r_s = 1.27 \text{ m}\Omega$	$L_{ls} = 396 \text{ }\mu\text{H}$	$L_{mq} = 2.51 \text{ H}$	$L_{md} = 2.79 \text{ mH}$
$r_{ka} = 5.26 \text{ m}\Omega$	$L_{lka} = 157 \text{ }\mu\text{H}$	$r_{kd} = 4.74 \text{ }\mu\text{H}$	$L_{lkd} = 69.8 \text{ }\mu\text{H}$
$r_{fd} = 401 \text{ }\mu\Omega$	$L_{lfd} = 227 \text{ }\mu\text{H}$	$P = 2$	$T_R = 1 \text{ ms}$
$v_{ref} = 4160 \text{ V}$	$v_{RMAX} = 7.3 \text{ pu}$	$v_{RMIN} = 0 \text{ pu}$	$K_F = 0.03$
$K_A = 400$	$T_A = 20 \text{ ms}$	$K_E = 1.0$	$T_E = 0.8 \text{ s}$
$T_{F1} = 1.0 \text{ s}$	$T_{F2} = 1.0 \text{ s}$	$S_{E75} = 0.5$	$S_{E100} = 0.86$

Fig. 2 illustrates the inverter topology of the 15-phase induction motor drive system which is the subject of this

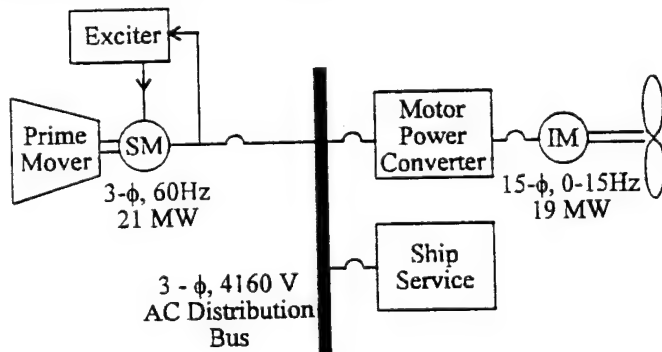


Figure 1. System Architecture.

analysis. As can be seen from Fig. 1, the motor power converter is divided into three parallel rectifier - dc link - inverter paths. In each path, a 6-pulse uncontrolled rectifier output is filtered with an LC circuit ( $L_f = 3 \text{ mH}$  and  $C_f = 1 \text{ mF}$ ), the output of which is connected to five H-bridge inverters, wherein  $H_i$  designates the  $i$ 'th H-bridge which controls the applied to the  $i$ 'th phase of the machine. The phases of the machine are labeled such that the fundamental component of the voltage applied to the  $i$ 'th phase is displaced  $(i-1)24^\circ$  (electrical) from the first phase.

The voltage vector  $v_{dc}$  will be used to designate the individual rail voltages, i.e.,

$$v_{dc} = \begin{bmatrix} v_{dc1} & v_{dc2} & v_{dc3} \end{bmatrix}^T \quad (1)$$

An identical convention will be used to identify the dc current vector  $i_{dc}$ , the rectifier current vector  $i_r$ , and the rectifier voltage vector  $v_r$ .

The configuration of each H-bridge is illustrated in Fig. 3. Therein, each semiconductor shown represents an effective device which is physically constructed using a series connection of several devices in order to achieve the necessary voltage rating. The on/off status of each effective switching device in the  $i$ 'th bridge is designated  $D_1$ , through  $D_4$ , and  $v_{s1}$ ,  $i_{s1}$ , and  $i_{dch1}$  denote the  $i$ 'th phase voltage,  $i$ 'th phase current (defined positive into the machine), and the dc link current into the  $i$ 'th H-bridge, respectively. The switching state of the  $i$ 'th H-bridge will be denoted

$$s_i = \begin{cases} 1 & D_1, \text{ and } D_4, \text{ on} \\ 0 & (D_1, \text{ on and } D_2, \text{ on}) \text{ or } (D_2, \text{ on and } D_4, \text{ on}) \\ -1 & D_2, \text{ and } D_3, \text{ on} \end{cases} \quad (2)$$

and  $s$  will denote the vector of switching states. The goal of the controller set forth herein will be to specify  $s$  as a function of time in such a way that the electromagnetic torque  $T_e$  closely tracks the desired torque  $T_e^*$ .

#### III. INDUCTION MOTOR MODEL

The control of the induction motor is formulated on the three 5-phase set based qd transformation as set forth in Appendix B. In particular, the stator transformation may be expressed as

$$f_{qds1} = K_{s1} f_{s1} \quad (3)$$

where

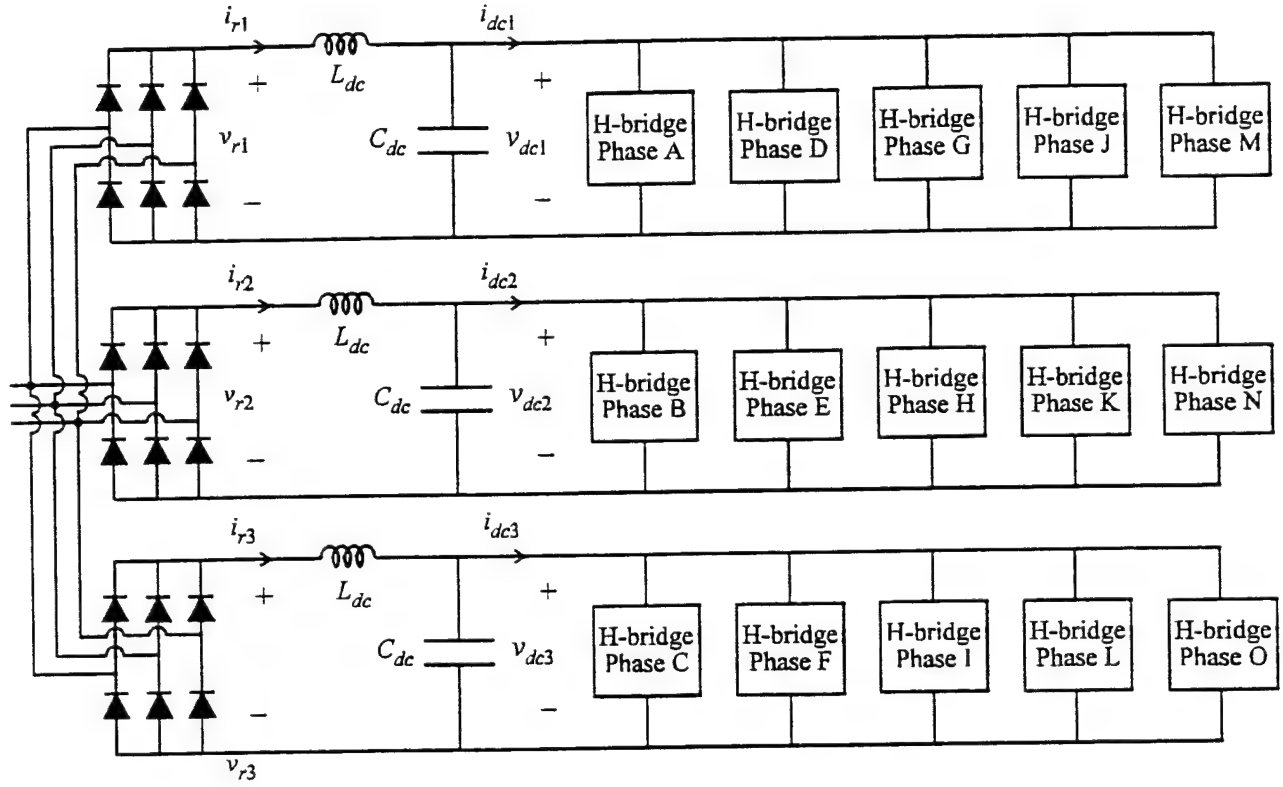


Figure 2. Motor Controller.

$$\mathbf{f}_{s1} = [f_{s1} \ f_{s1+3} \ f_{s1+6} \ f_{s1+9} \ f_{s1+12}]^T \quad (4)$$

In (6)

$$\theta_{e1} = \theta_e - (i-1) \frac{\pi}{15} \quad (7)$$

$$\mathbf{f}_{qds1} = [f_{qs1} \ f_{ds1} \ f_{0s1} \ f_{\alpha s1} \ f_{\beta s1}]^T \quad (5)$$

where  $\theta_e$  is the position of the synchronous reference frame. The rotor transformation is given by

$$\mathbf{f}_{qdr} = \mathbf{K}_r \mathbf{f}_r \quad (8)$$

$i \in 1, 2, 3$ ,  $f$  may be a voltage  $v$ , current  $i$ , or flux linkage  $\Lambda$ , and

where

$$\mathbf{K}_{s1} = \frac{2}{5} \begin{bmatrix} \cos(\theta_{e1}) & \cos(\theta_{e1} - \frac{2\pi}{5}) & \frac{1}{2} & \frac{1}{2} \\ \sin(\theta_{e1}) & \sin(\theta_{e1} - \frac{2\pi}{5}) & \frac{1}{\sqrt{2}} & \frac{-1-2\cos\frac{2\pi}{5}}{2\sqrt{2}} \\ 0 & \frac{2-2\cos\frac{2\pi}{5}}{\sqrt{150+100\cos\frac{4\pi}{5}}} \end{bmatrix}$$

$$\begin{bmatrix} \cos(\theta_{e1} - \frac{4\pi}{5}) & \cos(\theta_{e1} - \frac{6\pi}{5}) & \cos(\theta_{e1} - \frac{8\pi}{5}) \\ \sin(\theta_{e1} - \frac{4\pi}{5}) & \sin(\theta_{e1} - \frac{6\pi}{5}) & \sin(\theta_{e1} - \frac{8\pi}{5}) \\ \frac{1}{2} & \frac{1}{2} & \frac{1}{2} \\ \frac{-1-2\cos\frac{4\pi}{5}}{2\sqrt{2}} & \frac{-1-2\cos\frac{4\pi}{5}}{2\sqrt{2}} & \frac{-1-2\cos\frac{2\pi}{5}}{2\sqrt{2}} \\ \frac{-1-4\cos\frac{2\pi}{5}}{\sqrt{150+100\cos\frac{4\pi}{5}}} & \frac{-1-4\cos\frac{4\pi}{5}}{\sqrt{150+100\cos\frac{4\pi}{5}}} & \frac{-3-2\cos\frac{4\pi}{5}}{\sqrt{150+100\cos\frac{4\pi}{5}}} \end{bmatrix}$$

(6)

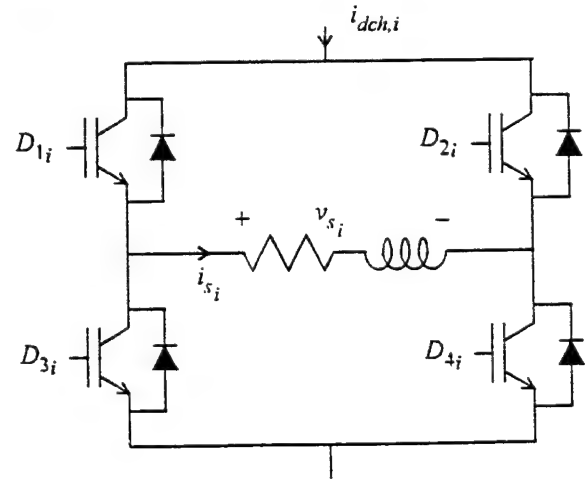


Figure 3. H-bridge.

$$\mathbf{f}_{abr} = \begin{bmatrix} f_{ar} & f_{br} \end{bmatrix}^T \quad (9)$$

$$\mathbf{f}_{qdr} = \begin{bmatrix} f_{qr} & f_{dr} \end{bmatrix}^T \quad (10)$$

and

$$\mathbf{K}_r = \begin{bmatrix} \cos(\theta_e - \theta_r) & \sin(\theta_e - \theta_r) \\ \sin(\theta_e - \theta_r) & -\cos(\theta_e - \theta_r) \end{bmatrix} \quad (11)$$

In (11)  $\theta_r$  denotes the electrical rotor position. In terms of qd variables, the induction motor stator and rotor voltage equations may be expressed as

$$v_{qs1} = r_s i_{qs1} + \omega_e \lambda_{ds1} + \frac{d\lambda_{qs1}}{dt} \quad (12)$$

$$v_{ds1} = r_s i_{ds1} - \omega_e \lambda_{qs1} + \frac{d\lambda_{ds1}}{dt} \quad (13)$$

$$v_{0s1} = r_s i_{0s1} + \frac{d\lambda_{0s1}}{dt} \quad (14)$$

$$v_{\alpha s1} = r_s i_{\alpha s1} + \frac{d\lambda_{\alpha s1}}{dt} \quad (15)$$

$$v_{\beta s1} = r_s i_{\beta s1} + \frac{d\lambda_{\beta s1}}{dt} \quad (16)$$

and

$$v'_{qr} = r'_r i'_{qr} + (\omega_e - \omega_r) \lambda'_{dr} + \frac{d\lambda'_{qr}}{dt} \quad (17)$$

$$v'_{dr} = r'_r i'_{dr} - (\omega_e - \omega_r) \lambda'_{qr} + \frac{d\lambda'_{dr}}{dt} \quad (18)$$

respectively. Since the machine is of squirrel cage design, the q- and d-axis rotor voltages are both zero. The stator flux linkage equations may be expressed as

$$\lambda_{qs1} = L_{ls} i_{qs1} + \lambda_{qm} \quad (19)$$

$$\lambda_{ds1} = L_{ls} i_{ds1} + \lambda_{dm} \quad (20)$$

$$\lambda_{0s1} = L_{ls} i_{0s1} \quad (21)$$

$$\lambda_{\alpha s1} = L_{ls} i_{\alpha s1} \quad (22)$$

$$\lambda_{\beta s1} = L_{ls} i_{\beta s1} \quad (23)$$

and the rotor flux linkage equations as

$$\lambda'_{qr} = L_{lr} i'_{qr} + \lambda_{qm} \quad (24)$$

$$\lambda'_{dr} = L_{lr} i'_{dr} + \lambda_{dm} \quad (25)$$

where

$$\lambda_{qm} = L_m \left( \sum_{i=1}^3 i_{qs1} + i'_{qr} \right) \quad (26)$$

$$\lambda_{dm} = L_m \left( \sum_{i=1}^3 i_{ds1} + i'_{dr} \right) \quad (27)$$

Finally, electromagnetic torque may be expressed

$$T_e = \frac{5P}{2} \left( \lambda_{dm} \sum_{i=1}^3 i_{qs1} - \lambda_{qm} \sum_{i=1}^3 i_{ds1} \right) \quad (28)$$

The three 5-phase set based qd equivalent circuit of the induction machine is illustrated in Fig. 4, and parameters are listed in Table 2.

Table 2. Induction Motor Parameters		
$r_s = 122 \text{ m}\Omega$	$L_{ls} = 6.79 \text{ mH}$	$L_m = 145 \text{ mH}$
$r'_r = 35.7 \text{ m}\Omega$	$L'_{lr} = 7.62$	$P = 12$

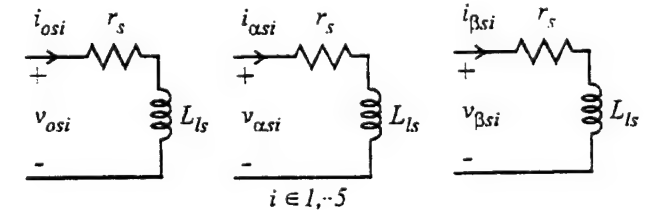
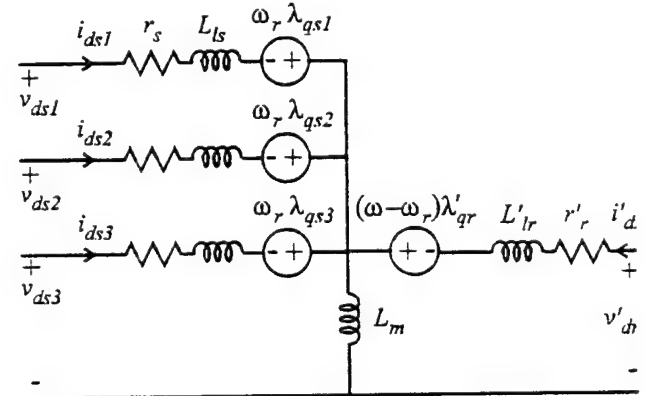
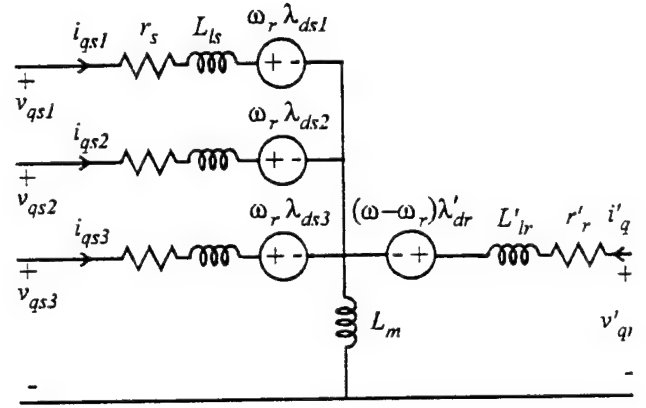


Figure 4. Three 5-phase set QD equivalent circuit of 15-phase induction machine.



#### IV. CONTROLLER ARCHITECTURE

The first decision to be made in the design of the controller was the overall control architecture. Some of the desired properties of the controller included that (i) it must be stable, (ii) it is field oriented based so that the drive will act as a torque transducer, (iii) the currents be tightly controlled in order to protect the inverter semiconductors, and (iv) the switching frequency should be a constant. In regard to (i), most systems are inherently stable. However, because of requirement (iii), that is the currents are to be tightly controlled, this drive system exhibits a negative impedance characteristic which makes the drive inherently unstable. Requirement (ii) is put in place because it simplifies the system design in that with a field-oriented control the response of the torque response of the drive is much faster than the response of the mechanical dynamics, so that in designing the mechanical system controls the electrical dynamics may be neglected. In addition, the fast action of the field oriented control will be useful in stabilizing the dc link, which as previously mentioned is unstable if the motor currents are tightly regulated, which is

in turn a requirement designed to protect the inverter semiconductors (by tightly controlling the currents the semiconductors can be operated close to their maximum current limit, which is important in large drive systems). Finally, requirement (iv) is put in place so that switching losses can be controlled independently of operating point.

These four constraints suggest the controller architecture illustrated in Fig. 5. The structure of the controls closely parallels that of the system in that there are three control channels, one for each dc link. The primary input commands are operation status, a torque command  $T_e^*$ , and a rotor flux command  $\lambda_{dr}^*$ . The first stage of the control is a paralleling control which divides the torque command into three torque commands corresponding to the amount of electromagnetic torque is due to the q-axis current associated with each link,  $T_{e1}^*$ ,  $T_{e2}^*$ , and  $T_{e3}^*$ , respectively. The paralleling controls also divide the d-axis rotor flux into the amount of that flux which is to be contributed by the 5-phase set being supplied by that link. These commands are designated  $\lambda_{dr1}^*$ ,  $\lambda_{dr2}^*$ , and  $\lambda_{dr3}^*$ . For normal operation this process is very simple, as illustrated in Fig. 6. In the case that, say, one dc link

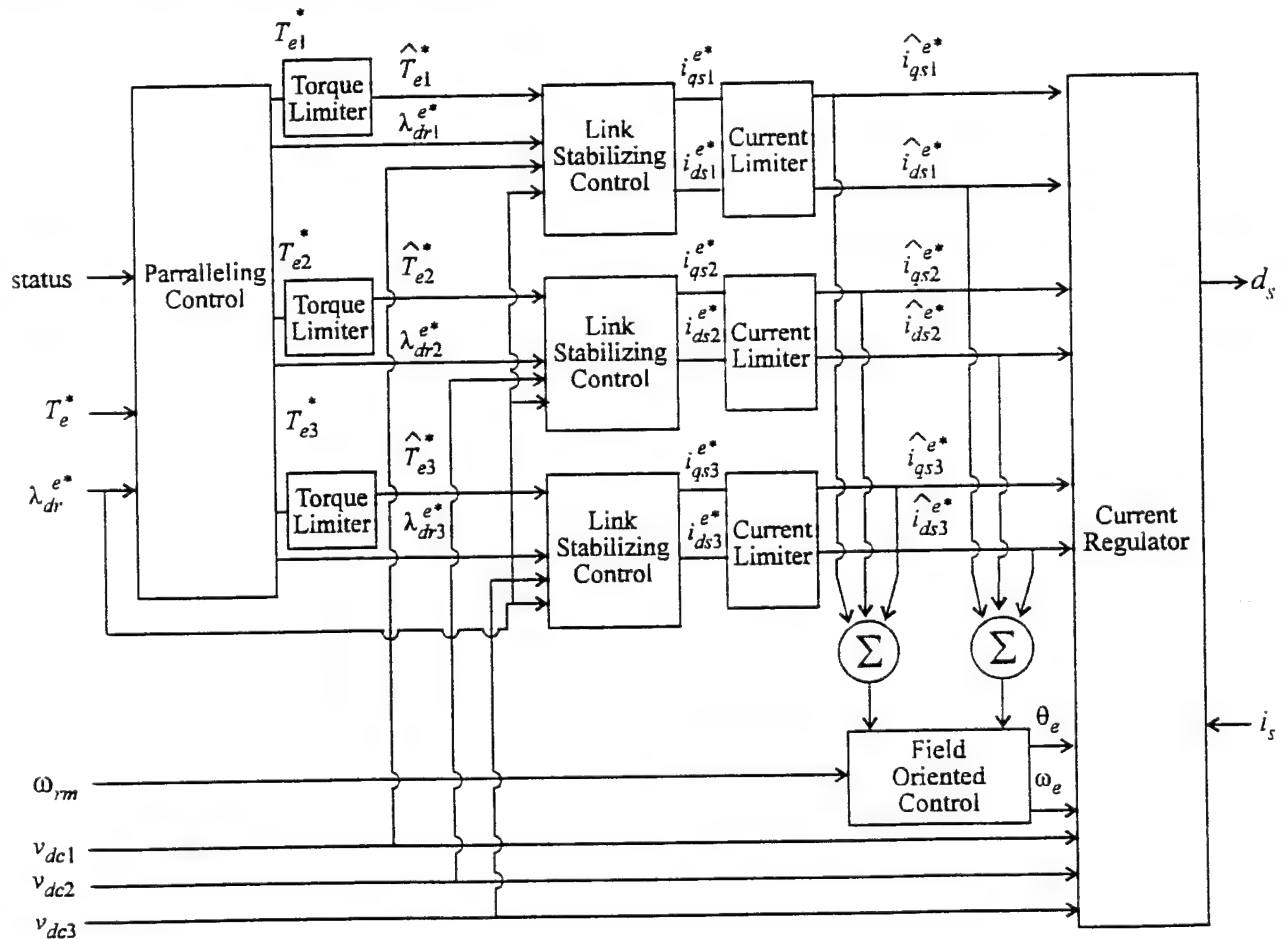


Figure 5. 15-Phase induction motor link stabilized indirect field oriented controller.

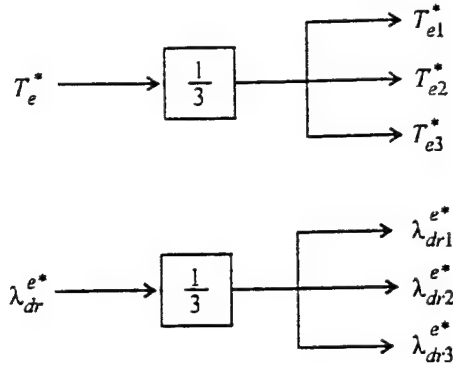


Figure 6. Paralleling controls.

becomes non-operational the torque and flux command is divided between the two-remaining dc links. The next block in the controls is a torque command limiter, as illustrated in Fig. 7. Note that this limit not only bounds the torque command but also the rate of change of the torque command, if desired. The outputs of the torque limiters are the link torque commands denoted  $\hat{T}_{e1}^*$ ,  $\hat{T}_{e2}^*$ , and  $\hat{T}_{e3}^*$ .

Based on the link flux linkage commands and the link torque commands, the desired q- and d-axis currents for each link  $i_{qs1}^*$  and  $i_{ds1}^*$  are established using the link stabilizing control illustrated in Fig. 8. The function of this control is to modify the qd current commands such that the negative impedance instability is avoided. This is accomplished by making the inverter appear to be an open circuit at frequencies much greater than  $1/\tau$ . Details are set forth in Appendix A. The outputs of the link stabilizing control are then passed through a current limiter, as illustrated in Fig. 9. Note that the q- and d-axis currents are not limited symmetrically. Instead, the d-axis current is given priority so as to maintain the desired flux level. This is important because it prevents a transient which invokes the current limit from disturbing the rotor flux and thereby resulting in loss of proper flux orientation.

Based upon the limited current command and the mechanical rotor speed  $\omega_{rm}$ , the indirect field oriented control illustrated in Fig. 10 establishes the speed and position of the synchronous reference frame, denoted  $\omega_s$  and  $\theta_s$ , respectively. Note that part of the indirect field oriented control which establishes the q- and d-axis current commands has been incorporated into the link stabilizing control.

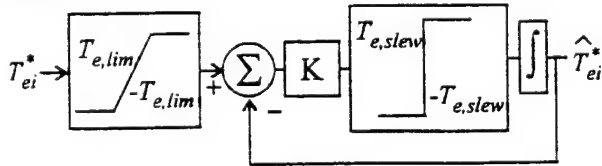


Figure 7. Torque limiter.

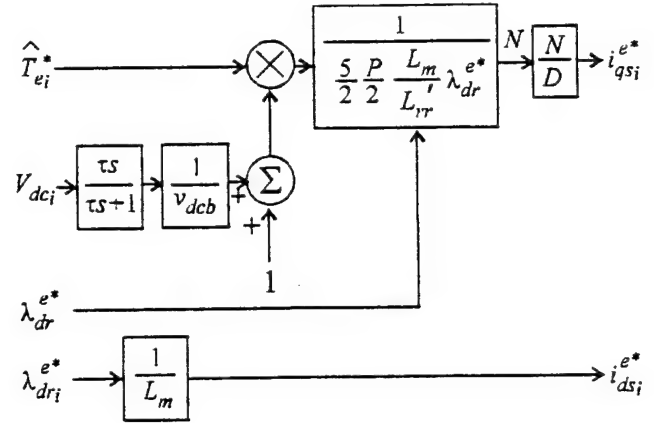


Figure 8. Link stabilizing control.

In addition, although, the details will not be set forth herein, the fact that indirect field oriented control makes use of the drive parameters coupled with the size of the drive necessitates the use of an on line-parameter estimator such as a Kalman filter. This aspect of the control has not been set forth herein but is an important part of the indirect field oriented controller.

The final aspect of the control, and the one which will be the focus of this paper, is the design of the current regulator. The function of the duty current regulator will be to establish the duty cycle signal to a sine-triangle modulator such that the actual currents are equal to the commanded currents. Inputs to the current regulator include the commanded q- and d-axis currents, the dc link voltages, the speed and position of the synchronous reference frame, and finally the instantaneous phase currents.

## VI. DECOUPLING TRANSFORMATION

From Fig. 4, it is apparent that the q- and d-axis circuits are highly coupled which complicates the control design. However, by suitable selection of a transformation, the q- and d-axis sets can be decoupled. In order to derive this transformation, it is convenient to first express the stator

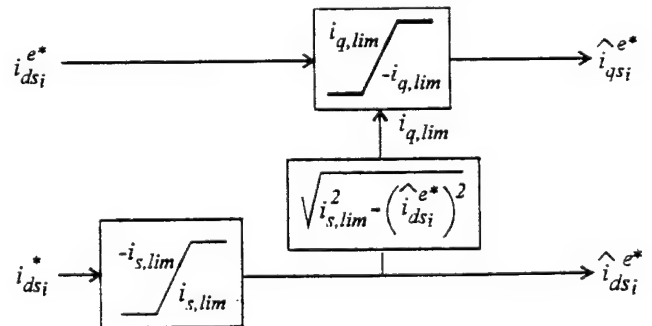


Figure 9. Current limit control.

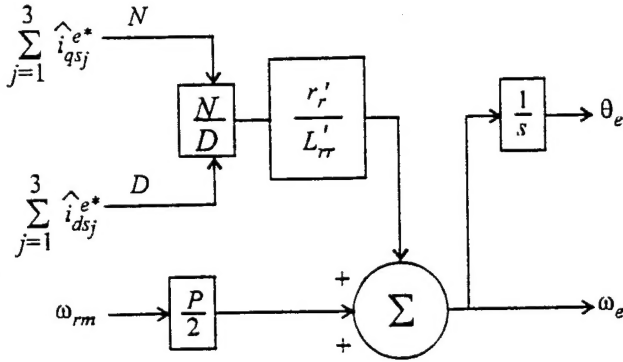


Figure 10. Field oriented controller.

voltage equations in subtransient form. In the case of the q-axis, solving (24,26) for the rotor current and substitution into (19) yields

$$\lambda_{qs1} = L_{ls} i_{qs1} + (L'_{lr} || L_m) \sum_{i=1}^3 i_{qs1} + \frac{L_m}{L'_{rr}} \lambda_{qr} \quad (28)$$

Similarly, for the d-axis

$$\lambda_{ds1} = L_{ls} i_{ds1} + (L'_{lr} || L_m) \sum_{i=1}^3 i_{ds1} + \frac{L_m}{L'_{rr}} \lambda_{dr} \quad (29)$$

By manipulation of (12,13,17,18,28,29) it is possible to express the stator voltage equation solely in terms of the stator currents and rotor flux linkages. In particular,

$$\begin{aligned} v_{qs123} = & r_s i_{qs123} + \omega_e L_{ls} i_{ds123} + L_{ls} \frac{d i_{qs123}}{dt} + \\ & \left[ \left( \frac{L_m}{L_{rr}} \right)^2 r'_r + (L'_{lr} || L_m) \frac{d}{dt} \right] U_{3,3} i_{qs123} + \\ & \omega_e (L'_{lr} || L_m) U_{3,3} i_{ds123} - \frac{r'_r L_m}{L'^2_{rr}} U_{3,1} \lambda'_{qr} + \omega_r \frac{L_m}{L_{rr}} U_{3,1} \lambda_{dr} \end{aligned} \quad (30)$$

and

$$\begin{aligned} v_{ds123} = & r_s i_{ds123} - \omega_e L_{ls} i_{qs123} + L_{ls} \frac{d i_{ds123}}{dt} + \\ & \left[ \left( \frac{L_m}{L_{rr}} \right)^2 r'_r + (L'_{lr} || L_m) \frac{d}{dt} \right] U_{3,3} i_{ds123} - \\ & \omega_e (L'_{lr} || L_m) U_{3,3} i_{qs123} - \frac{r'_r L_m}{L'^2_{rr}} U_{3,1} \lambda'_{dr} - \omega_r \frac{L_m}{L_{rr}} U_{3,1} \lambda_{qr} \end{aligned} \quad (31)$$

where  $U_{ij}$  is a  $i$  row by  $j$  column matrix of ones and

$$f_{qs123} = \begin{bmatrix} f_{qs1} & f_{qs2} & f_{qs3} \end{bmatrix}^T \quad (32)$$

$$f_{ds123} = \begin{bmatrix} f_{ds1} & f_{ds2} & f_{ds3} \end{bmatrix}^T \quad (33)$$

where  $f$  may be a voltage, current, or flux linkage.

In order to decouple the three sets of q-axis, it is convenient to transform (30-31) using the transformations

$$f_{qsxz} = T f_{qs123} \quad (34)$$

$$f_{dsxz} = T f_{ds123} \quad (35)$$

where

$$f_{qsxz} = \begin{bmatrix} f_{qsx} & f_{qsy} & f_{qsx} \end{bmatrix}^T \quad (36)$$

$$f_{ds123} = \begin{bmatrix} f_{dsx} & f_{dsy} & f_{dsz} \end{bmatrix}^T \quad (37)$$

and

$$T = \sqrt{\frac{2}{3}} \begin{bmatrix} 1 & -\frac{1}{2} & \frac{1}{2} \\ 0 & -\frac{\sqrt{3}}{2} & \frac{\sqrt{3}}{2} \\ \frac{1}{\sqrt{6}} & \frac{1}{\sqrt{6}} & \frac{1}{\sqrt{6}} \end{bmatrix} \quad (38)$$

Note that (38) is almost orthogonal, except that the last row has been modified so that the z-component of the q- and d-axis variables would correspond to the average of those variables. This transformation yields

$$\begin{aligned} v_{qsxz} = & (r_s + L_{ls} \frac{d}{dt}) i_{qsxz} + \omega_e L_{ls} i_{dsxz} + \\ & \sqrt{6} \left[ \left( \frac{L_m}{L_{rr}} \right)^2 r'_r + (L_m || L_{lr}) \frac{d}{dt} \right] C_{3,3} i_{qsxz} + \\ & \sqrt{6} \omega_e (L_{lr} || L_m) C_{3,3} i_{dsxz} - \frac{r'_r L_m}{L'^2_{rr}} C_{3,1} \lambda'_{qr} + \omega_r \frac{L_m}{L'_{rr}} C_{3,1} \lambda'_{dr} \end{aligned} \quad (39)$$

and

$$\begin{aligned} v_{dsxz} = & (r_s + L_{ls} \frac{d}{dt}) i_{dsxz} - \omega_e L_{ls} i_{qsxz} + \\ & \sqrt{6} \left[ \left( \frac{L_m}{L_{rr}} \right)^2 r'_r + (L_m || L_{lr}) \frac{d}{dt} \right] C_{3,3} i_{dsxz} - \\ & \sqrt{6} \omega_e (L_{lr} || L_m) C_{3,3} i_{qsxz} - \frac{r'_r L_m}{L'^2_{rr}} C_{3,1} \lambda'_{dr} - \omega_r \frac{L_m}{L'_{rr}} C_{3,1} \lambda'_{qr} \end{aligned} \quad (40)$$

where  $C_{ij}$  is an  $i$  by  $j$  matrix whose  $ij$ 'th element is one and whose remaining elements are zero. Upon consideration of the definition of  $C_{ij}$  it can be seen the x-, y-, and z-components of the q- and d-axis stator voltage equations are uncoupled.

## VII. XY-COMPONENT CONTROL

The control of the x-axis component of the q- and d-axis currents is as follows. First, extracting the x-axis components from (39) and (40),

$$v_{qsx} = r_s i_{qsx} + \omega_e L_{ls} i_{dsx} + L_{ls} \frac{d i_{qsx}}{dt} \quad (41)$$

$$v_{dsx} = r_s i_{dsx} - \omega_e L_{ls} i_{qsx} + L_{ls} \frac{d i_{dsx}}{dt} \quad (42)$$

One feature of interest in (41-42) is the coupling between the q- and d-axis, which is troublesome because it introduces a lightly damped eigenvalue whose natural frequency is a function of operating point through  $\omega_e$ . A suitable control law which eliminate this problem is to command a x-component of the voltage of

$$v_{qsx}^* = \omega_e L_{ls} i_{dsx} + (K_{pqx} + \frac{K_{lpx}}{s})(i_{qsx}^* - i_{qsx}) \quad (43)$$

$$v_{dsx}^* = -\omega_e L_{ls} i_{qsx} + (K_{pdx} + \frac{K_{ldx}}{s})(i_{dsx}^* - i_{dsx}) \quad (44)$$

where  $s$  is the Laplace operator and  $K_{pqx}$   $K_{iqx}$  denote the x-component of the q-axis proportional and integral gains, respectively. This control algorithm is depicted in Fig. 11. Assuming that the desired voltage is obtained, the transfer function between the q-axis current command and the q-axis current becomes

$$\frac{i_{qs}}{i_{qs}^*} = \frac{K_{pqx}s + K_{iqx}}{L_s s^2 + (r_s + K_{pqx})s + K_{iqx}} \quad (45)$$

From (45), it can be seen that the poles may be arbitrarily placed. If the poles are widely spaced, and the fastest pole is faster than the stator leakage dynamics, the zero will nearly cancel the first pole, so that the second pole dominates the response. The transfer function for the d-axis is identical, and the control of the y-axis component is identical to that of the x-axis component of the current. Typically, the y-axis component gains will be identical to those of the x-axis. However, the d-axis gains may occasionally be selected to be different than that of the q-axis.

#### VIII. Z-AXIS CONTROL

The voltage equations governing the z-component of the q- and d-axis may be expressed as

$$v_{qs} = r_z i_{qs} + \omega_e L_z i_{qs} + L_z \frac{di_{qs}}{dt} + \frac{r'_m \lambda'_m}{L_s^2} \lambda'_{qr} + \omega_r \frac{L_m}{L'_r} \lambda'_{dr} \quad (46)$$

$$v_{ds} = r_z i_{ds} - \omega_e L_z i_{ds} + L_z \frac{di_{ds}}{dt} + \frac{r'_m \lambda'_m}{L_s^2} \lambda'_{dr} - \omega_r \frac{L_m}{L'_r} \lambda'_{qr} \quad (47)$$

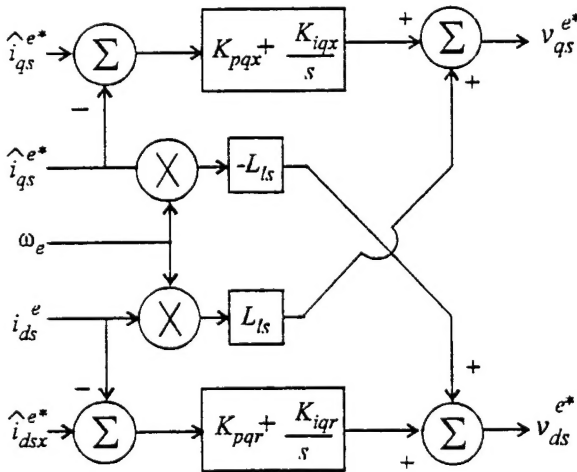


Figure 11. QD set current control.

where

$$r_z = r_s + \sqrt{6} \left( \frac{L_m}{L'_r} \right)^2 r'_r \quad (48)$$

$$L_z = L_{ls} + \sqrt{6} (L'_r || L_m) \quad (49)$$

The dynamics of the z-component of the q- and d-axis currents is similar to the design of the dynamics of the x- and y-components of the q- and d-axis currents, with the exception that the z-component is coupled to the rotor circuits. However, the stator voltages and currents vary on a time scale much faster than that of the rotor flux linkages. Therefore, the rotor flux linkage terms may be treated as disturbances. A suitable control strategy is thus to synthesize the commanded z-components of the voltages as

$$v_{qs}^* = \omega_e L_z i_{ds} + (K_{pqz} + \frac{K_{ipz}}{s})(i_{qs}^* - i_{qs}) \quad (50)$$

$$v_{ds}^* = -\omega_e L_z i_{qs} + (K_{pqz} + \frac{K_{ipz}}{s})(i_{ds}^* - i_{ds}) \quad (51)$$

which is identical to the form of the control for the x- and y-components of the currents. Again assuming the actual voltage are equal to the commanded voltages the transfer function of the z-component of the stator current may be expressed

$$\frac{i_{qs}}{i_{qs}^*} = \frac{K_{pqz}s + K_{iqz}}{L_z s^2 + (r_z + K_{pqz})s + K_{iqz}} \quad (52)$$

As with the case of the x- and y- component controllers the poles may be arbitrarily placed, and the pole placement of the q- and d-axis may be placed independently, if so desired.

#### IX. ZERO SEQUENCE CONTROL

Unlike a wye-connected 3-phase machine zero sequence currents can be present in the drive system shown and should be actively controlled to zero. The control design of the zero sequence circuit is straightforward since each zero sequence circuit is dynamically equivalent to a uncoupled RL circuit. Herein, a simple first order low pass controller of the form

$$v_{ns} = -\frac{K_0}{\tau_0 s + 1} i_{ns} \quad (53)$$

is utilized, wherein 'n' may be '0', 'α', or 'β'. Although each zero sequence circuit could have a different gain, there is no reason why this would be desirable since the zero sequence circuits are all identical. The low-pass filter portion of the control helps filter out switching noise. It has been found through computer simulation that the zero-sequence circuits are much more susceptible to switching noise than the q- and d-axis. Based on (46), the characteristic equation of the zero sequence current is given by

$$s^2 + \left( \frac{L_{ls} + r_s \tau_0}{L_{ls} \tau_0} \right) s + \left( \frac{r + K_0}{L_{ls} \tau_0} \right) = 0 \quad (54)$$

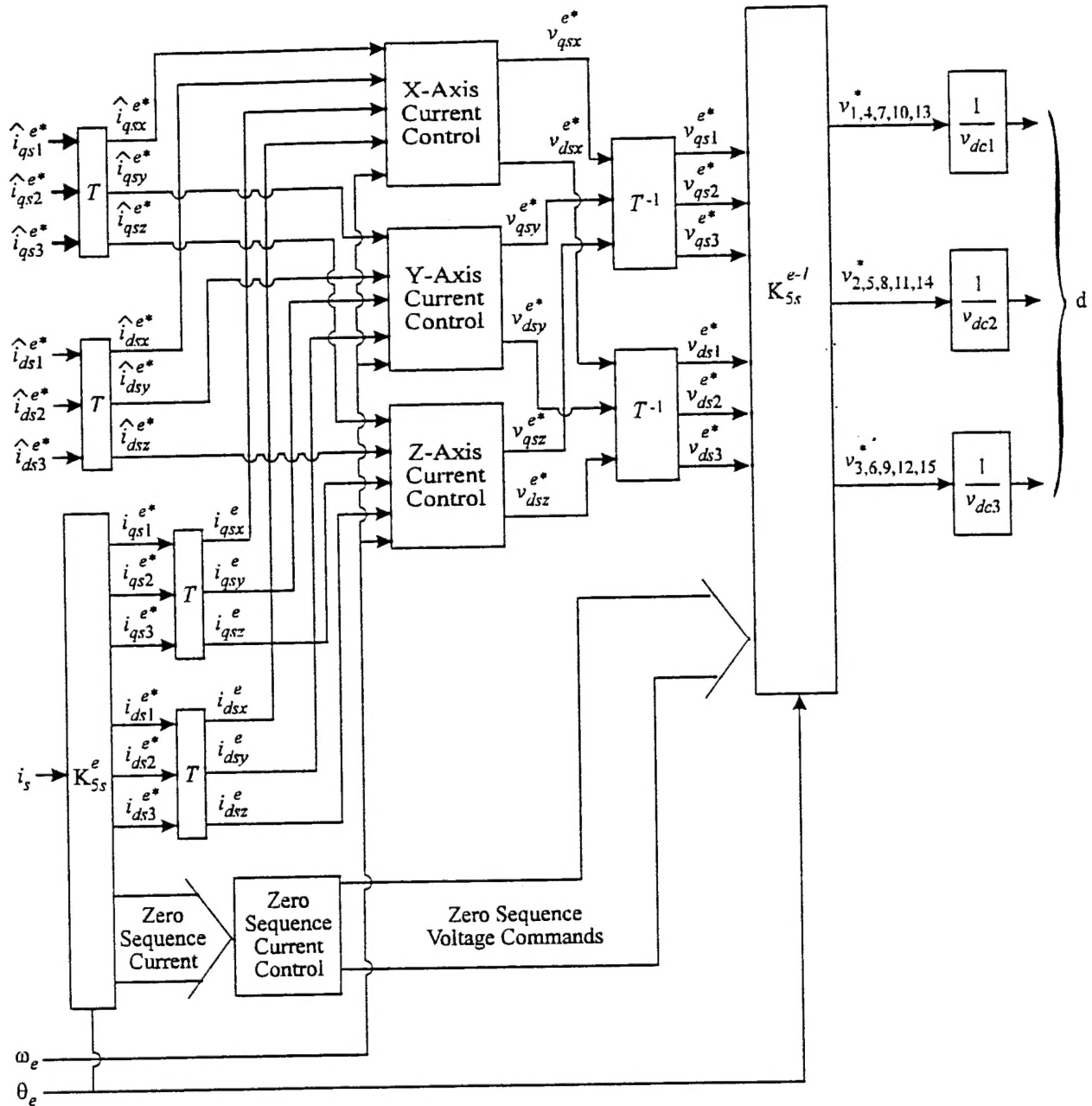


Figure 12. Current Regulator.

Using (53), by suitable selection of  $\tau_0$  and  $K_0$  the poles may be arbitrarily placed. There are no zeros associated with the zero sequence dynamics.

#### X. CURRENT REGULATOR DESIGN

The finalized current regulator is illustrated in Fig. 12. Therein the limited desired qd- currents are resolved into

x,y, and z-components. The measured currents are also transformed to qd variables. and then divided into xyz components. Based on the speed of the synchronous reference frame, the commanded xyz currents and actual xyz currents, the xyz components of a voltage commanded is determined, from which the qd voltage command is found. Finally, the qd voltage command, along with the zero sequence voltage commands are transformed to machine variables.

A sine-triangle modulator is used to achieve the desired voltage command for each phase. In particular, a duty cycle is formulated for each phase (denoted  $d_i$ ) which is compared to a unity amplitude triangle wave (denoted  $t_i$ ) as illustrated in Fig. 13. The switching signal is formulated in accordance with

$$s_i = \begin{cases} 1 & \text{if } d_i \leq t_i \\ -1 & \text{if } d_i > t_i \end{cases} \quad (55)$$

The triangle wave signals of adjacent phases are phase displaced from each other by an equal amount, and the frequency of the triangle waves is 2 kHz. It can be readily shown that, upon neglecting conduction drops, the fast average of the phase voltage is given by

$$\bar{v}_i = d_i v_{dcj} \quad (56)$$

where  $j$  denotes the dc link corresponding to the  $i$ 'th phase. Inverting this relationship provides a method of achieving the desired voltage as depicted in Fig. 13.

After selection of suitable pole locations, the current regulator gains and other control system parameter were determined and appear in Table 3.

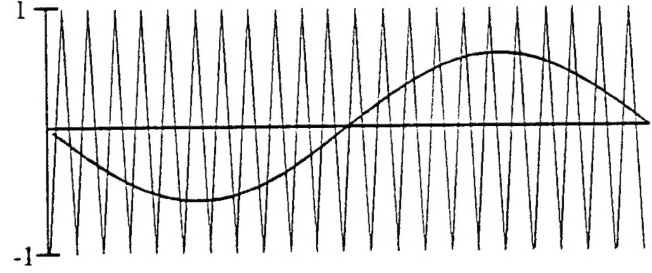


Figure 13. Sine-triangle modulation signals  $d_i$  and  $t_i$ .

Table 3. Induction Motor Controller Parameters		
$T_{e,lim} = 403 \text{ kNm}$	$T_{e,slew} = 4.03 \text{ MNm/s}$	$K = 100$
$i_{s,lim} = 650 \text{ A}$	$v_{dcb} = 5618 \text{ V}$	$\tau = 20 \text{ ms}$
$K_{pax} = 17.07 \text{ V/A}$	$K_{iax} = 306.6 \text{ V/As}$	$K_{paz} = 61.65 \text{ V/A}$
$K_{pax} = 17.07 \text{ V/A}$	$K_{iax} = 306.6 \text{ V/As}$	$K_{iaz} = 504.9 \text{ V/As}$
$K_\theta = 4.175$	$\tau_\theta = 4 \text{ ms}$	$\lambda_{dr}^* = 53 \text{ Vs}$